MODELING IONOSPHERIC SCINTILLATION AND ITS EFFECTS ON GPS CARRIER TRACKING LOOPS AND TWO OTHER APPLICATIONS OF MODELING AND ESTIMATION

A Dissertation

Presented to the Faculty of the Graduate School

of Cornell University

in Partial Fulfillment of the Requirements for the Degree of

Doctor of Philosophy

by

Todd Edwin Humphreys

January 2008

MODELING IONOSPHERIC SCINTILLATION AND ITS EFFECTS ON GPS CARRIER TRACKING LOOPS
AND TWO OTHER APPLICATIONS OF MODELING AND ESTIMATION

Todd Edwin Humphreys, Ph.D.
Cornell University 2008

Four papers are presented that introduce several applications of modeling and estimation with emphasis on the Global Positioning System (GPS). The main thrust of this work, contained in the first two papers, concerns modeling ionosphere-induced scintillation in GPS radio waves and modeling the effect of scintillation on GPS receiver carrier tracking loops. The third paper introduces a novel magnetometer-based attitude and rate estimation strategy for application to spacecraft with wire booms. The fourth paper investigates certain anomalous peaks in the power spectra of GPS-derived zenith neutral delay measurements and concludes that these peaks are caused by atmospheric pressure tides.

BIOGRAPHICAL SKETCH

Todd E. Humphreys was born the son of goodly parents in Ogden, Utah on November 18, 1974. He spent two years in northern Argentina (1994–1996) as a religious volunteer. Upon returning, he studied briefly at Weber State University and then at Utah State University, graduating with a B.S. (2000) and M.S. (2003) in electrical engineering. His Master's thesis concerned attitude determination for small satellites with modest pointing constraints. During the summers from 1999 to 2002 he worked as a researcher at NASA's Jet Propulsion Laboratory on the MEMS rate sensor development team. After graduation from Utah State University, he spent four months as a visiting estimation researcher in Madrid, where he met his beautiful wife, Fátima. They were married in 2004 during his second year of graduate studies at Cornell University. In March, 2006, they had a son, Ramón, who is widely regarded as the most wonderful little boy in the world.

Para Fátima

ACKNOWLEDGEMENTS

My thanks to my advisor, Dr. Mark Psiaki, who is attentive, supportive, and—above all—utterly competent. Thanks to my co-advisor Paul Kintner for tutoring me like a son. Thanks to my parents and siblings for their prayers and encouragement. And my sincerest thanks to my wife Fátima and son Ramón: being by your side has made sweet memories of these years in Ithaca.

TABLE OF CONTENTS

LIST OF FIGURES

LIST OF TABLES

Chapter 1

Introduction

Increased dependence on the Global Positioning System (GPS) and other satellite navigation systems makes users vulnerable to signal loss or degradation caused by ionospheric effects. Radio wave scintillation, the temporal fluctuation in phase and intensity caused by electron density irregularities along the propagation path, stresses a GPS receiver's carrier tracking loop, and, as severity increases, can lead to navigation bit errors, cycle slipping, and complete loss of carrier lock [1–8].

In anticipation of the 2011 solar maximum, when scintillation effects will be more severe, there is great interest in (1) understanding how scintillation affects GPS receiver tracking loops, (2) developing ways to efficiently and comprehensively test GPS receivers under realistic scintillation conditions, and (3) developing tracking loop architectures that perform robustly in the presence of scintillation. Chapters 2 and 3 address points (1) and (2).

In Chapter 2, a large library of specially-processed scintillation data is compiled and used to characterize the features of scintillation that make carrier tracking difficult. The response of GPS receiver phase tracking loops to scintillation is studied by injecting the recorded scintillation data into a testbed in which software tracking loops simulate the behavior of the phase tracking loops in typical GPS receivers. On the basis of the simulation results, a model is developed that approximately predicts the rate of cycle slipping that a typical phase tracking loop experiences when tracking a given interval of recorded scintillation. The model distills the properties of scintillation down to two parameters that are relevant for tracking loops: the scintillation index S_4 and the decorrelation time τ_0.

In Chapter 3, the scintillation effects model developed in Chapter 2 is used in another role. Now, instead of predicting loop tracking performance, the model is used to synthesize realistic scintillation time histories. When used in the scintillation testbed, such time histories enable controlled and comprehensive evaluation of software GPS tracking loops. The time histories can also be used as input to a GPS signal simulator to test hardware GPS receivers for scintillation robustness. Hence, the simulator proposed in Chapter 3 offers a solution to problem (2) above.

Chapters 2 and 3 of this dissertation can be viewed as setting up the necessary framework for addressing problem (3) above; that is, the problem of developing scintillation-robust GPS tracking loops. Now with a better understanding of scintillation effects, tracking loops can be specifically configured to reduce phase error variance and avoid cycle slipping to the extent possible. These modified loops can then be tested over a wide range of scintillation parameters using the scintillation simulator. The hope is that by exploiting the scintillation model and simulator offered in the following chapters there will be fewer surprises due to scintillation when operating GPS receivers during the 2011 solar maximum than there were during the 2000 solar maximum [4].

In addition to the two papers treating GPS receivers and scintillation, two other papers are included as chapters in this dissertation. Chapter 4 develops an attitude and rate estimation strategy for a sounding rocket payload with wire booms. Chapter 5 shows that the pico-seconds GPS signal propagation delay introduced by daily atmospheric tides can be detected by a network of GPS receivers when measurements are averaged over several years. The conclusions follow in Chapter 6.

Chapter 2

Characterization of Severe Ionospheric Scintillation and its Effect on GPS Carrier Phase Tracking

T. E. Humphreys, M. L. Psiaki, B. M. Ledvina, A. P. Cerruti, and P. M. Kintner, Jr., "Characterization of severe ionospheric scintillation and its effect on GPS carrier phase tracking," *IEEE Transactions on Aerospace and Electronic Systems*, 2007, submitted for review.

2.1 Abstract

A large set of equatorial ionospheric scintillation data has been compiled, used to characterize features of severe scintillation that impact Global Positioning System phase tracking, and used to develop a scintillation testbed that evaluates tracking loops. The purpose of this work is to develop a simple, general, and realistic scintillation effects model that can be used to improve the scintillation performance of phase tracking loops. It is known that severe equatorial scintillation causes cycle slipping and, in the worst cases, complete loss of carrier lock. Data-driven tests that evaluate the scintillation robustness of typical phase tracking loop architectures indicate that cycle slips are predominantly connected with the abrupt, near half-cycle phase changes that occur during the deep power fades of severe equatorial scintillation. A new characterization of scintillation effects proposed herein employs a differentially-detected bit error model to predict cycle slipping rates that approximately agree with the data-driven simulation tests.

2.2 Introduction

A transionospheric radio wave can exhibit temporal fluctuations in phase and intensity caused by electron density irregularities along its propagation path. This phenomenon, called scintillation or fading, is a subject of both scientific interest and practical concern [9]. At Global Positioning System (GPS) frequencies (L band), strong scintillation is manifest in deep power fades (> 15 dB) that are often associated with rapid phase changes. Such vigorous signal dynamics stress a receiver's carrier tracking loop and, as their severity increases, lead to navigation bit errors, cycle slipping, and complete loss of carrier lock [2–8].

Increasingly, modern GPS applications are exploiting techniques that require carrier phase measurements. In view of this trend, and of their already widespread use, attention is focused here on phase tracking loops, or phaselock loops (PLLs), as opposed to frequency tracking loops.

Severe L-band scintillation is both infrequent and geographically confined. The type known as equatorial scintillation, or equatorial spread F, generally occurs between 1900 and 2400 local time in the region extending $\pm 15^\circ$ about the geomagnetic equator [10]. Another common type of scintillation occurs at high latitudes [11]. Significant effects have also been noted in the mid-latitude region, but they occur infrequently [12]. This paper concentrates on equatorial scintillation because it is particularly difficult to track.

Despite their relative rarity, scintillation effects are a serious concern for certain GPS user communities whose applications place demanding requirements on receiver performance. Consider three examples:

1. Proposals for GPS-based ionospheric research call for large arrays of GPS re-

ceivers whose combined phase and amplitude measurements will be used to image fine-scale ionospheric structures during scintillation events. Such studies would be compromised by receivers that repeatedly lose phase lock.

2. Carrier-phase-based GPS techniques that are capable of subdecimeter-level relative positioning accuracy are finding increased use in civilian and military applications [13],[14, Ch. 7]. These techniques rely on accurate resolution of carrier phase ambiguities, a process that may take several minutes. Severe scintillation poses a threat to such carrier-based techniques because, among other things, repeated cycle slipping on the same GPS link, or slipping on more than one link, causes new ambiguities in the carrier phases that must be resolved before the system can recover operational accuracy.

3. The aviation community is anticipating an overhaul of the air traffic control system that would see GPS replace radar as the primary aircraft location sensor [15]. There is concern that severe scintillation effects may prevent the system from meeting its exacting integrity requirements.

As these examples show, there is interest in developing GPS receivers whose tracking loops are specially designed to maintain lock in the presence of severe scintillation. Design and testing of such receivers depends crucially on accurate models of scintillation and its effects on receivers. Several researchers have responded to this need by developing models for scintillation effects on PLLs [3, 5–8, 16], but as will be shown, these models are not sufficiently realistic. Instead, they tend to underestimate the effects of severe equatorial scintillation by failing to capture its essential feature: large, abrupt phase changes associated with deep power fades.

To put this paper's contributions in context, the following list outlines current approaches to characterizing scintillation effects on GPS receivers. The strengths and

limitations of each approach are noted.

Statistical models [5, 6]: In this approach, scintillation intensity, as measured by the S_4 index and the phase spectrum profile, is used to estimate the PLL's phase error variance, σ_φ^2. A hypothetical receiver is said to lose lock when σ_φ^2 exceeds a certain threshold. This approach's generality and simplicity are appealing, but, as currently implemented, it tends to underestimate the rate of cycle slipping in actual scintillation. First, it assumes the PLL is operating in its linear regime, which, in the case of strong scintillation, is likely not the case. Second, as implemented in [5, 6], the value of the lock threshold is chosen based on the erroneous assumption that phase noise is uncorrelated in time.

Simulation using synthetic phase and amplitude time histories [7, 16]: In this approach, synthetic scintillating phase and amplitude time histories are generated in such a way that their power spectra and probability distributions match well-accepted models [17–19]. The phase and amplitude time histories are then fed as inputs to a simulated PLL whose phase error variance σ_φ^2 and rate of cycle slipping are observed. One advantage of this approach is that it requires no assumption that the loop operates in its linear regime. Hence, the cycle slipping and phase error are a true reflection of the simulated loop's response to the synthetic inputs. As will be shown in Section 2.4.3, however, correct power spectra and distributions can produce synthetic phase and amplitude time histories that are unrealistically easy to track.

Simulation using recorded wideband scintillation data [3, 20]: In this approach, a non-real-time software GPS receiver processes raw wide-bandwidth digital data that were previously recorded on a digital storage device during a scintillation event. The behavior of the software receiver's PLL is observed as it tracks through the fluctuations in the recorded data. Since no simplifying models or assumptions are introduced, this approach is a very realistic test of receiver performance. It is flexible in the sense that

a designer may evaluate different tracking loop strategies and may add noise to the recorded data bitstream to simulate a reduced signal-to noise-ratio. However, there are several drawbacks: (1) A designer is only at liberty to adjust the scintillation intensity insofar as varying levels of intensity are present in the recorded data; (2) the method is computationally expensive—correlations must be computed from the raw data on each run; (3) without any model to describe the effect of the scintillating input signal on the carrier tracking loop, the method does not provide the kind of insight that can guide receiver design; and (4) the "true" phase time history is unknown, so phase error and cycle slips are not defined, though complete loss of carrier lock is obvious.

Hardware-in-the-loop simulation [8, 21]: In this method, empirical [21] or synthetic [8] phase time histories are used to drive phase variations in the RF output of a GPS signal simulator. Likewise, amplitude fades are simulated by modulating the simulator's output signal strength manually [21] or according to a synthetic amplitude time history [8]. A GPS receiver to be tested is connected to the simulator and the behavior of the receiver's tracking loops is observed. To the extent that the input phase and amplitude time histories are realistic and loss of lock is reliably detected, this method is an effective end-to-end test of a full receiver. However, it inherits drawback (3) from the previous paragraph and, as currently implemented in [21], the "true" phase data is 1st-order low pass filtered at 2 Hz. As will be discussed in Section 2.4.3, this practice artificially softens the effect of severe phase scintillation on the receiver's PLL. The same section will note that the synthetic phase time history in [8] is likely unrealistic for severe equatorial scintillation.

Field testing [4]: Field testing is of course the ultimate confrontation with reality both for receivers and for the scintillation models used to validate them. Thus, the results of a campaign on Ascension Island during the last solar maximum exposed worrisome

vulnerabilities in the receivers tested and raised questions about the overly optimistic simulations conducted prior to the campaign [4]. Nonetheless, as with the previous two methods, field testing is not a substitute for models that describe how scintillation affects the carrier tracking loop. Such models yield the insight necessary to guide receiver design and they enable bench tests, which can be more exhaustive than field tests.

This paper presents a data-driven simulation testbed for evaluating carrier phase tracking loops that is meant to overcome the foregoing methods' limitations. This tool will be referred to as the scintillation testbed or simply the testbed throughout the remainder of this paper. The testbed is realistic and flexible, and it reveals an intuitive connection between cycle slips and the scintillation patterns that cause them. It is based on a library of empirical phase and amplitude time histories recorded under a wide range of equatorial scintillation conditions, and represents an extension of the work in [3] and [20].

As a preamble to the presentation of the scintillation testbed, Section 2.3 introduces the empirical scintillation library and Section 2.4 presents observations about general characteristics of severe scintillation. Particular attention will be focused on an especially troublesome fading phenomenon herein termed "canonical fading." Section 2.5 then addresses some general effects of scintillation on phase tracking. The testbed is presented in Section 2.6. Section 2.7 describes the example PLLs that will be evaluated in the testbed and Section 2.8 presents their performance results. The results will demonstrate a close connection between cycle slips and errors in differentially-detected navigation data bits. This connection will suggest a model, developed in Section 2.9, of scintillation effects on GPS receiver phase tracking loops. The conclusions follow in Section 2.10.

2.3 The Empirical Scintillation Library

A library of empirical equatorial phase and amplitude scintillation phenomena has been compiled for use in the scintillation testbed. This section describes the data on which the library is based and briefly summarizes the processing required to generate the library's individual records.

To cover a broad range of severe scintillation effects, the empirical scintillation library includes equatorial scintillation data from two different sources. The first source is a set of data from the DNA Wideband satellite experiment, a radio beacon experiment that was operational from 1976 to 1979 [18, 22]. From a near-polar 1000-km orbit, the Wideband satellite broadcast 10 coherent continuous-wave signals whose frequencies ranged from VHF to S-band and included an L-band signal at 1239 MHz that is nearly coincident with the GPS L_2 signal. The 2891-MHz S-band signal, which, because of its high frequency was minimally affected by scintillation, was used as the phase reference for the lower frequencies in a coherent, multi-band receiver chain. The receiver chain's baseband phase and amplitude outputs were bandlimited to 150 Hz and digitized at 500 Hz. It should be emphasized that these baseband data, not the original high frequency carrier signals, are the Wideband data referred to in this paper.

The Wideband data included in the scintillation library were recorded at two equatorial ground stations, one in Ancon, Peru (11.8° N latitude) and the other on Kwajalein atoll in the Marshall Islands (9.4° N latitude). Each ground station was equipped with a 9.1-m parabolic tracking antenna. The high-gain antennas, together with 12-bit quantization and the 500-Hz sampling rate, yielded high-quality, low-noise complex signal time histories. Moreover, the fact that the received signals were continuous-wave ensured that cycle slips, when they occurred, were whole-cycle slips or multiples thereof;

i.e., there are none of the half cycle slips that occur when tracking the bi-phase modulated GPS signals. Whole cycle slips are present during very strong patches of scintillation, as evidenced by a comparison among signals at different frequencies, but these do not diminish the usefulness of the data in an empirical model. This issue will be further discussed in a later section.

Among the 10 signals broadcast by the Wideband satellite, the 1239-MHz L-band signal, which is nearest the 1227.6-MHz GPS L_2 frequency, is of greatest interest for studying scintillation effects on GPS receivers. However, because the Wideband data were recorded roughly two years before solar maximum, the L-band data are not representative of the strongest equatorial scintillation at GPS frequencies. To represent extreme scintillation events, the L-band data are augmented in the scintillation library with unscaled data from the uppermost UHF carrier at 447 MHz. As will be detailed in the following section, it is conjectured that the UHF data provide test cases that exceed the worst L-band scintillation likely to occur at solar maximum.

Ten passes marked by strong scintillation were chosen from the archives of the Wideband experiment for inclusion in the scintillation library. Each recorded satellite pass yields approximately 12 minutes of continuous data, which are stored in the library as complex time histories at the original 500-Hz sampling rate. No high-pass filtering to remove trends nor low-pass filtering to remove receiver noise were required.

The second source of data for the scintillation library is a set of GPS L_1 C/A code digital data sampled at 5.7 MHz. The data were recorded in December 2003 at Cachoeira Paulista, Brazil (22.7° S latitude) [20], which lies along the southern boundary of the Appelton equatorial anomaly—a region notorious for strong scintillation [10]. The recorded data set spans several hours and includes strongly scintillating signals on multiple GPS links. The data have been extensively processed to generate empirical

scintillation library records that are comparable in quality to those from the Wideband data. The goal of this processing has been to eliminate, insofar as possible, all receiver and Doppler effects on the phase and amplitude data, leaving only effects due to scintillation.

The raw 5.7-MHz samples are initially processed through a software GPS receiver to extract carrier phase, amplitude, and navigation bit estimates for each GPS signal present. If bit parity failures are detected—as is often the case during patches of strong scintillation—then a record of correct navigation bits is compiled and used to eliminate, or "wipe off," the data bits from the incoming GPS signal in a reprocessing run, this time using a standard nonsquaring PLL in place of the squaring (Costas) loop. This strategy ensures that, like the Wideband data, the GPS phase time histories are free from half-cycle slips, though they may be affected by whole cycle slips. The carrier phase output is further processed to eliminate, to the extent possible, variations due to receiver clock instability, PLL dynamics, and Doppler. Both the output phase and amplitude data, which are sampled at 100 Hz, are then filtered to reduce receiver noise. However, owing to the weakness of the GPS signal and the low gain of the receiving antenna, the GPS data's signal-to-noise ratio (SNR) remains considerably lower than the Wideband SNR. Details of the GPS data preliminary processing techniques are found in the Appendix. Table 2.1 summarizes the contents of the empirical scintillation library.

Table 2.1: Summary of empirical scintillation library contents

Data source	Original Carrier Frequency (MHz)	Combined length of records (hours)
Wideband	447 (UHF)	1.9
Wideband	1239 (~ GPS L_2)	1.9
GPS	1575 (GPS L_1)	3.7

2.4 Characteristics of Severe Scintillation

Short samples from two different scintillation library records are presented in Fig. 3.1 (Wideband L-band data) and in Fig. 3.2 (GPS L_1 data). Both records manifest strong scintillation, each with $S_4 \approx 0.9$, where S_4 is the standard scintillation index defined by

$$S_4^2 = \frac{\langle I^2 \rangle - \langle I \rangle^2}{\langle I \rangle^2} \tag{2.1}$$

in which I is signal intensity (squared amplitude) and $\langle \cdot \rangle$ denotes time average. As mentioned previously, the GPS data's SNR is worse than that of the Wideband data (evidenced by the small, high-frequency ripples on the plots in Fig. 3.2), but this does not obscure the obvious similarities between the two samples. The most striking features are the deep power fades that occur simultaneously with abrupt, approximately half-cycle phase changes whose sense (downgoing or upgoing) appears random. Such fades are found in patches of severe scintillation throughout the scintillation library. They appear to be a universal feature of strong equatorial scintillation. As will be demonstrated later on, they are the primary cause of phase unlock for PLLs tracking a strongly scintillating signal that carries bi-phase modulated data, as is the case for GPS signals. They will be designated "canonical fades" for convenience in this paper.

2.4.1 Scintillation Severity

It will be useful to discuss the contents of the scintillation library in terms of the scintillation index S_4 and of a general measure of scintillation rapidity, the decorrelation time τ_0, which is defined as the time lag at which a scintillating baseband signal's autocorrelation function falls off by a factor $1/e$ (a more detailed definition of τ_0 will be given in Section 2.9.2). The scintillation library includes a reasonably comprehensive

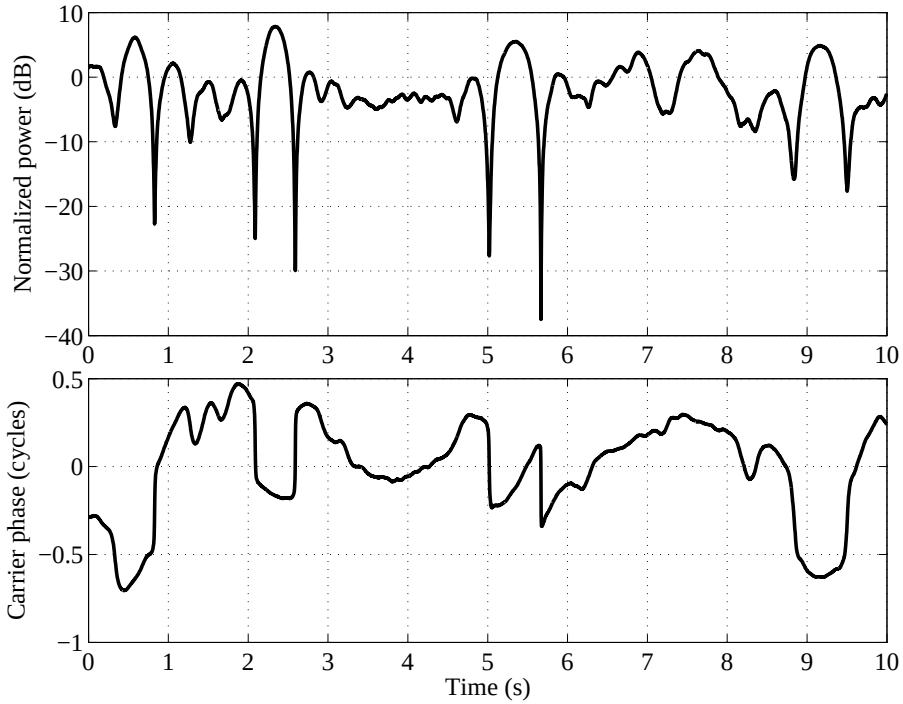

Figure 2.1: An excerpt of normalized signal power (upper panel) and carrier phase (lower panel) from a record of Wideband L-band data with $S_4 \approx 0.9$.

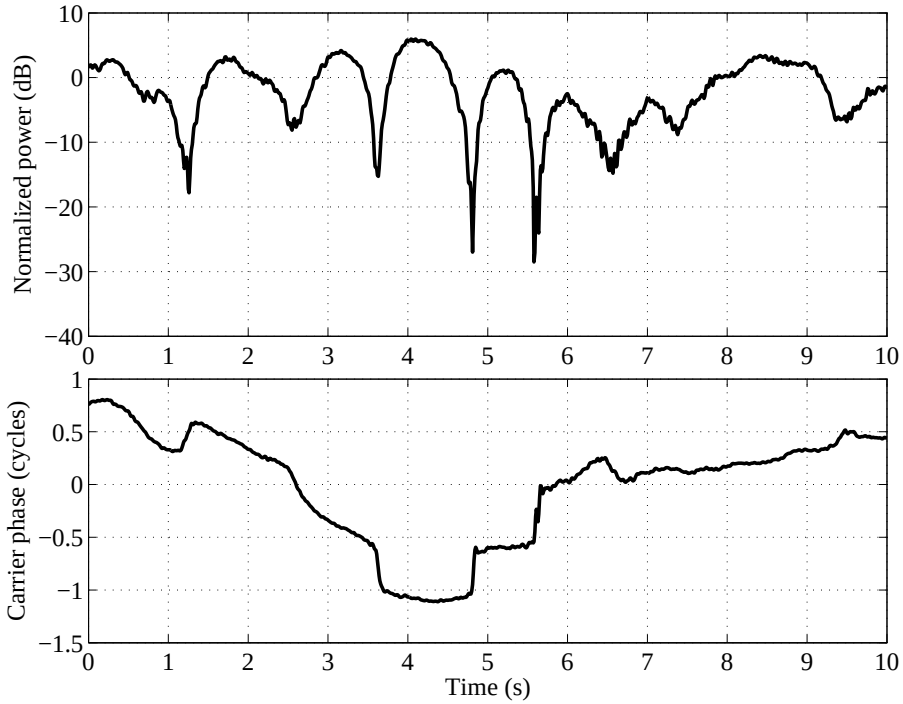

Figure 2.2: As Fig. 3.1 for GPS L_1 data. Again, $S_4 \approx 0.9$.

sampling of equatorial scintillation phenomena, with S_4 indices ranging from near zero to approximately 1.2 and values of τ_0 spanning an order of magnitude. It will be shown later on that, for purposes of phase tracking, scintillation severity can be conveniently parameterized by S_4 and τ_0.

During intervals of weak to moderate scintillation ($S_4 \lesssim 0.5$), the Wideband 447-MHz data manifest S_4 indices that are approximately 3.7 times greater than those for the corresponding interval at 1239-MHz. This is roughly consistent with the $S_4 \propto f^{-1.5}$ scaling predicted by weak scintillation theory [9]. As scintillation severity increases, multiple scattering effects cause the S_4 indices at all scintillation library frequencies (447, 1239, and 1575 MHz) to saturate near 1. Thus, when considered only in terms of the S_4 index, patches of strong UHF scintillation do not appear more severe than patches of strong Wideband L-band or GPS L_1 scintillation.

In contrast, the rapidity of strong scintillation at UHF can exceed that at L-band for equivalent line-of-sight dynamics. This is because the multiple-scattering effects associated with severe scintillation lead to spectral broadening (decreased τ_0), and these effects are stronger at lower frequencies [9]. Thus, values of τ_0 for the scintillation library's Wideband UHF and L-band data recorded simultaneously during patches of severe scintillation reach lows of 0.12 and 0.4 seconds, respectively, which confirms the increased severity of the UHF scintillation.

Because of the different ionospheric conditions along the various GPS links represented in the GPS L_1 data, the data include a wide range of τ_0 values, from ~ 2 seconds during weak to moderate scintillation to 0.5 seconds during severe scintillation. That the minimum values of τ_0 for the Wideband L-band and GPS data are not more disparate is surprising given the large difference in the radio line of sight scan velocity in the ionosphere's F layer. (Recall that the F layer is the dense ionospheric layer at approximately

350 km altitude where the irregularities that cause scintillation tend to form.) Over the intervals shown in Figs. 3.1 and 3.2, the Wideband and GPS τ_0 values were 0.4 and 0.8 seconds, respectively. By comparison, the respective scanning velocities were about 4000 m/s and 100 m/s, and typical background ionospheric drift velocities range from 100 to 200 m/s [23]. Hence, excluding other factors, one would expect the Wideband and GPS τ_0 values for these segments to differ by at least a factor of 10 instead of 2. This paradox can be resolved by considering the geometry of ionospheric structures and their drift rates relative to the scan velocity vector. As noted in [23], time scales of equatorial scintillation are determined by the horizontal velocity of the scan point measured with respect to the drifting ionosphere and in a direction perpendicular to the local magnetic field. For the GPS data, this relative velocity is determined by a combination of ionospheric drift and the east-west scanning of the line-of-sight vector. For the Wideband data, the near-polar orbit of the transmitting satellite implies that most of the scan velocity is in the north-south direction—nearly aligned with the local magnetic field. This is believed to be the reason why the large scanning velocity does not lead to greatly reduced values of τ_0.

It will be shown in later sections that complex signal scintillation is, on average, more difficult to track as S_4 increases and as τ_0 decreases. Therefore, for the present study, the upshot of the foregoing S_4 and τ_0 considerations is that the Wideband L-band data can be considered a reasonable proxy for severely scintillating signals at the GPS L_2 frequency, whereas the Wideband UHF data is only useful in the sense that it is more vigorous than all conceivable extreme cases of L-band scintillation, and can thus be used to test the limits of GPS tracking loop capability. Slow scintillation (large τ_0) at high S_4 can also challenge tracking loops when deep power fades persist for several seconds. Such cases are represented in the library's GPS L_1 data by several instances of power fades exceeding 15 dB and lasting $\sim$ 2 seconds.

Note that the above time scales apply only to the static receivers that were used to collect the data contained in the scintillation library. Receivers mounted on dynamic platforms may see significantly faster or slower scintillation. For example, when a dynamic platform causes the line-of-sight vector to move "in resonance" with irregularity patterns, deep power fades may last significantly longer than 2 seconds [23]. By redefining the scintillation library's sampling interval, the library can easily accommodate more extreme scintillation time scales, but this has not been done for the present study.

2.4.2 First-order Statistics and Phase Power Spectra

Besides S_4 and τ_0, other signal statistics useful for scintillation modeling are shown in Figs. 2.3 and 2.4. Empirical first-order amplitude and phase rate distributions are plotted in Fig. 2.3. In panel (a) the full 300-sec GPS record from which the excerpt in Fig. 3.2 is taken has been used to generate an empirical joint distribution, expressed in density of samples, in the variables $\Delta\theta$, the phase change over 20 ms (the duration of a GPS navigation data bit), and α, the normalized fading amplitude. Strongly scintillating Wideband data are similarly distributed. The distribution reveals the effect of canonical fading as an increased spreading of $\Delta\theta$ for small values of α. Some spreading in $\Delta\theta$ is also due to an increase in phase errors at low loop SNR, but this is a lesser effect. The marginal distribution of α [panel (c)] agrees well with the Rice distribution [24, Ch. 2], and even better with the popular Nakagami-m distribution, given by [17]

$$p(\alpha) = \frac{2m^m \alpha^{2m-1}}{\Omega^m \Gamma(m)} \, e^{-m\alpha^2/\Omega} \tag{2.2}$$

where the parameter $m = 1/S_4^2$ and $\Omega \equiv E[\alpha^2]$ is the mean-square of the fading amplitude. Here, amplitude normalization implies $\Omega = 1$. In practice, the ensemble expectation $E[\cdot]$ is computed as the time average $\langle\cdot\rangle$ over intervals of approximate stationarity.

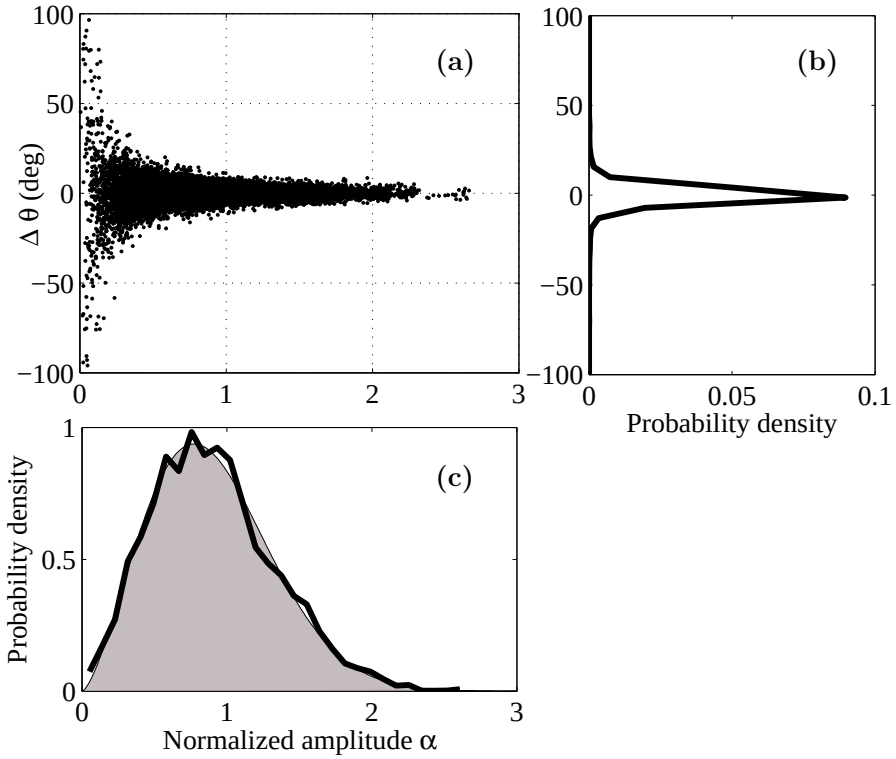

Figure 2.3: (a) Empirical joint probability distribution in the variables $\Delta\theta$ and α. (b) Marginal empirical distribution in $\Delta\theta$. (c) Marginal empirical distribution in α (solid line) compared with the Nakagami-m distribution (shaded area) corresponding to the empirical S_4 value.

The marginal distribution of $\Delta\theta$ [panel (b)] appears benign, but a close examination reveals long tails relative to the Gaussian distribution. It will be shown that these tails are responsible for most scintillation-induced cycle slipping.

Another characterization commonly used for scintillation effects modeling is the phase power spectrum, shown for several example data sets in Fig. 2.4. For the GPS L_1 data, filtering has been omitted so that the frequency content of the raw scintillating signal is properly exhibited. The figure's three spectra are derived from strongly scintillating data ($S_4 > 0.9$). Over frequencies of interest for phase tracking, the spectra

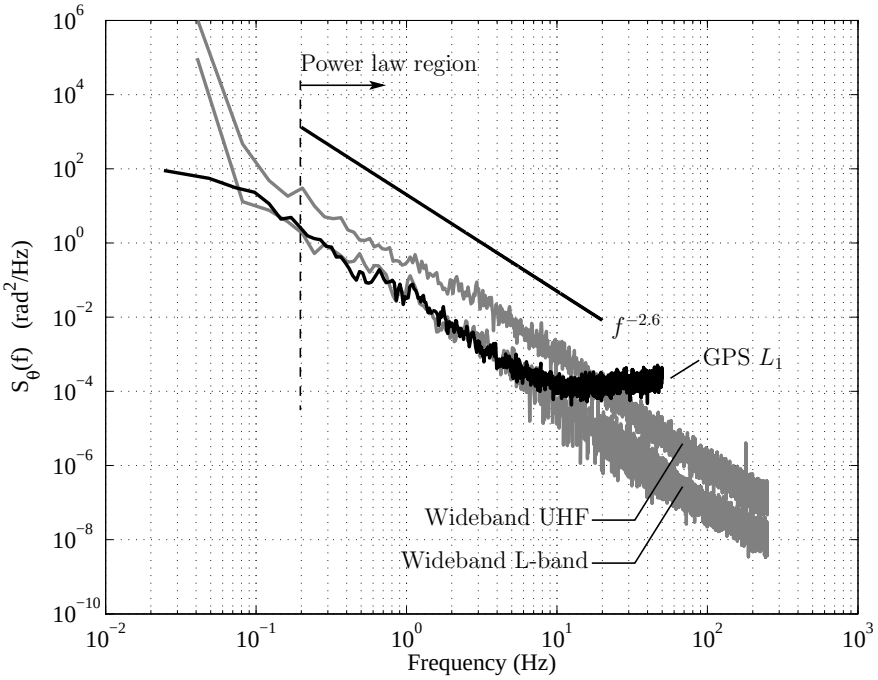

Figure 2.4: Phase power spectra of various data samples. For frequencies to the right of the dashed line, the spectra are well approximated by the power law $S_\theta(f) = Tf^{-p}$. For reference, the solid line shows the spectral slope corresponding to $p = 2.6$.

conform to the profile predicted by weak-scatter phase screen theory [19]:

$$S_\theta(f) = \frac{T}{(f_0^2 + f^2)^{p/2}} \tag{2.3}$$

where T is a strength parameter, f_0 is the temporal frequency corresponding to the ionospheric outer scale, and p is the phase power law index. In practice, the value of f_0 is not well-defined. In any case, it is much smaller than frequencies relevant to PLL phase errors, which are on the order of the PLL noise bandwidth ($\sim$ 10 Hz). Accordingly, it is assumed that $f_0 \ll f$ over frequencies of interest, and Eq. (2.3) is approximated by the power law $S_\theta(f) = Tf^{-p}$, where T is reinterpreted as the power density at 1 Hz.

The pronounced bend in the GPS L_1 spectrum near 10 Hz marks the noise floor of the GPS data. No such floor is present in the Wideband data out to the 250-Hz Nyquist cutoff frequency. Accordingly, when used in the scintillation testbed, the Wideband

library records are modeled as having no noise component (infinite SNR) whereas each GPS record is modeled as having a known, irreducible noise component.

Until diverging at the GPS noise floor, the GPS and Wideband data have similar p values, in this case $p \approx 2.6$. A survey of all library records shows 2.6 to be the empirical limit of p at high S_4. Such convergence is a consequence of the canonical-fade-induced abrupt phase changes, which, as they become more frequent and discontinuous, drive p toward 2, the high frequency asymptote for any discontinuous signal.

The important point of Fig. 2.4 as regards phase tracking is the following: phase scintillation is not confined below any particular frequency. Hence, some phase power density will unavoidably fall outside a practical PLL's tracking bandwidth, resulting in phase tracking errors. Such errors lead to cycle slips when the phase changes are sufficiently large and abrupt, as is often the case with canonical fading.

2.4.3 Canonical Fading

It is instructive to make a closer examination of the canonical fading phenomenon. Even before conducting experiments, one would expect canonical fading to have a strong adverse effect on PLL performance. Consider an analogy for the effect of canonical fading on a PLL's ability to track carrier phase: Suppose that, while driving at night, a driver's headlights dimmed each time the car came upon a curve in the road. Suppose, further, that the curve could be hard to the left or hard to the right with equal probability. Under these conditions, the driver would find it difficult to maintain the car on the road. In the analogy, the dimming headlights represent the fading-induced low loop SNR, which makes phase much harder to measure. Occasional cycle slips during canonical fades are inevitable as the PLL "misses the curve." This hypothesis is borne out by

testbed experiments.

At first glance, it appears that the rapid phase changes associated with the canonical fades in Figs. 3.1 and 3.2 might be phase errors that arise at low loop SNR rather than genuine shifts in the incoming carrier phase. However, the two effects can be distinguished by noting that, once the nominal SNR level is recovered after a fade, the net phase change should be small under the hypothesis that the true carrier phase is changing smoothly. Instead, a net phase change approaching $1/2$ cycle is observed. Furthermore, given that both the GPS receiver (with data bit wipeoff) and the Wideband receiver are incapable of fractional cycle slips, the approximately half-cycle phase shifts cannot be attributed to receiver cycle slipping.

The canonical fading phenomenon becomes intuitive when a receiver's scintillating complex baseband signal $z(t)$ is represented on the complex plane (Fig. 2.5). The signal's instantaneous phase and amplitude can be associated with a phasor that wanders about the plane with a speed inversely proportional to τ_0. As strong fading drives the phasor's magnitude toward zero, it's motion through a small neighborhood centered at the origin tends to produce swift, half-cycle phase changes, the hallmark of canonical fades.

Canonical fades have been noted in earlier studies of scintillation [16, 19] (though not by name), and have been reproduced in phase screen scintillation models [25, 26], but they have not been accounted for in models of scintillation effects on GPS tracking loops [5–8, 16]. These latter models successfully reproduce the first-order scintillation statistics described in [18] and the phase and amplitude spectra derived from phase screen theory in [9] and [19]; nevertheless, their phase and amplitude time histories are unconvincing because they fail to reproduce the canonical fading phenomenon at high S_4.

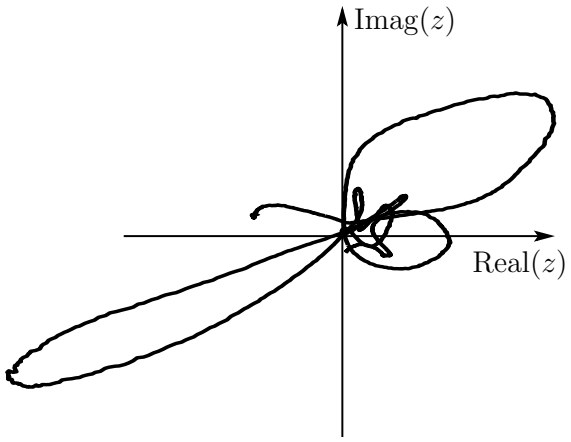

Figure 2.5: A trace on the complex plane of the complex baseband signal $z(t)$ corresponding to the first three seconds of the amplitude and phase time histories in Fig. 3.1.

To understand why, recall from Fig. 2.3 that canonical fading shows up as a correlation between signal amplitude and the absolute value of phase rate—a correlation that is not detected by first-order phase and amplitude statistics. Moreover, although the phase time histories shown in Figs. 3.1 and 3.2 lead to power-law phase spectra (Fig. 2.4), the inverse is not generally true; that is, a power-law phase spectrum does not guarantee a realistic phase time history. The method used to generate a synthetic phase time history in [7] (and likely in [8], though details are not provided) consists of passing white Gaussian noise through a low-pass shaping filter. While this method can indeed produce a phase time history with an arbitrarily shaped spectrum, it does not tend to generate the large, nearly discontinuous phase jumps associated with canonical fades. Moreover, because the methods in [7] and [8] shape the phase and amplitude spectra independently, whatever abrupt phase changes are present in the synthesized phase time history are not, in general, coincident with deep amplitude fades. As a result, the synthetic phase time history is unrealistically easy to track.

Failing to account for canonical fading can also impair scintillation models based on

empirical data. For example, in [21] a scintillation monitor's 50-Hz phase measurements are used to drive phase variations in a hardware-in-the-loop simulation. In a preprocessing step, the phase data are first-order low-pass filtered with a cutoff frequency of 2-Hz. This is done under the assumption that the filtering reduces the high-frequency noise in the measured phase data without significantly distorting the phase variations due to scintillation. The problem with this approach is that it artificially rate-limits the genuine phase changes associated with canonical fades, thereby making the phase history easier to track. To avoid such rate limiting, the empirical scintillation models advanced in the present paper are either not low-pass filtered (Wideband data) or are low-pass filtered with a generous 20-Hz cutoff frequency (GPS data).

2.5 Overview of Scintillation Effects on Phase Tracking Loops

Phase tracking loops are affected by scintillation in three related ways: (1) increased phase error variance, (2) cycle slipping, and (3) frequency unlock. This section gives an overview of these effects to set terms and develop intuition before the scintillation testbed is introduced. For a general treatment of phase tracking loops, the reader is referred to [27–30].

2.5.1 Phase Error Variance

Consider a standard (non-squaring) PLL with true phase input $\theta(t)$ and phase estimate $\hat{\theta}(t)$. When the phase error $\varphi(t) = \theta(t) - \hat{\theta}(t)$ is small enough that the PLL's phase detector can be regarded as linear, then, for zero-mean white driving noise, the PLL's phase error

variance $\sigma_\varphi^2 = E[\varphi^2(t)]$ (in rad^2) is accurately approximated by [29]

$$\sigma_\varphi^2 = \frac{B_n N_0}{C} \equiv \frac{1}{\rho_L} \tag{2.4}$$

where C/N_0 is the carrier power to noise ratio, B_n is the PLL's single-sided noise bandwidth, and ρ_L is the loop SNR. Under normal circumstances, GPS carrier phase tracking requires a squaring (e.g., Costas) PLL, which is insensitive to the half-cycle phase changes induced by the data bit modulation. In a squaring PLL, the actual phase error tracked is 2φ, with the corresponding variance denoted by $\sigma_{2\varphi}^2$. Furthermore, ρ_L is reduced by a squaring loss factor approximately equal to [3]

$$\mathcal{S}_L = \left(1 + \frac{N_0}{2T_a C}\right)^{-1} \tag{2.5}$$

where $1/T_a$ is the pre-detection bandwidth. [Equation (2.5) is exact for a Costas loop with a multiplicative phase detector.] Thus, for the squaring loop,

$$\sigma_\varphi^2 = \frac{\sigma_{2\varphi}^2}{4} = \frac{1}{\rho_L \mathcal{S}_L} \tag{2.6}$$

is a useful approximation for σ_φ^2 in the linear regime. For analysis of the squaring loop, an equivalent loop SNR is defined as [24, p. 206]

$$\rho_{eq} \equiv \frac{\rho_L \mathcal{S}_L}{4} \tag{2.7}$$

which leads to $\rho_{eq} = 1/\sigma_{2\varphi}^2$ for small 2φ.

At large values of φ, the assumption of PLL linearity breaks down and analysis becomes much more difficult. An exact expression for σ_φ^2 for a 1st-order non-squaring PLL driven by white Gaussian noise is found in [27, Ch. 4]. Precise phase error statistics for all but this standard 1st-order loop are typically obtained via simulation. Fortunately, one can show that the exact phase error variance for the standard 1st-order loop is a reasonable proxy for that of higher order loops. Thus one can identify the region of approximate linear PLL operation by noting that, for the standard 1st-order loop, the

linear model [Eq. (2.4)] is reasonably accurate (within 20%) for $\rho_L > 4$, or $\sigma_\varphi < 28.6°$. Likewise, a squaring loop behaves approximately linearly for $\rho_{eq} > 4$, or $\sigma_\varphi < 14.3°$.

Note that the above results assume that all phase errors are due to constant-intensity white measurement noise. Equations (2.4) – (2.7) further assume PLL linearity. All of these assumptions are violated during severe scintillation: Amplitude fading causes variations in the loop SNR, phase changes are time-correlated, and, when attempting to track through the large, rapid phase changes associated with canonical fading, the PLL cannot be expected to operate in its linear regime. For these reasons, calculating σ_φ^2 for a PLL tracking through strong scintillation does not appear straightforward. The approach taken in [5] and [6] breaks σ_φ^2 down into three components: (1) a measurement noise component that takes amplitude fading into account, (2) a component due to dynamics in $\theta(t)$, and (3) a component due to oscillator noise. But to calculate these components, the approach in [6] invokes PLL linearity, which is violated during severe scintillation.

2.5.2 Cycle Slipping

A PLL's phase detector is periodic, meaning that it cannot distinguish between the phase errors φ and $\varphi + 2n\pi$ (non-squaring loop) or φ and $\varphi + n\pi$ (squaring loop), where n is an integer. As a result, an infinite set of stable attractors exists for the nonlinear difference equations that describe the PLL error dynamics. At low loop SNR, or during vigorous phase scintillation, the phase error can slip from one stable attractor to another, leading to infinite σ_φ^2 in the steady-state. This is the familiar cycle slip phenomenon associated with PLLs [30, 31], [29, Ch. 6].

The mean time to first cycle slip T_s is defined as the average time required for the loop phase error to reach $\pm 2\pi$ ($\pm\pi$ for the squaring loop) for the first time, starting from

an initial condition of zero phase error. For first order loops, and in other cases where cycle slips occur as isolated events, T_s is the same as the mean time between cycle slips; if cycle slips occur in bursts—as may happen for $\rho_L, \rho_{eq} < 5$ in 2nd- or higher-order loops—then T_s and the mean time between cycle slips are not related simply [31].

As with the calculation of σ_φ^2, an analytical solution for T_s has only been possible for the simple case of a 1st-order unstressed (zero static phase error) PLL driven by white Gaussian noise, in which case [27, p. 101]

$$T_s = \frac{\pi^2 \rho_L I_0^2(\rho_L)}{2B_n} \tag{2.8}$$

is the time to first slip/mean time between slips for a non-squaring loop; $I_0(\cdot)$ is a modified Bessel function of the first kind. An approximate T_s for 1st-order squaring loops obtains by substituting ρ_{eq} for ρ_L. Unstressed 2nd- and higher-order loops have lower T_s than unstressed 1st-order loops, and stressed loops are more prone to cycle slipping than unstressed loops; nonetheless, Eq. (2.8) remains a useful upper bound. For GPS applications, a 2nd- or 3rd-order loop is required to accurately track carrier phase in the presence of Doppler-induced quadratic phase growth. In fact, even the 2nd-order loop experiences significant loop stress ($\sim 1^\circ$ static phase error) during the largest GPS line-of-sight accelerations. Only the 3rd-order loop maintains near-zero static phase error for all GPS geometries. Accordingly, scintillation testbed experiments will focus on 3rd-order loops.

Phase and amplitude scintillation cause cycle slipping via two different mechanisms. The first of these—and the most common—was discussed briefly in the previous section: a squaring-loop PLL is often unable to track through the abrupt phase change associated with a canonical fade. This makes sense: in the limit as the fade depth increases, the abrupt, nearly π-rad phase transition looks like bi-phase data modulation, to which the squaring-loop PLL is insensitive by design. Hence, the PLL detects no phase

shift and a half-cycle slip occurs. In marginal cases, where the PLL might be capable of distinguishing a scintillation-induced phase transition from a data-bit-induced phase transition, the sudden drop in loop SNR increases the likelihood of a cycle slip. One can demonstrate this by shifting the phase and amplitude time histories relative to one another so that the signal power fades and the rapid phase changes are no longer aligned. Experiments show that such shifting leads to an approximate 20% decrease in cycle slips—evidence that simultaneous power fades and abrupt phase changes are a particularly challenging combination. Scintillation testbed results will show that canonical fading accounts for over 90% of equatorial-scintillation-induced cycle slips.

Prolonged amplitude fading is the second mechanism by which scintillation causes cycle slipping. This phenomenon may be considered a special case of canonical fading in which the fading time scale is elongated so that the amplitude fade is accompanied by phase dynamics that are slow compared to a typical 10-Hz PLL noise bandwidth. In this case, broadband measurement noise dominates and Eq. (2.8) applies. Cycle slips occur rarely by this mechanism. To see why, consider that the overwhelming majority of deep fades (> 15 dB) in the scintillation library's GPS data last less than 2 seconds. Assume that, during a rare 2-second fade, the received C/N_0 drops to 23 dB-Hz. For a predetection bandwidth of $1/T_a = 100$ Hz and a PLL noise bandwidth equal to $B_n = 10$ Hz, the resulting equivalent loop SNR is $\rho_{eq} = 4$. Substituting ρ_{eq} into Eq. (2.8) yields $T_s \approx 22.3$ seconds for a 1st-order loop, which implies a slip probability of less than $1/10$ over the 2-second fade. Consistent with this analysis, cycle slips due to prolonged amplitude fading are rare, amounting to less than 10% of the cycle slips in the scintillation testbed results.

2.5.3 Frequency Unlock

The general term *phase unlock* refers to single or successive cycle slips. At very low loop SNR or in extreme scintillation a PLL may never recover phase lock after a long succession of cycle slips. This phenomenon, called "drop lock" in the PLL literature, is related to the PLL's frequency pull-in range. For reasons that will become clear, the term *frequency unlock* is a more precise descriptor than drop lock for the phenomenon as it relates to the discrete-time PLLs used in modern GPS receivers.

A PLL's frequency pull-in range is the maximum frequency step input that a PLL is able to "pull in" and eventually achieve phase lock. For example, a continuous-time 1st-order non-squaring PLL has a pull-in range equal to the loop gain K [30]. For higher-order PLLs, the frequency pull-in range can be thought of as the maximum tolerable mismatch $\Delta\omega = |\omega_c - v|$ between the carrier frequency ω_c and the PLL's internal estimate of carrier frequency v, assuming that higher order loop filter states (e.g., the estimate of carrier frequency rate) are relaxed, where applicable.

Continuous-time PLLs whose loop filters contain one or more perfect integrators have an infinite frequency pull-in range [29, Ch. 8]. On the other hand, the frequency pull-in range of 2nd- and higher-order discrete-time PLLs is limited by the loop update (accumulation) interval T_a. When the frequency mismatch $\Delta\omega$ exceeds a certain threshold $\Delta\omega_m$, then v is attracted toward a stable equilibrium value that satisfies $T_a\Delta\omega = n\pi$ (non-squaring loop) or $T_a\Delta\omega = n\pi/2$ (squaring loop), $n = 1, 2, 3, \ldots$. Intuitively, these equilibrium values exist because the loop cannot detect a phase error change of $2n\pi$ (non-squaring loop) or $n\pi$ (squaring loop) between loop updates. The value of $\Delta\omega_m$ is a function of the particular loop configuration. It can be surprisingly small for PLLs common in GPS receivers: for a 3rd-order Costas loop with $T_a = 10$ ms and $B_n = 10$ Hz, $\Delta\omega_m = 81$ rad/s ≈ 13 Hz. At very low loop SNR or during vigorous scintillation,

cycle slips can occur in bursts as noise and phase dynamics force v momentarily away from ω_c. If, due to such forcing, $\Delta\omega$ exceeds $\Delta\omega_m$, then there is a high probability that v will become trapped at one of the incorrect stable equilibrium values. Thus the PLL experiences frequency unlock.

Frequency unlock and momentary phase unlock have rather different practical consequences. Unlike momentary phase unlock (i.e., cycle slipping), frequency unlock often leads to complete loss of the GPS signal link—a result of signal attenuation due to frequency detuning. If v settles on an equilibrium value such that $n \geq 2$ (non-squaring loop) or $n \geq 4$ (squaring loop), then the baseband signal power drops by more than 13 dB, making it likely that the PLL will experience further frequency detuning and eventually lose the signal entirely. Worse yet, re-acquisition may not be possible at low SNR or during scintillation. Such complete signal loss can occur even in high-quality GPS receivers during severe scintillation [4], with sobering implications for GPS-dependent systems.

2.6 The Scintillation Testbed

The scintillation testbed is a collection of software routines used to test various phase tracking strategies under realistic equatorial scintillation conditions. The testbed derives input phase and amplitude time histories from empirical scintillation library records, feeds these to a PLL under test, and observes the PLL's phase error variance and phase lock behavior. In addition, the testbed evaluates the GPS navigation bit error probability of two differential bit detection techniques under the influence of scintillation.

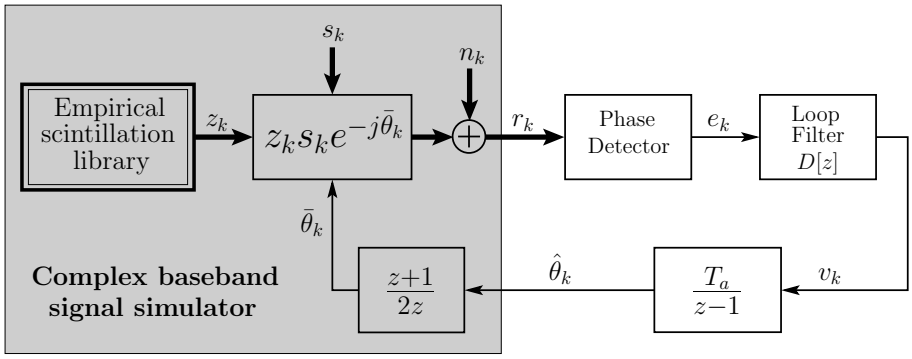

Figure 2.6: Block diagram of the scintillation testbed. Thick lines denote complex signal routing.

2.6.1 Description

The scintillation testbed is illustrated in block diagram form in Fig. 2.6. Its PLL model is an adaptation of the standard baseband model for a discrete-time PLL [32]; a GPS-specific baseband model is developed in [3]. Use is made of the z-transform to denote delays in the discrete-time signals. Routes for complex and scalar quantities are denoted respectively by thick and thin lines.

Within the gray box in Fig. 2.6 are mechanized the mixing and accumulation operations typical in a GPS receiver. The mechanization is based on the following model for the complex baseband signal r_k:

$$r_k = \frac{1}{T_a} \int_{t_{k-1}}^{t_k} [z(t)s_k + n(t)]\, e^{-j\hat{\theta}(t)} dt \tag{2.9}$$

In this model, $z(t) = \alpha(t) \exp[j\theta(t)]$ is the complex channel response function, with $\alpha(t)$ and $\theta(t)$ representing scintillation-induced amplitude and phase variations; it is assumed that $z(t)$ is normalized so that $E[|z(t)|^2] = 1$. The quantity $\hat{\theta}(t)$ is the PLL's phase estimate; $T_a = t_k - t_{k-1}$ is the accumulation interval; $n(t)$ is complex zero-mean additive white Gaussian noise; $s_k = \sqrt{E_a} \exp[j(\tilde{\theta}_k + \theta_c)]$, with $\tilde{\theta}_k \in \{0, \pi\}$, is the binary data signal over the kth accumulation interval; θ_c is the carrier phase, which is assumed constant;

and E_a is the energy per accumulation. Note that $\tilde{\theta}_k$ does not change from one accumulation interval to the next except when adjacent intervals straddle a data bit transition. Note also that $z(t)$, $n(t)$, and $\hat{\theta}(t)$ are represented here as continuous-time signals whereas they exist as discrete-time signals in modern GPS receivers. The continuous-time approximation is justified because their discrete-time sampling interval is much smaller than T_a.

Equation (2.9) is a baseband model, meaning that the nominal carrier frequency and all motion-induced Doppler shift effects are assumed to have been perfectly removed via baseband mixing. This is a realistic assumption for 3rd-order PLLs, whose static phase error is zero for a constant carrier frequency rate. Of course, the testbed could easily be modified to include the effects of motion-induced Doppler shift or receiver clock drift.

The phase estimate $\hat{\theta}(t)$ varies linearly and, for practical PLL bandwidths, slowly over the accumulation interval. Hence r_k may be approximated as

$$\begin{aligned} r_k &\approx \frac{e^{-j\bar{\theta}_k}}{T_a} \int_{t_{k-1}}^{t_k} [z(t)s_k + n(t)]\, dt \\ &= z_k s_k e^{-j\bar{\theta}_k} + n_k \end{aligned} \tag{2.10}$$

where z_k and $\bar{\theta}_k = [\hat{\theta}(t_k) + \hat{\theta}(t_{k-1})]/2$ are the respective averages of $z(t)$ and $\hat{\theta}(t)$ over the accumulation interval, and n_k is an element of a zero-mean complex Gaussian noise sequence with variance $E[n_k^* n_j] = N_0 \delta_{kj}$. Under the assumption that $E[|z(t)|^2] = 1$, the SNR per accumulation in the absence of scintillation (i.e., when $S_4 = 0$) is given by $E_a/N_0 = T_a C/N_0$. In the remainder of this paper, the values of E_a/N_0 and C/N_0 when $S_4 = 0$ will be referred to as the nominal E_a/N_0 and C/N_0. For the GPS L_1 data, the effective nominal carrier-to-noise ratio is less than C/N_0 because of additional noise power that is already present in the data. The final value of C/N_0 is calculated based on N_0 and on the effective C/N_0 of each GPS L_1 record, an estimation strategy for which is described in the Appendix. Also, in general, when $S_4 > 0$ the variations in $z(t)$ over the

accumulation interval lead to $\Omega \equiv E[|z_k|^2] < 1$. Thus the average SNR per accumulation $\bar{\gamma} \equiv \Omega E_a/N_0$ is slightly less than E_a/N_0.

To generate the averages z_k, the scintillation library's 500-Hz Wideband data samples z_{Wj} and 100-Hz GPS L_1 data samples z_{Gj} are treated slightly differently. Both data types are initially normalized so that $E[|z_{Wj}|^2] = E[|z_{Gj}|^2] = 1$. The Wideband data samples are then directly averaged to approximate the z_k, i.e.,

$$z_k \approx \frac{1}{N_W} \sum_{j=(k-1)N_W}^{kN_W-1} z_{Wj} \quad k = 1, 2, 3, ... \tag{2.11}$$

, where $N_W = 500 \cdot T_a$ is the number of Wideband samples per accumulation. Since the scintillation testbed only considers $T_a \in \{10, 20\}$ ms, at least 5 samples are used to generate each average, making Eq. (2.11) a close approximation.

Because the GPS L_1 samples z_{Gj} are derived from actual 100-Hz baseband accumulations, they can be assumed to represent averages over $T_a = 10$ ms. Thus, no averaging is required to represent the z_k corresponding to $T_a = 10$ ms. However, the z_{Gj} must be attenuated to reflect the condition $\Omega \equiv E[|z_k|^2] < 1$ mentioned above. For this, Ω is estimated based on its dependence (detailed in Section 2.9.2) on S_4 and τ_0. Then for $T_a = 10$ ms, the z_k are approximated as

$$z_k \approx \sqrt{\hat{\Omega}}\, z_{Gk} \tag{2.12}$$

where $\hat{\Omega}$ is an estimate of Ω in the neighborhood of z_{Gk}. For $T_a = 20$ ms, two of the 10-ms z_k from Eq. (2.12) are averaged to approximate the 20-ms z_k. The outputs z_k of the empirical scintillation library block in Fig. 2.6 are taken to represent the approximations derived from Eqs. (2.11) and (2.12).

The three blocks to the right of the gray box in Fig. 2.6 are particular to the PLL under test and will be treated in the next subsection. In addition to the functions depicted in Fig. 2.6, the scintillation testbed evaluates the bit error probability of binary differential

phase shift keying (binary DPSK) bit detection. Binary DPSK makes a decision about the sign of a data bit based on the phase change between two adjacent data bit intervals. As will be shown, there exists a close connection between binary DPSK bit errors and cycle slips for GPS signal tracking during severe equatorial scintillation. A "Fast DPSK" scheme (proposed in [33]) that does differential detection using only one sub-bit-length accumulation interval on each side of a data bit edge is also evaluated. Both DPSK techniques operate on the baseband signal r_k, which implies knowledge of the carrier frequency ω_c. In practice, ω_c can be estimated using a low-bandwidth frequency tracking loop.

The testbed also includes routines for cycle slip and frequency unlock detection. The correct way to measure the mean time to first slip T_s empirically for the case of white phase noise is demonstrated in [34] where, after each slip, the phase tracking loop is re-initialized in perfect steady-state lock so that it experiences no transients. But mean time between cycle slips, not mean time to first slip, is the quantity of interest for PLLs operating in the presence of scintillation. The two are not equivalent when slips occur in clumps, as can be the case for 2nd- and higher-order loops during severe scintillation or at low loop SNR. Thus, the testbed's cycle slip detection routine measures mean time between slips, and T_s will be assumed to refer to this quantity in testbed results.

The measurement of T_s depends on a somewhat arbitrary definition of a cycle slip. The following procedure, which leads to cycle slip counts that agree with a visual inspection, has been adopted for the scintillation testbed. A phase error time history $\varphi_k = \theta_c + \theta(t_k) - \hat{\theta}(t_k)$ is first constructed where for $\theta(t_k)$ is substituted the phase of the original z_{Gj} or z_{Wj} samples taken at times nearest each t_k. The sequence φ_k is then 1.5-Hz low-pass filtered to produce $\tilde{\varphi}_k$, from which the differences $b_k = |\tilde{\varphi}_k - \tilde{\varphi}_{k-N}|$ are computed, where N is chosen such that the differenced elements are separated by the

rise time of the low-pass filter. A cycle slip is declared when b_k exceeds $2\beta\pi$ rad (non-squaring loops) or $\beta\pi$ rad (squaring loops), with $\beta = 3/5$. Frequency unlock is declared after 5 successive seconds of cycle slipping, a rule that also agrees closely with visual inspection. The time interval of each testbed run is chosen to be long enough that loop re-initialization at the beginning of each run has a negligible effect on the mean time between cycle slips or frequency unlock. Values of T_s greater than the time interval of each individual testbed run are calculated by averaging cycle slip counts over repeated runs.

It was noted previously that whole cycle slips, although rare, are present in both Wideband and GPS records in the scintillation library. These occur during particularly deep canonical fades where, for example, instead of tracking an abrupt half-cycle upgoing phase change, the original PLL tracks an abrupt half-cycle downgoing phase change, resulting in a whole cycle slip. From the point of view of a PLL being evaluated in the scintillation testbed, the true (upgoing) phase change and the tracked (downgoing) phase change are equally challenging to track. Hence, the whole cycle slips do not diminish the usefulness of the data in the scintillation library.

2.6.2 Validation

Besides agreement with visual inspection, the scintillation testbed has been checked against Viterbi's theoretical results for the first-order continuous-time PLL operating in white Gaussian noise [27]. For these tests, T_a was set to 1 ms and a 1st-order $D[z]$ was designed using a constant update approximation so that the PLL's closed-loop behavior is nearly equivalent to that of the analog PLL assumed in Viterbi's analysis. Tests were conducted using simulated white Gaussian noise (no phase or amplitude scintil-

lation) over the same time intervals and loop SNR values used later to evaluate PLLs in scintillation. The test results showed close agreement with theory: the experimental distribution of φ_k modulo 2π was practically indistinguishable from its theoretical counterpart, and the experimental T_s at each SNR tested was within 10% of the theoretical value [Eq. (2.8)] when compared on a logarithmic plot. Likewise, experimental bit error probabilities for the testbed's binary DPSK bit detector were shown to be essentially identical to the theoretical values for the additive white Gaussian noise channel (given, for example, in [35, Ch. 7]).

A validation of the testbed's DPSK bit detector was also carried out in the presence of scintillation (not just white measurement noise). For this, a GPS L_1 record from the scintillation library was processed in the testbed. The number of errors in the bit stream produced by the testbed's DPSK bit detector was noted. This number was then compared to the number of errors found in the navigation data output of the software receiver used to process the raw data samples from which the GPS L_1 record was originally derived (see the Appendix for details on the software receiver and the preliminary data processing). The two bit error counts were found to be in reasonable agreement, indicating that the scintillation testbed recreates the conditions that cause scintillation-induced navigation bit errors.

2.7 Example PLLs

The scintillation testbed is a generalized tool for evaluating the performance of carrier tracking strategies in the presence of scintillation. Any carrier tracking loop that operates on the baseband signal r_k can be tested for robustness and evaluated—under controlled scintillation conditions—against an array of alternative strategies. To illus-

trate its usefulness and to gain insight into the effects of scintillation on typical PLLs used in GPS receivers, a set of example PLLs was tested. Each PLL in the set has a different combination of phase detector and loop filter.

The phase detectors considered in the set of example PLLs are given in Table 2.2. All detectors make use of the in-phase $I_k = \mathrm{Re}(r_k)$ and quadrature $Q_k = \mathrm{Im}(r_k)$ components of r_k, which are simulations of the usual accumulations produced by the baseband mixer and integrate-and-dump accumulators of a digital GPS receiver. The two-quadrant arctangent (AT), decision directed (DD), and conventional Costas (CC) detectors are standard squaring-loop phase detectors used in GPS receivers [36, 37]. The AT and CC detector make direct use of the I_k and Q_k components whereas the DD detector attempts to wipe off data bit modulation by estimating the current data bit value as $\mathrm{sign}(I_{m,k})$, where $I_{m,k}$ is the sum of the in-phase components of all accumulations up to time t_k within the current (mth) data bit interval. The decision-directed four-quadrant arctangent (DD-AT) detector is a hybrid of the DD and AT detectors in which data bit wipeoff via $\mathrm{sign}(I_{m,k})$ enables full four-quadrant phase detection. If the accumulation interval T_a equals the GPS data bit interval $T_b = 20$ ms, then the AT and DD-AT detectors are equivalent.

The dot-product four-quadrant arctangent (DP-AT) detector is identical to the DD-AT detector except that data bit wipeoff is based on differential bit detection. Like binary DPSK bit detection, the DP-AT phase detector makes a decision about the sign of the current data bit by measuring—via a dot product—the phase change between the previous and the current data bit interval. Suppose it is known that $\tilde{d}_{m-1}$ is the transmitted data bit over the $(m-1)$th data bit interval. Then the DP-AT phase detector's estimate $d_{m,k}$ of the value of the data bit during the accumulation ending at time t_k within the mth

Table 2.2: Phase Detectors for the Set of Example PLLs

Phase Detector	**Abbr.**	**Definition**
Two-quadrant arctangent	AT	$e_k = \text{atan}(Q_k/I_k)$
Decision-directed four-quadrant arctangent	DD-AT	$e_k = \text{atan2}[Q_k \cdot \text{sign}(I_{m,k}), I_k \cdot \text{sign}(I_{m,k})]$
Conventional Costas	CC	$e_k = I_k \cdot Q_k$
Decision directed	DD	$e_k = Q_k \cdot \text{sign}(I_{m,k})$
Dot-product four-quadrant arctangent	DP-AT	$e_k = \text{atan2}(Q_k d_{m,k}, I_k d_{m,k})$

data bit interval is

$$d_{m,k} = \begin{cases} -\tilde{d}_{m-1}, & \text{Re}(r^*_{m,k}\tilde{r}_{m-1}) < 0 \\ \tilde{d}_{m-1}, & \text{Re}(r^*_{m,k}\tilde{r}_{m-1}) \geq 0 \end{cases} \tag{2.13}$$

where $r_{m,k} = I_{m,k} + jQ_{m,k}$ is the sum of all r_k up to time t_k within the mth data bit interval and $\tilde{r}_{m-1}$ is the sum of all r_k within the $(m-1)$th data bit interval. The value $d_{m,k}$ is used to wipe off data bit modulation from each r_k during the mth data bit interval, as indicated in Table 2.2. At the end of the mth data bit interval, $d_{m,k}$ becomes $\tilde{d}_m$ and $r_{m,k}$ becomes $\tilde{r}_m$. For added stability, the DP-AT detector is designed to revert to the DD-AT detector when $\text{Re}(r^*_{m,k}\tilde{r}_{m-1}) \approx 0$. It will be shown that the DP-AT detector is well suited for making phase measurements during severe equatorial scintillation.

The digital loop filter $D[z]$ takes the phase detector outputs e_k and estimates the phase rate v_{k+1} for the $(k+1)$th accumulation interval according to

$$v_{k+1}T_a = K_1 e_k + K_2 \sum_{i=1}^{k} e_i + K_3 \sum_{i=1}^{k} \sum_{j=1}^{i} e_j + ... \tag{2.14}$$

where the sequence extends to the K_N term for an Nth-order loop filter, which yields Nth-order closed-loop PLL dynamics. The loop constants K_n are determined according

to the controlled-root formulation for digital PLL design introduced in [34]. Loops of order 1 through 3 can be selected, with the design parameter $T_a B_n$ ranging from 0.01 to 0.4. The loop filter's output v_k passes through the integration block $[T_a/(z-1)]$ to generate the phase estimate $\hat{\theta}_k$.

All PLLs in the example set are designed to have a constant bandwidth, meaning that their noise bandwidth B_n remains constant for small phase errors despite changes in the fading amplitude $\alpha_k = |z_k|$. When connected to a loop filter $D[z]$ with fixed coefficients, the AT-type phase detectors (AT, DD-AT, DP-AT) automatically deliver a constant B_n because, in the absence of noise, the arctangent function is insensitive to changes in α_k. The outputs e_k of the DD and CC phase detectors, on the other hand, are sensitive to changes in α_k. They must be normalized by α_k (DD) or α_k^2 (CC) to yield a B_n that, for small phase errors, is equal to the constant B_n of the AT-type detectors. In the scintillation testbed, such normalization is accomplished by estimating α_k^2 as

$$\hat{\alpha}_k^2 = \langle r_k^* r_k \rangle - N_0 \tag{2.15}$$

where the time average $\left\langle r_k^* r_k \right\rangle$ is mechanized using a first-order low-pass filter with a time constant of 0.1 seconds.

2.8 Testbed Results and Discussion

The scintillation testbed has been used to compare the set of example PLLs described above for various loop orders, noise bandwidths, and update intervals. Such comparison tests are used to identify a baseline loop configuration with which to evaluate scintillation effects. Results are presented in Section 2.8.1. Thereafter, for the baseline loop order, noise bandwidth, and update interval, a more extensive set of results is given in Sections 2.8.2 and 2.8.3 for tests conducted in the absence of scintillation (mea-

surement noise only) and in the presence of scintillation (both measurement noise and scintillation-induced phase and amplitude variations). The latter results will indicate a connection between cycle slips and DPSK-detected bit errors. This connection will be exploited in subsequent sections to develop a model that can be used to approximately predict cycle slips for the broad class of typical GPS PLLs represented by the set of example PLLs.

Performance tests of two elaborate variable-bandwidth phase tracking strategies have also been conducted using the scintillation testbed. The results of these tests, given in Section 2.8.4, will suggest a limit on the cycle slip performance of any unaided PLL in severe equatorial scintillation.

2.8.1 Loop Order, Update Interval, and Noise Bandwidth Comparisons

For the following results, comparison tests have been performed by varying one parameter (e.g., loop order) at a time from a baseline configuration with loop order 3, update (accumulation) interval $T_a = 10$ ms, and noise bandwidth $B_n = 10$ Hz. The phase detectors employed are those described in Section 2.7. Measurement noise n_k is added to simulate a nominal C/N_0 value of 43 dB-Hz for the Wideband data, and nominal C/N_0 values between 40 and 44 dB-Hz for the GPS data, with a mean of 43 dB-Hz. Each PLL configuration is tested on the entire 7.5-hour scintillation library. Further details on the test conditions are given in Section 2.8.3.

Loop order: PLLs of order 2 and 3 were tested. No significant difference in T_s was found. This was true whether all scintillation library data or only GPS L_1 data were

used. On the other hand, the 2nd-order loop did show a reduced rate of frequency unlock across all phase detectors. However, the 3rd-order loop's ability, and the 2nd-order loop's inability, to maintain zero static phase error when tracking quadratic phase growth (not simulated for the present testbed results) would tend to neutralize this advantage. Therefore, 2nd- and 3rd-order loops appear to be roughly equally suited for GPS phase tracking in scintillation.

Loop update interval: PLLs with $T_a = 10$ ms and $T_a = 20$ ms were tested. It was found that for all phase detectors an increase in T_a from 10 to 20 ms worsened (shortened) T_s. Moreover, for all but the DP-AT PLL, the incidence of frequency unlock increased substantially—consistent with a reduced pull-in threshold $\Delta\omega_m$ (cf. Section 2.5.3). Thus, $T_a = 10$ ms appears preferable to $T_a = 20$ ms for phase tracking in scintillation.

Loop noise bandwidth: PLLs with $B_n = 7.5$, $B_n = 10$ and $B_n = 15$ Hz were tested. In general, PLLs with higher B_n experience fewer cycle slips in severe scintillation at high nominal C/N_0 because they are better able to track vigorous phase fluctuations than lower-bandwidth PLLs. As nominal C/N_0 decreases below 40 dB-Hz, however, measurement noise effects become important and a wide bandwidth loop becomes comparatively more prone to cycle slipping. Near a nominal C/N_0 of 43 dB-Hz, an increase in B_n from 7.5 to 10 Hz resulted in a marginal improvement (increase) in T_s but also caused an increase in frequency unlock for all phase detectors. As B_n was further widened to 15 Hz, T_s improved still further but the rate of frequency unlock increased dramatically. Hence, it appears that B_n values from 7.5 to 10 Hz are a good choice for operating in severe scintillation at typical nominal values of C/N_0.

In view of the above results, a baseline configuration with loop order 3, $T_a = 10$ ms, and $B_n = 10$ Hz was chosen for the more thorough tests that follow.

2.8.2 PLL Behavior in the Absence of Scintillation

It is instructive to contrast the behavior of the example PLLs in the absence of scintillation (white measurement noise only) with their behavior during scintillation. It will be shown that scintillation-free and scintillation tests that produce equivalent σ_φ are not equally challenging for the PLL under test.

To test PLL behavior in the absence of scintillation, the scintillation library's complex outputs z_k are set to unity for all k; the white measurement noise simulated by n_k remains as described in Section 2.6.1. Runs of 100-second length have been iterated 3000 times with C/N_0 ranging from 21 to 30 dB-Hz. Cycle slip results are presented in Fig. 2.7, which plots the normalized mean time between cycle slips $T_s B_n$ vs. the equivalent loop SNR ρ_{eq}. For convenience, the horizontal axis is also expressed in terms of C/N_0, which is related to ρ_{eq} via Eqs. (2.4), (2.5), and (2.7), and in terms of empirical values of σ_φ for the DD-AT PLL. Note that large phase errors at these low values of ρ_{eq} cause the empirical σ_φ values to be larger than predicted by the linear approximations expressed in Eqs. (2.6) and (2.7). Also note that to obtain sensible values of σ_φ in the presence of cycle slips, the phase errors φ_k are taken modulo π. The same is true for all values of σ_φ presented hereafter.

The results in Fig. 2.7 assume the baseline loop order and update interval (3rd order and $T_a = 10$ ms), but apply generally to $B_n \lesssim 20$ Hz. Second-order loops and loops with $T_a = T_b = 20$ ms have also been tested (recall that T_b is the GPS data bit interval). All loops demonstrated a marginal reduction in cycle slips with a change in T_a from 10 to 20 ms. No significant reduction was noted, over the range of C/N_0 values tested, due to a change from 3rd-order to 2nd-order loops.

Theoretical values of $T_s B_n$ vs. ρ_{eq} for a continuous-time 1st-order PLL (dashed

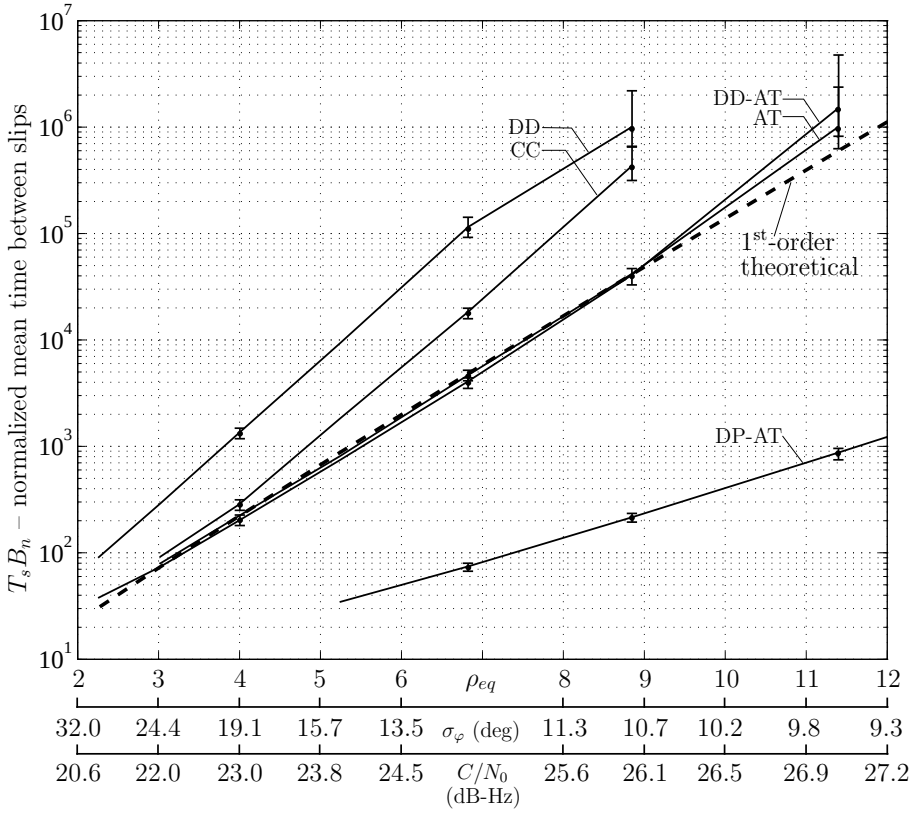

Figure 2.7: Experimental normalized mean time between cycle slips as a function of ρ_{eq} (linear scale) for several 3rd-order PLLs with $T_a = 10$ ms operating in the presence of complex white Gaussian noise. The horizontal axis scale is also expressed in terms of the standard deviation σ_φ of the phase error φ_k modulo π, and in terms of the carrier-to-noise ratio C/N_0, assuming $B_n = 10$ Hz. The values of σ_φ correspond to the DD-AT phase detector but also hold approximately for the CC and AT detectors. The dashed line shows the theoretical $T_s B_n$ for a continuous-time 1st-order PLL [Eq. (2.8)]. Error bars indicate two standard deviations about the estimated values.

line in Fig. 2.7) agree closely with the values for the DD-AT and AT PLLs, which demonstrates that Eq. (2.8) (with ρ_{eq} substituted for ρ_L) is a useful approximation for these PLLs over the range of ρ_{eq} shown. In terms of cycle slips, the DD and CC phase detectors have a decided advantage for the measurement-noise-only case. This result can be understood by noting that large phase errors cause the nonlinear (sinusoidal) phase detector characteristic of the DD and CC detectors effectively to reduce the associated

PLL's noise bandwidth relative to PLLs based on the AT-type detectors, which have a linear characteristic over $-\pi/2 \leq \varphi_k < \pi/2$, with sharp nonlinear breaks at $-\pi/2$ and $\pi/2$. In the absence of actual variations in the received phase, PLLs with a lower effective B_n experience fewer cycle slips.

Among the phase detectors tested, the DP-AT detector suffered the most cycle slips at each value of ρ_{eq}. This result is intuitive: it can be shown that for the additive white Gaussian noise case the differentially-detected bit estimates $d_{m,k}$ that are used to do data bit wipeoff in the DP-AT phase detector are more prone to errors than the coherently-detected bit estimates $\text{sign}(I_{m,k})$ used in the DD and DD-AT detectors.

2.8.3 PLL Behavior in the Presence of Scintillation

Tests of PLL behavior in the presence of scintillation are conducted using the standard scintillation library outputs z_k. Scintillation data are divided into 30-second records so that the signal statistics over each record are reasonably stationary. Measurement noise n_k is added to simulate nominal C/N_0 values ranging from 35 to 55 dB-Hz. Each 30-second record at each value of C/N_0 is iterated 30 times with different measurement noise realizations to accumulate enough data for a statistical analysis of the results. Note, however, that the GPS L_1 results have measurement noise realizations that change only in part between different runs because the data's intrinsic noise component is invariant.

In all, tests have been conducted on 885 30-second scintillation records with S_4 values ranging from 0.02 to 1.3. Wideband and GPS L_1 results are presented separately to avoid conflating results from inputs with different noise properties. On the other hand, Wideband UHF and L-band results have been lumped together despite the inputs' dif-

ferent scintillation properties. This was done because there are not enough intervals of severe scintillation in the Wideband L-band data for clear trends to emerge, and because, for the relationships to be presented in this section, the L-band data generally fit trends established by the UHF data. The results given here apply to the baseline loop configuration (3rd-order loop, $T_a = 10$ ms, and $B_n = 10$ Hz).

The relationships between S_4 and the primary PLL performance metrics, namely, cycle slips and σ_φ^2, are shown in Figs. 2.8 and 2.9. These results are for the DD-AT phase detector but are approximately representative of the other phase detectors tested. Each point in Figs. 2.8 and 2.9 corresponds to a different 30-second record from the scintillation library and represents an average over 30 test iterations. Fig. 2.8 presents results in terms of cycle slip rate on the left vertical axis, and, for convenience, in terms of T_s on the right vertical axis. As would be expected, a general increase in the rate of cycle slips accompanies increasing S_4. The lack of cycle slips below $S_4 \approx 4$ suggests that, whatever its other characteristics (e.g., fading time scales), scintillation with $S_4 \lesssim 0.4$ can be considered benign. Also, for convenience in the following, severe scintillation will be roughly identified with $S_4 > 0.6$. The wide spread in cycle slip rate for $S_4 > 0.6$ indicates that records with equivalent measured S_4 are not necessarily equally challenging to track. This is true within the GPS L_1 records but is especially striking in the comparison between GPS and Wideband data. The implications of this spreading for scintillation effects modeling will be discussed in Section 2.9.

It was found in initial processing that GPS data bit parity failures—which can be considered a rough proxy for cycle slips—were predominantly associated with canonical fades. Experiments with the scintillation testbed confirmed this result: over 90% of the slips underlying the data in Fig. 2.8 were induced by canonical fades.

Fig. 2.9 shows how σ_φ, the standard deviation of the phase measurement error

modulo π, increases with increasing S_4, a dependence that is due both to the fade-induced reductions in loop SNR and to phase scintillation with frequency components that exceed the PLL's B_n. The difference in σ_φ at low S_4 between the Wideband and GPS data reflects the latter's irreducible noise component, which the analysis treats as a dynamically-varying true phase that the PLL does not exactly track. The large values of σ_φ at high S_4—in some cases exceeding 30 deg for Wideband data and 13 deg for GPS L_1 data—contribute to the degradation of carrier-phase-dependent GPS systems during strong scintillation.

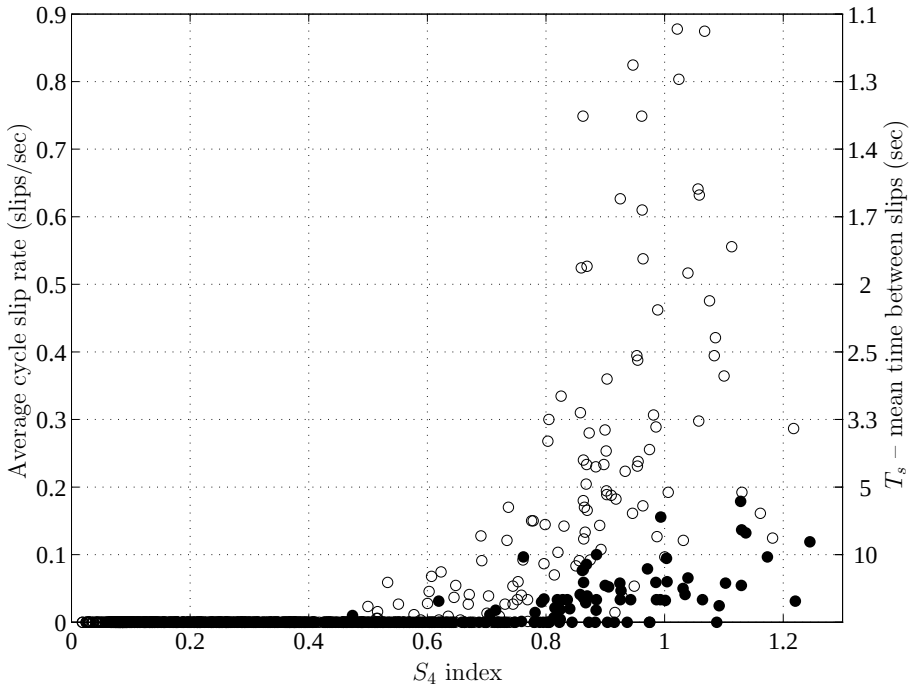

Figure 2.8: Average DD-AT PLL cycle slip rate over each 30-second test record vs. S_4 for the Wideband data at C/N_0 = 43 dB-Hz (open circles) and for the GPS L_1 data within 40 < C/N_0 < 44 dB-Hz with mean C/N_0 = 43 dB-Hz (filled circles). The right vertical axis expresses the cycle slip rate in terms of T_s.

Fig. 2.10 plots T_s (solid lines) and the mean time between bit errors T_e (dashed lines) as functions of nominal C/N_0 for Wideband data in the severe scintillation regime ($S_4 > 0.6$). For clarity of presentation, error bars are not shown. Standard deviations for

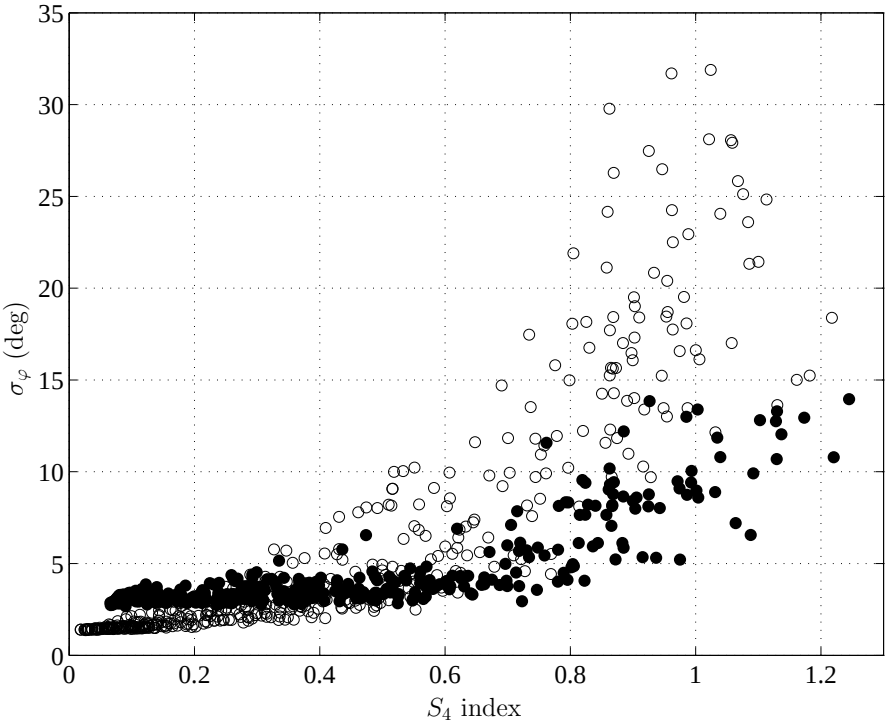

Figure 2.9: Standard deviation of DD-AT PLL phase error modulo π over each 30-second test record vs. S_4 for the Wideband data at C/N_0 = 43 dB-Hz (open circles) and for the GPS L_1 data within 40 < C/N_0 < 44 dB-Hz with mean C/N_0 = 43 dB-Hz (filled circles).

all curves are less than 0.4 seconds at C/N_0 = 35 dB-Hz and 1 second at C/N_0 = 55 dB-Hz. The range of nominal C/N_0 values considered in Fig. 2.10 is meant to span the worst to best case C/N_0 values that a terrestrial receiver would see in open-sky conditions. Empirical σ_φ values for the DD-AT PLL are given along the upper horizontal axis. One might think that these values appear too small to be associated with such high cycle slipping rates, but one must bear in mind that it is the intermittent abrupt phase changes, not just an overall high σ_φ, that drives the slipping.

Compared with the measurement-noise-only case (Fig. 2.7), the phase detector performance ordering in Fig. 2.10 is nearly inverted, with the DP-AT phase detector now experiencing fewer cycle slips than the other detectors. Such a reversal in performance

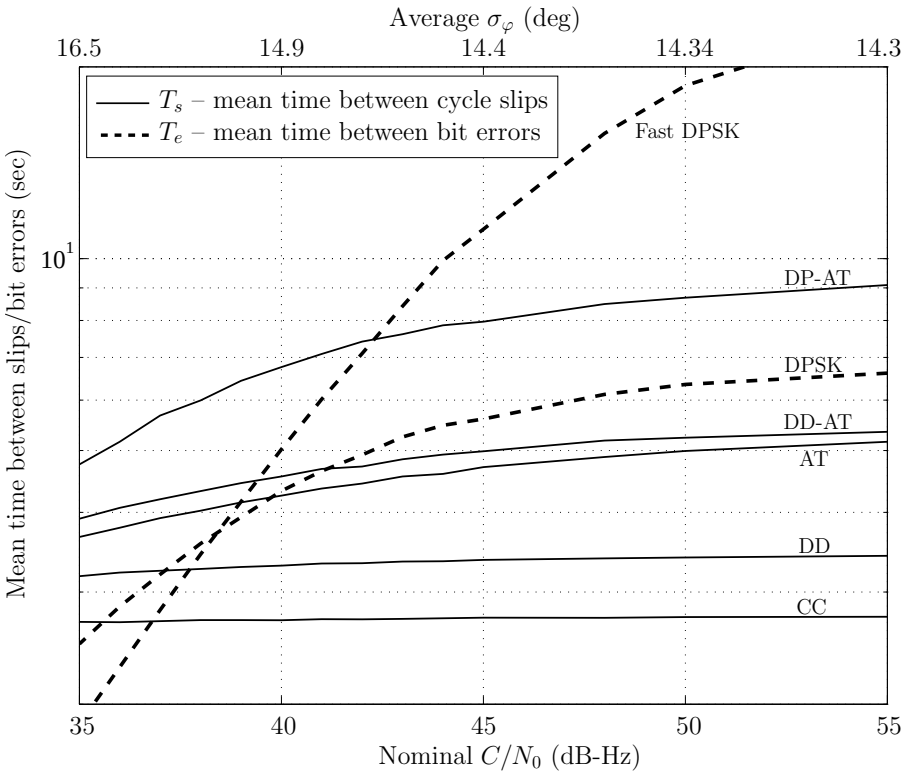

Figure 2.10: Experimental mean time between cycle slips T_s as a function of nominal C/N_0 (dB-Hz) for several PLLs operating in severe scintillation ($S_4 > 0.6$). Input scintillation data are Wideband UHF and L-band records from the empirical scintillation library. The horizontal axis scale is also expressed in terms of the standard deviation σ_φ (deg) of the phase error φ_k modulo π (upper axis). The values of σ_φ correspond to the DD-AT phase detector but also hold approximately for the AT and DP-AT detectors. The dashed lines give the mean time between bit errors T_e for binary DPSK and Fast DPSK bit detection.

is best understood in terms of the PLL's effort to drive the quadrature component Q_k of r_k to zero. During an extreme canonical fade, the phase of the complex scintillation z_k can change by nearly π rad from one data bit interval to the next. In this case, none of the phase detectors can distinguish between a scintillation-induced phase change and a data-bit-induced phase change: a cycle slip results. In less extreme (slower and shallower) canonical fades, however, the DP-AT detector has an advantage. During this kind of fade, the baseband phasor r_k is dislodged from its nominal tracking orientation

(aligned with the real axis in the complex plane) and rotates toward the imaginary axis; but as long as phase scintillation and noise do not cause r_k to rotate more than $\pi/2$ rad in one data bit interval, then the DP-AT detector decides the current bit sign correctly and thus avoids a cycle slip. In contrast, the non-differential phase detectors (DD-AT, AT, DD, and CC) almost always slip a cycle if, due to phase scintillation and noise, r_k rotates across the imaginary axis—no matter how slowly the rotation occurs. Hence, the non-differential phase detectors rely on a wide noise bandwidth B_n to drive r_k safely to its nominal tracking orientation, whereas the DP-AT detector allows r_k to rotate up to π rad away from the real axis, so long as it rotates no more than $\pi/2$ rad per bit interval. In short, the DP-AT phase detector experiences fewer cycle slips because it is better able to tolerate large instantaneous phase errors.

The testbed's demonstration that the DP-AT PLL performs well during severe scintillation is consistent with the claim advanced in [33] that differential bit detection techniques are expected to outperform coherent detection techniques during scintillation. The claim is based on the hypothesis that scintillation can be classified as fast fading relative to the GPS data bit interval $T_b = 20$ ms. The flattening of the T_e curves in Fig. 2.10 at high nominal C/N_0 indicates an irreducible bit error probability. Such limiting behavior is indeed consistent with fast fading [38], [24, Ch. 8].

Besides its role as a relatively robust phase tracking strategy, the DP-AT PLL offers an important insight into cycle slipping: Errors in the differentially-detected bit estimates $d_{m,k}$ tend to cause the DP-AT PLL to slip cycles. Conversely, if the $d_{m,k}$ are error-free, then the DP-AT PLL tends to avoid cycle slips. This connection is evident in Fig. 2.10 where, as an accessible proxy for errors in $d_{m,k}$, errors in DPSK-detected data bits are used. The dashed DPSK curve indicates that the mean time between bit errors T_e for DPSK detection serves as a useful lower bound for the DP-AT PLL's T_s. Likewise,

the Fast DPSK curve suggests that further cycle slip immunity at high nominal C/N_0 can be attained by reducing the interval over which phase changes are detected. The connection between DPSK-detected bit errors and cycle slips will be developed into a scintillation effects model in later sections.

Only Wideband data were used to generate the curves in Fig. 2.10 because of the difficulty in setting precise C/N_0 values for tests with the GPS data. Nonetheless, useful results for T_s and T_e are obtained from the GPS data by averaging over all 30-second records of severely scintillating GPS L_1 data ($S_4 > 0.6$) whose nominal C/N_0 values fall within the range $40 < C/N_0 < 44$ dB-Hz. The mean value of C/N_0 for records within this range is $C/N_0 = 43$ dB-Hz. As summarized in Table 2.3, such averaging of the GPS data yields the same phase detector performance ordering as was noted with the Wideband data, albeit with an approximately 4-fold improvement in T_s and T_e. Also, the mean time between DPSK bit errors (36.8 seconds) is consistent with its previously noted role as lower bound to the DP-AT PLL's T_s (43.3 seconds).

Table 2.3: Average T_s and T_e for severely scintillating GPS L_1 data

Phase Detection		Bit Detection	
Detector	T_s (s)	Detector	T_e (s)
DP-AT	43.3	Fast DPSK	106.3
DD-AT	37.0	DPSK	36.8
AT	33.6		
DD	22.1		
CC	15.7		

Frequency unlock statistics have also been collected over all 30-second records with $S_4 > 0.6$. At a nominal $C/N_0 \sim 43$ dB-Hz, the DP-AT PLL's mean time between

frequency unlock was 1.6 and 2.2 hours for the Wideband and GPS data, respectively. The AT and CC phase detectors fared slightly worse than this, whereas the DD and DD-AT phase detectors never experienced frequency unlock in 55 hours of iterated runs. The DD-AT PLL appears to be a good alternative to the DP-AT PLL if one is willing to trade a slight decrease in T_s for a much higher resistance to frequency unlock.

2.8.4 Variable-bandwidth PLLs and Apparent PLL Performance Limitations

Other phase tracking strategies more exotic than the example PLLs were also evaluated in the scintillation testbed. The first of these is the Kalman-Filter based PLL (KFPLL) developed in [39] and tested in [3]. The KFPLL's functionality encompasses the phase detector and loop filter blocks of Fig. 2.6. It achieves good performance at low C/N_0 by optimally adapting its loop bandwidth to C/N_0 and by using a hypothesis testing approach for resolving the data-bit-induced phase ambiguity. As demonstrated in [3], the KFPLL's adaptive bandwidth scheme makes it good at avoiding frequency unlock. On the other hand, the scintillation testbed showed that the KFPLL's cycle slip performance is generally worse than that of standard constant-bandwidth PLLs (like those in the example set) because, by reducing B_n during a canonical fade, the KFPLL is less able to track the rapid phase change.

A modified KFPLL was also considered, in which a simple scintillation model expressed in terms of interfering phasors is incorporated into the filter dynamics. When the modified KFPLL detects the onset of a canonical fade, it switches from a quiescent to a fading signal model. After the fade, it employs a hypothesis test to decide whether the phase change was up- or down-going. This method showed only marginal improvement

in T_s compared to the much simpler DP-AT PLL from the example set. Here again, canonical fading is the problem: in deep canonical fades, the costs associated with the up- and down-going hypotheses are nearly equal, making a decision based on hypothesis testing only slightly better than random.

To date, it appears that unless a PLL is supplied with additional information, it cannot be expected to perform much better during scintillation than the example set's DP-AT PLL for typical nominal values of C/N_0. One obvious approach to improving cycle slip performance is navigation data bit aiding. In this approach, the true navigation data bit sequence is obtained by some means and used to flawlessly wipe off the data modulation, just as was done in after-the-fact processing to generate the GPS L_1 records in the scintillation library. Slips can now occur only in full-cycle increments, meaning that the half-cycle canonical-fade phase shifts can be tracked. Moreover, the PLL now operates as a non-squaring loop; hence, its loop SNR increases by approximately 6 dB [cf. Eq. (2.7)], leading to a decrease in cycle slips due to measurement noise [cf. Eq. (2.8)]. Testbed results indicate that in severe scintillation ($S_4 > 0.6$) and at a nominal $C/N_0 \approx 43$ dB-Hz, perfect data bit wipeoff extends T_s by a factor greater than 65.

2.9 Scintillation Effects Modeling

The measure of a good model for scintillation effects on phase tracking is its ability to predict PLL behavior; specifically, to predict σ_φ^2 and T_s. Emphasis will be focused here on predicting T_s because, whereas an increase in σ_φ^2 gradually degrades performance, a cycle slip represents a sudden—and likely more consequential—upset to a carrier-phase-dependent GPS system. The scintillation effects modeling challenge can be posed as follows: Given a time history $z(t)$ of complex signal scintillation, extract the simplest

statistical description sufficient to predict the expected cycle slip performance within a class of standard PLLs.

2.9.1 Various Approaches to Scintillation Effects Modeling

As a first solution to the modeling challenge, one might consider developing a cycle slip prediction model based solely on the most common scintillation statistic, namely, S_4. A glance at Fig. 2.8 reveals the problem with this approach: the wide spread in cycle slips for $S_4 > 0.6$ implies that, by itself, S_4 cannot be made to explain nor accurately predict cycle slipping. Large differences in the measured slip rate at equivalent measured S_4 levels imply that there exist time series statistics relevant to phase tracking that are not captured by S_4. In other words, the S_4 index doesn't capture the fact that the Wideband records—and some GPS L_1 records—have fast fading time scales (low τ_0) that make the data hard to track.

Another strategy would be to augment S_4 with a bulk phase scintillation statistic such as the variance of the true phase time history σ_θ^2 or—even more descriptive—with the spectral strength and slope parameters T and p. References [5] and [6] adopt this approach: values for S_4, T and p are used to estimate the phase error variance σ_φ^2 of a PLL with a certain order and B_n; σ_φ^2, in turn, is used to predict T_s.

This approach seems sensible. Consider Fig. 2.11, which plots the average cycle slip rate vs. σ_φ over each 30-second record in the scintillation library. Clearly, there exists a strong correlation between σ_φ and cycle slips for $\sigma_\varphi > 5$ deg. What is more, the Wideband data and the GPS data appear to follow the same trend, meaning that, unlike the S_4 index, σ_φ captures the time series statistics that make a particular record hard to track. Unfortunately, it is difficult to model σ_φ^2 as a function of S_4, T, and p

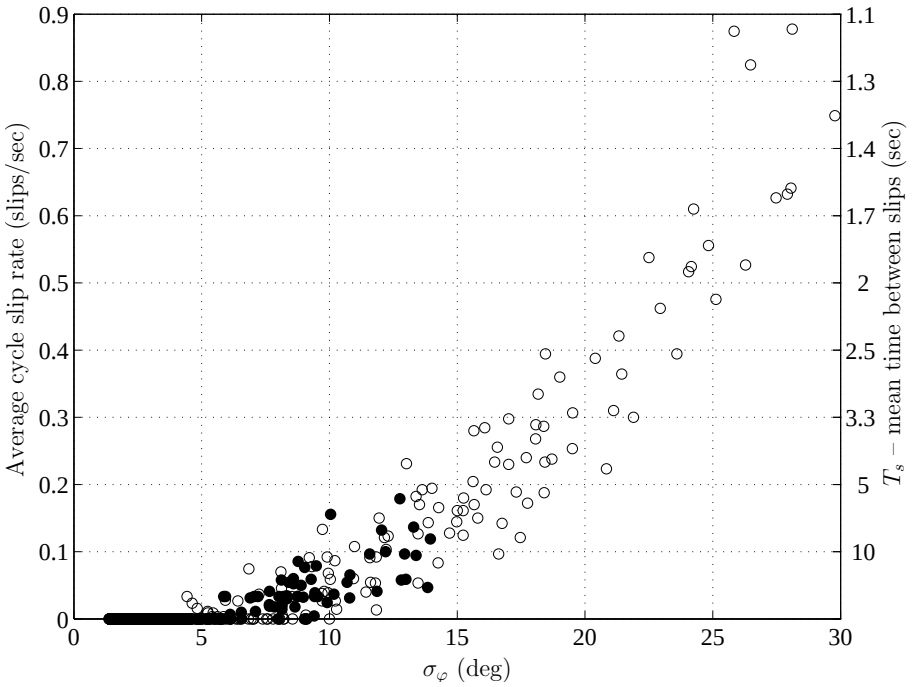

Figure 2.11: Average DD-AT PLL cycle slip rate over each 30-second test interval vs. σ_φ for the Wideband data at C/N_0 = 43 dB-Hz (open circles) and for the GPS L_1 data within 40 $\leq$ $C/N0$ $\leq$ 44 dB-Hz with mean C/N_0 = 43 dB-Hz (filled circles). The right axis expresses the cycle slip rate in terms of T_s.

without invoking the PLL linearity assumption, which, as mentioned in Section 2.5.1, is likely invalid for strong scintillation. Moreover, even if a good estimate of σ_φ^2 could be obtained, it is not clear how to connect σ_φ^2 and cycle slips in a way that explains the empirical relationship apparent in Fig. 2.11. The method adopted in [6], whereby σ_φ^2 is related to T_s on the basis of simulation results that assume Gaussian white measurement noise, leads to unreasonable predictions for T_s—especially for low values of σ_φ^2. Using the data underlying Fig. 2.11, one can show that, for the DD-AT PLL, Wideband and GPS data records that lead to $8 < \sigma_\varphi < 10$ deg yield mean T_s values of 29 and 27 seconds, respectively. By comparison, the DD-AT line in Fig. 2.7 indicates that for $\sigma_\varphi < 10.2$ deg, $T_s > 5$ hours. Hence, within this range of σ_φ, the method adopted in [6] overestimates T_s by over 600 times.

A more satisfactory modeling approach can be developed around the close connection between differentially-detected data bit errors and cycle slips. Recall from the discussion of Fig. 2.10. and Table 2.3 that, for both the Wideband and GPS data, the mean time T_e between DPSK-detected bit errors acts as a lower bound on the best-performing (DP-AT) PLL's value of T_s. Fig. 2.12, which plots the DP-AT PLL's average cycle slip rate for all 30-second scintillation library records vs. the DPSK-detected bit error rate over each record, shows that the relationship between slip rates and bit error rates is strongly correlated, and that both Wideband and GPS data obey the same trend. A straight-line fit to the data falls below the $T_s = T_e$ dashed line, indicating that T_e underbounds T_s. Thus, if one can predict T_e for a given time history of complex signal scintillation, then one has a useful lower bound for the DP-AT PLL's T_s.

The connection between T_e and T_s that is apparent in Fig. 2.12 was explained previously in terms of the differentially-detected bit estimates $d_{m,k}$. It can now be restated more generally as follows: the signal properties that tend to cause DPSK bit errors also tend to induce cycle slips in many PLL designs. By tying DPSK-detected bit errors to PLL cycle slips, one trades the difficult problem of cycle slip prediction for the more tractable problem of bit error prediction.

2.9.2 Binary DPSK Bit Error Probability in the Presence of Scintillation

The goal of this subsection is to derive an expression for the binary DPSK bit error probability for a scintillating communications channel. This expression will enable DPSK T_e to be estimated for a given time history $z(t)$ of complex signal scintillation. The formulation proposed here extends the closed-form solution for fast Ricean fading given in

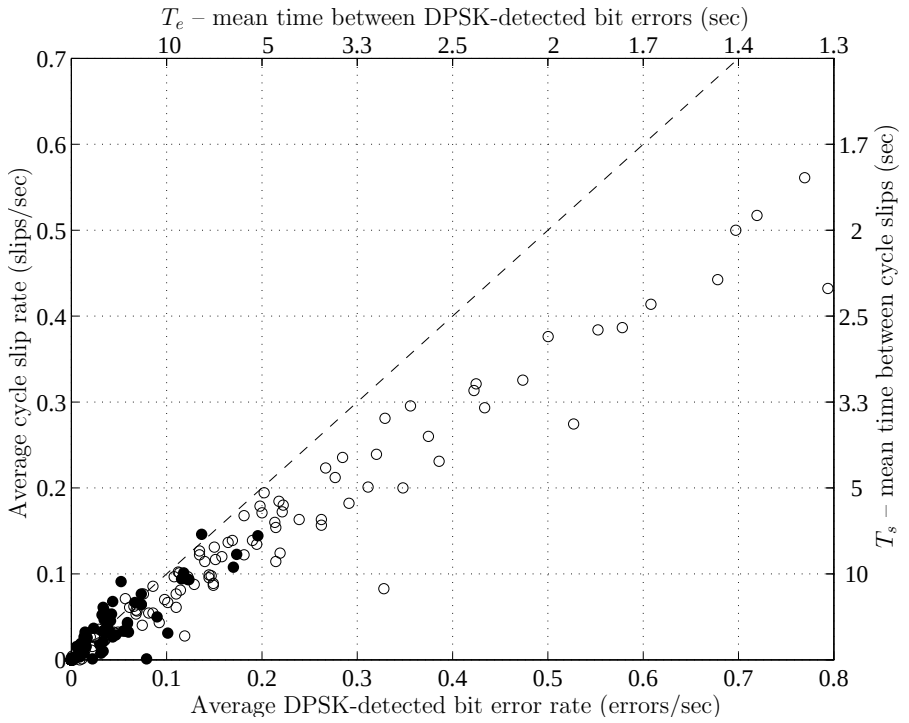

Figure 2.12: Average DP-AT PLL cycle slip rate vs. the average DPSK-detected bit error rate over each 30-second test interval for the Wideband data at $C/N_0 = 43$ dB-Hz (open circles) and for the GPS L_1 data within $40 \leq C/N0 \leq 44$ dB-Hz with mean $C/N_0 = 43$ dB-Hz (filled circles). The right and top axes express the cycle slip rate and bit error rate in terms of T_s and T_e, respectively. The dashed 45° line indicates the condition $T_s = T_e$.

[24, Sec. 8.2.5.2] to the specific case of complex signal scintillation with a 2nd-order Butterworth-type power spectrum.

Consider again the model for the complex baseband signal r_k given in Eq. (2.9). Assume that $T_a = T_b$ and that the phase estimate $\hat{\theta}(t)$ is generated by a low-bandwidth frequency tracking loop so that, like the carrier phase θ_c, it can be considered constant over adjacent bit intervals. For convenience, and without loss of generality, set $\theta_c = \hat{\theta}(t) = 0$ over the interval $[t_{k-2}, t_k)$. Then $r_k = z_k \sqrt{E_b} \exp(j\tilde{\theta}_k) + n_k$ is the complex baseband signal, where z_k now represents the average of $z(t)$ over the kth bit interval and E_b is the energy per bit. As before, the noise element n_k is zero-mean Gaussian with

$E[n_k^* n_j] = N_0 \delta_{k,j}$. Let the channel response function $z(t)$ be defined as $z(t) = \bar{z} + \xi(t)$, where $\bar{z}$ is the direct component, modeled as a complex constant, and $\xi(t)$ is the multipath component, modeled as a complex stationary zero-mean Gaussian random process with autocorrelation function $R_\xi(\tau) = \frac{1}{2}E[\xi^*(t)\xi(t+\tau)]$. The channel decorrelation time $\tau_0 > 0$ is defined as the value of τ for which $R_\xi(\tau)/R_\xi(0) = e^{-1}$. A narrow $R_\xi(\tau)$ (small τ_0) implies a scintillation channel that changes rapidly with time.

The binary DPSK decision variable is $u_k = \mathrm{Re}(r_k^* r_{k-1})$. In the absence of scintillation and noise, $u_k = 1$ when $\tilde{\theta}_k = \tilde{\theta}_{k-1}$, and $u_k = -1$ when $\tilde{\theta}_k = \tilde{\theta}_{k-1} + \pi$. Without loss of generality, suppose that $\tilde{\theta}_k = \tilde{\theta}_{k-1}$. Then $P_e = P(u_k < 0)$ is the binary DPSK bit error probability. Calculation of P_e requires the following statistics of z_k:

$$\sigma^2 \equiv \tfrac{1}{2}E[|z_k - \bar{z}|^2] = \frac{1}{T_b^2}\int_0^{T_b}\int_{t-T_b}^{t} R_\xi(\tau)\,d\tau\,dt \tag{2.16}$$

$$\rho\sigma^2 \equiv \tfrac{1}{2}E[(z_{k-1} - \bar{z})^*(z_k - \bar{z})] = \frac{1}{T_b^2}\int_0^{T_b}\int_{t-2T_b}^{t-T_b} R_\xi(\tau)\,d\tau\,dt \tag{2.17}$$

Assume that the channel response function $z(t)$ is normalized so that $E[|z(t)|^2] = 1$. Then for saturated (Rayleigh) fading where $\bar{z} = 0$, the quantity $2\sigma^2 \leq 1$ can be interpreted as the loss in signal power due to fluctuations in $z(t)$ over the integration interval. Likewise, $\rho \leq 1$ represents the degrading effect of bit-to-bit fluctuations in $z(t)$ on the DPSK decision variable u_k.

Under the assumption of Ricean fading, the magnitude of z_k, namely $\alpha_k = |z_k|$, has a Ricean probability distribution with mean-square value $\Omega \equiv E[\alpha_k^2] = 2\sigma^2(1 + K)$, where K is the Ricean K-parameter. Defining the average SNR per bit as $\bar{\gamma} \equiv \Omega E_b/N_0 = \Omega T_b C/N_0$, one has, together with ρ and K, all the quantities necessary to evaluate the closed-form expression for P_e given in [24, Sec. 8.2.5.2]:

$$P_e = \frac{1}{2}\left[\frac{1 + K + \bar{\gamma}(1-\rho)}{1 + K + \bar{\gamma}}\right]\exp\left(\frac{-K\bar{\gamma}}{1 + K + \bar{\gamma}}\right) \tag{2.18}$$

In practice, estimation of P_e can be approached in two different ways. The first approach assumes that the averages z_k are available. In this case, ρ can be estimated directly by evaluating the expectation operations in Eqs. (2.16) and (2.17) as time averages, then dividing Eq. (2.17) by Eq. (2.16). Likewise, Ω is estimated by evaluating $\langle |z_k|^2 \rangle$. Assuming that the underlying $z(t)$ is normalized ($E[|z(t)|^2] = 1$), then $\Omega < 1$ for any $S_4 > 0$. Next, the Ricean K parameter is estimated. Under the Ricean model, K is defined as the ratio of the direct component power to the multipath component power, i.e., $K \equiv |\bar{z}|^2/2\sigma^2$. In practice, invoking this definition to estimate K is problematic because low-frequency phase scintillation causes the instantaneous $\bar{z}$ to wander. Instead, it is best to estimate K based on its relationship with $m = 1/S_4^2$, given by

$$K = \frac{\sqrt{m^2 - m}}{m - \sqrt{m^2 - m}} \tag{2.19}$$

where S_4 is evaluated according to Eq. (3.4) with $I = \alpha_k^2$. If the measured S_4 exceeds unity, K is set to 0. Substituting K, ρ, and $\bar{\gamma} = \Omega E_b/N_0$ into Eq. (2.18) yields the desired P_e. Tests have shown that the values of P_e calculated according to this approach agree closely with the bit error probability averages observed in the scintillation testbed for a given interval of scintillation.

The second approach, which is more appropriate for theoretical work, calculates P_e based on the τ_0 and S_4 of a hypothetical scintillation time history $z(t)$. In this case, σ^2 and ρ are estimated indirectly via a model of $R_\xi(\tau)$. The model, which closely fits the autocorrelation functions of records in the scintillation library over a broad range of scintillation strength, corresponds to the power spectrum of a 2nd-order Butterworth filter [40]:

$$R_\xi(\tau) = \sigma_\xi^2 e^{(-\beta|\tau|/\tau_0)}[\cos(\beta\tau/\tau_0) + \sin(\beta|\tau|/\tau_0)] \tag{2.20}$$

with $\beta = 1.2396464$. Substituting this into Eqs. (2.16) and (2.17) leads to

$$\sigma^2 = \left(\sigma_\xi^2/q^2\right)[2q + f(q) - 1] \tag{2.21}$$

$$\rho\sigma^2 = \left(\sigma_\xi^2/2q^2\right)[f(2q) - 2f(q) + 1] \tag{2.22}$$

where $f(q) = \exp(-q)(\cos q - \sin q)$ and $q = \beta T_b/\tau_0$.

The approach for a hypothetical $z(t)$ proceeds as follows. As before, a K value corresponding to $z(t)$ is derived from S_4. Call this value K' to distinguish it from the K value associated with the averages z_k; the two are in general slightly different. Again assuming $E[|z(t)|^2] = 1$, K' is related to σ_ξ^2 and $\bar{z}$ by $2\sigma_\xi^2(1 + K') = 1$ and $\bar{z}^2 = 2K'\sigma_\xi^2$ (without loss of generality, $\bar{z}$ can be assumed to be real). Solving for σ_ξ^2 and substituting σ_ξ^2 and τ_0 into Eqs. (2.21) and (2.22) yields values for σ^2 and $\rho\sigma^2$. These, in turn, are used to estimate the K and Ω for the hypothetical averages z_k via $K = \bar{z}^2/2\sigma^2$ and $\Omega = \bar{z}^2 + 2\sigma^2$. Finally, the K, ρ, and $\bar{\gamma} = \Omega E_b/N_0$ corresponding to the z_k are used in Eq. (2.18) to solve for P_e. This approach has been tested using estimates of τ_0 obtained from the scintillation library's empirical $z(t)$ intervals. If the intervals are stationary and long enough to yield accurate estimates of τ_0, the approach generates a P_e that agrees closely with the bit error probability averages observed in the scintillation testbed over the same intervals.

Once P_e is obtained by any means, one calculates a useful lower bound for the achievable mean time between cycle slips T_s over the interval of scintillation considered by computing the mean time between DPSK-detected bit errors $T_e = T_b/P_e$. Thus, in response to the scintillation effects modeling challenge posed in the introduction to Section 2.9, one can offer the triad $\{S_4, \tau_0, C/N_0\}$ (or $\{K, \rho, \bar{\gamma}\}$, which contains equivalent information) as a scintillation channel characterization sufficient to approximately predict the cycle slip performance of a class of standard GPS PLLs. In this characterization, S_4 gives a measure of the scintillation intensity, τ_0 describes the speed of the

fluctuations, and C/N_0 defines the channel's nominal carrier-to-noise ratio.

2.9.3 Applicable Domain of the Scintillation Effects Model

It is necessary to outline the range of parameter values over which the proposed scintillation effects model is applicable. First note that the methods presented above for estimating T_e impose no restrictions on the range of τ_0 and C/N_0, and that the condition $S_4 \leq 1$ implied by $K \geq 0$ is not significantly restrictive because, aside from rare "focusing" behavior, S_4 takes on values near or below unity [9]. Thus, T_e can be estimated as described above for nearly all possible parameter values.

On the other hand, the model of T_e as a useful approximation for T_s is only valid within a limited range of τ_0, C/N_0, T_a and B_n values. For example, in the limit as nominal $C/N_0 \to \infty$, one can always reduce cycle slips by shortening T_a and widening B_n. In this extreme case, T_e and T_s are no longer usefully related. Of course, not all parameter values are of practical interest. For a terrestrial GPS receiver, values of nominal C/N_0 range from 38 to 55 dB-Hz. Within this range and in the presence of severe scintillation, widening B_n much beyond 10 Hz results in a steep increase in frequency unlock. Likewise, there exist practical limitations on the accumulation interval T_a: short T_a lead to increased squaring loss [cf. Eq. (2.5)], and long T_a tend to destabilize the tracking loop. Finally, realistic decorrelation times of L-band scintillation for a stationary receiver can be generally limited to $2 > \tau_0 > 0.2$ seconds. The following list summarizes practical ranges of τ_0, C/N_0, T_a and B_n for GPS carrier phase tracking in the presence of scintillation:

$$2 > \tau_0 > 0.2 \text{ sec} \qquad 38 \leq C/N_0 \leq 55 \text{ dB} - \text{Hz}$$

$$10 \leq T_a \leq 20 \text{ ms} \qquad 5 \leq B_n \leq 20 \text{ Hz}$$

Simulation tests have shown that the proposed model is applicable over this domain in the sense that on average $T_s/2 < T_e \leq T_s$.

2.10 Conclusions

Time histories of severe equatorial phase and amplitude scintillation from the Wideband Satellite experiment and from specially-processed GPS data have been compiled into a scintillation library. The data reveal a universal feature of strong equatorial scintillation: deep power fades ($>$ 15 dB) accompanied by abrupt, approximately half-cycle phase transitions. These "canonical fades" have been noted before by scintillation researchers, but they have not been expressly accounted for in existing models for scintillation effects on GPS receiver phase tracking loops.

A scintillation effects testbed that derives inputs from the scintillation library has been used to test several standard—and some exotic—phase tracking loop designs. Testbed results demonstrate that canonical fading causes the loops to skip cycles at a rate that is significantly faster than is predicted by existing scintillation effects models. Testbed results also show that the mean time between binary DPSK bit errors serves as a useful lower bound for the mean time between cycle slips experienced by a prototype PLL that uses differentially-detected data bit wipeoff. It has been argued that the prototype PLL is broadly representative of all PLLs in the sense that, without additional information (e.g., data bit aiding), other phase tracking schemes are unlikely to perform significantly better in severe scintillation than does the prototype PLL.

Inspired by the strong correlation between binary DPSK bit errors and cycle slips, a simple model for cycle slip prediction has been developed that can assess the severity of a given scintillation time history. The model, which reasonably approximates the rate of

cycle slipping observed in the testbed results, is based on the scintillation index S_4, the complex scintillation signal decorrelation time τ_0, and the nominal carrier-to-noise ratio C/N_0.

2.11 Appendix

This appendix describes the preliminary processing used to prepare the GPS L_1 data for inclusion in the scintillation library. In an initial processing pass, a GPS L_1 C/A-code software receiver operates on raw 5.7-MHz data samples that were recorded during a scintillation event. The software receiver produces navigation data bit, phase, and amplitude estimates for all GPS signals present in the data. Its PLL is a B_n = 10-Hz, 3rd-order loop with an arctangent discriminator and a 100-Hz pre-detection bandwidth; its loop filter is based on the controlled-root formulation [34]. If navigation bit parity failures are detected in the output data, then the raw data samples are reprocessed, this time with the bi-phase navigation data bits wiped off. Bit wipeoff requires reconstruction of an entire 12.5-minute navigation data superframe, which proceeds by replacing corrupted sections with their error-free counterparts. Such a reconstruction is possible because almost all the navigation data bits are either repeated across GPS links or are repeated in time during a 2-hour window. Exceptions to this rule occur infrequently and are limited to the 14-bit TLM message of the TLM word. If scintillation-induced bit errors occur here, they can often be corrected by hand. Since only certain patterns of four-bit errors are undetectable under the GPS parity check code, a reconstructed superframe is considered intact, for purposes of data bit wipeoff, if it passes the parity check.

This process of checking for parity errors and, if detected, reprocessing with the data

bits wiped off ensures that, like the Wideband data, no fractional cycle slips remain in the GPS software receiver's output phase time history. However, other effects remain in the phase data, namely, phase variations due to (1) receiver clock instability, (2) carrier Doppler due to line-of-sight motion, (3) PLL dynamics, and (4) receiver noise. An attempt is made to remove each of these effects as follows.

Receiver clock instability: The frequency reference of the digital storage receiver on which the raw 5.7-MHz GPS data were recorded is a temperature-compensated crystal oscillator (TCXO). It is known that the power spectrum of phase variations due to the TCXO's frequency instability significantly overlaps the power spectrum of phase scintillation [41]. Fortunately, the two effects can be separated in post-processing because, whereas phase scintillation is different from one GPS link to the next, receiver clock noise is common to all links. Removal of clock noise proceeds as follows: Over each interval of recorded GPS data, a relatively strong, minimally scintillating GPS link is chosen as the reference signal. The reference signal's phase time history is subtracted from the time history of a scintillating signal of interest. The resulting phase time history is free of phase variations due to receiver clock instability. Naturally, an unavoidable consequence of this approach is an approximate doubling of the spectrally flat measurement noise content in the differenced phase data.

Motion-induced carrier Doppler: Even after removal of receiver clock effects, a large low-frequency component due to the difference in motion-induced carrier Doppler shift between the scintillating and reference signals remains in the differenced phase time history. This component is easily eliminated by subtracting a low-order curve fit from the differenced phase time history.

PLL dynamics: The scintillating signal's true phase variations are filtered through the transfer function of the software receiver's PLL. Such filtering band limits ($\sim$ 10 Hz) and

adds second-order dynamics (i.e., overshoot and oscillation) to the desired scintillation time history. To eliminate these effects, the instantaneous phase error $\phi(t_k)$, as measured using the known navigation bits and the four-quadrant arctangent function, is added to the PLL's phase estimate $\hat{\theta}(t_k)$. The resulting signal is band limited only by the software receiver's 100-Hz pre-detection bandwidth.

Receiver noise: Widening the bandwidth of the software receiver's phase estimate as described above increases its broadband measurement noise component. Ideally, one would like to separate measurement noise from genuine scintillation-induced phase variations, but there is no way to distinguish the two in practice. The best one can do is identify a frequency beyond which phase scintillation has a negligible effect on phase tracking; the phase data is then low-pass filtered at this cutoff frequency. Unfortunately, the scintillating phase's power-law spectrum does not present any obvious candidates for a cutoff frequency. Upon examining the active GPS spectra in Fig. 2.4, one might be tempted to choose the frequency at which the phase spectrum breaks at the noise floor ($\sim$ 10 Hz) as the low-pass cutoff, but testbed runs using data with 10-Hz and 20-Hz cutoffs showed that, for the same effective C/N_0, the 20-Hz data were significantly more challenging to track. Also, at 20-Hz, the canonical-fade phase variations in the GPS data resembled much more closely the sharp phase changes in the low-noise Wideband data. Therefore, a conservative 20-Hz cutoff has been chosen. Both phase and amplitude data are 6th-order low-pass Butterworth filtered at this cutoff; hence, time shifts in the filtered amplitude and phase data are equal. For the amplitude data, filtering is done separately for the real and imaginary components of the baseband complex signal. The magnitude of the filtered result becomes the scintillating amplitude time history.

For use in the scintillation testbed, a measure of the noise component remaining in the amplitude and phase time histories is required so that approximate nominal C/N_0

values can be assigned to tests with the data. A scheme for estimating the intrinsic C/N_0 value of each GPS scintillation record has been developed based on (1) the known noise floor of the digital storage receiver's RF front-end, (2) the scintillation record's nominal amplitude, estimated as $\bar{A} = \sqrt{\Omega}$, where Ω is defined in Section 2.4.2, and (3) a model for how broadband noise is added in the phase differencing process and subtracted in the filtering process. The resulting C/N_0 values assigned to each GPS record ranged from 38 to 44 dB-Hz.

2.12 Acknowledgments

The authors give special thanks to J. Secan of NorthWest Research Associates for providing raw Wideband experiment data. Thanks also to A. Kumar from Cornell's department of Theoretical and Applied Mechanics for useful discussions on trapping regions in discrete-time nonlinear PLL dynamics.

Chapter 3

Simulating Ionosphere-Induced Scintillation for Testing GPS Receiver Phase Tracking Loops

T. E. Humphreys, M. L. Psiaki, and P. M. Kintner, Jr., "Simulating Ionosphere-Induced Scintillation for Testing GPS Receiver Phase Tracking Loops," to be submitted to *IEEE Transactions on Aerospace and Electronic Systems*.

3.1 Abstract

A simple model is proposed for simulating equatorial transionospheric radio wave scintillation. The model can be used to test Global Positioning System phase tracking loops for scintillation robustness because it captures the scintillation properties that affect such loops. In the model, scintillation amplitude is assumed to follow a Rice distribution, and the spectrum of the rapidly-varying component of complex scintillation is assumed to follow that of a low-pass 2nd-order Butterworth filter. These assumptions are justified, and the model validated, by comparison with phase-screen-generated and empirical scintillation data in realistic tracking loop tests. The model can be mechanized as a scintillation simulator that expects only two input parameters: the scintillation index S_4 and the decorrelation time τ_0.

3.2 Introduction

Increased dependence on the Global Positioning System (GPS) and other satellite navigation systems makes users vulnerable to signal loss or degradation caused by ionospheric effects. Radio wave scintillation, the temporal fluctuation in phase and intensity caused by electron density irregularities along the propagation path, stresses a GPS receiver's carrier tracking loop, and, as severity increases, can lead to navigation bit errors, cycle slipping, and complete loss of carrier lock [1–8].

In anticipation of the 2011 solar maximum, when scintillation effects will be more severe, there is great interest in testing civilian and military GPS receivers for scintillation robustness. Such testing entails subjecting a receiver's tracking loops to realistic phase and amplitude scintillation. This can be done by passing scintillation time histories through a software model of the tracking loops [1, 3, 7, 16, 20]; or by forcing phase and amplitude variations in the output of a GPS signal simulator [8, 21]; or, in the ultimate confrontation with reality, by field testing receivers in a region prone to strong scintillation [4]. The first two of these testing strategies can give misleading results if the scintillation time histories are not realistic. For example, in field testing on Ascension Island during the 2000 solar maximum, researchers noted receiver performance degradations much worse than those predicted by simulations conducted prior to the campaign [4, 8].

In a previous paper [1], the current authors propose a receiver testing strategy that is based on drawing scintillation time histories from a large library of empirical equatorial scintillation data. The scintillation library includes severe complex signal scintillation from the Wideband Satellite experiment [22] and from specially-processed GPS data. The data reveal a universal feature of strong equatorial scintillation: deep power fades

(> 15 dB) accompanied by abrupt, approximately half-cycle phase transitions. These "canonical fades" are shown in [1] to be the primary cause of loss of carrier lock in GPS phase tracking loops.

Although a receiver testing strategy based on empirical data is attractive for its realism, it nonetheless has several drawbacks: (1) A test engineer is only at liberty to adjust the scintillation behavior insofar as this behavior is represented in the recorded data; (2) thermal noise in the receiver that was originally used to record the data can leave high-frequency variations that make it difficult to precisely specify the carrier-to-noise ratio of a given test (this is the case in [1] for the scintillation library's GPS data); and (3) the empirical scintillation data is only stationary over short time intervals, making impossible extended testing under consistent scintillation statistics.

These limitations can be overcome by generating synthetic scintillation via computer simulation. Techniques for synthesizing scintillation include first-principles physics-based ionospheric models [42]; phase screen models [43–45]; and statistical models [7, 8, 16]. For testing carrier tracking loops, one seeks the simplest scintillation model—in terms of number of parameters and computational expense—that faithfully retains the scintillation properties that are relevant to carrier tracking. This goal favors statistical models over the computationally expensive and parameter-laden first-principles and phase-screen models.

Because statistical models are abstractions of the physics that inspires them, extra effort must be made to ensure that their outputs are realistic. As noted in [1], the methods used in [7]—and likely in [8] and [16], though details are not provided—shape the phase and amplitude spectra independently. This practice tends to produce scintillation time histories that are artificially easy to track because they do not manifest realistic canonical fades. As demonstrated in the present paper, the key to synthesizing realistic scintillation

is to focus on properly shaping the spectrum of the entire complex scintillation signal, not the amplitude and phase data taken independently. The proper spectral shape of the complex scintillation signal and the general structure of the scintillation model proposed in this paper are inspired by the model of equatorial scintillation effects on GPS phase tracking loops developed in [1]. The result is a simple and computationally efficient technique for simulating realistic equatorial scintillation. (Both [1] and the current paper focus on equatorial scintillation because it is particularly difficult to track.)

The next section develops the scintillation model. The development is aided by analyses of empirical scintillation amplitude distributions and power spectra. Thereafter, in Section 3.4, the model is validated by comparing its effect on phase tracking loops with the effects of phase-screen-generated and empirical scintillation. The conclusions follow in Section 3.5.

3.3 Scintillation Model

The scintillation model proposed here is premised on the notion, advanced in [1], that the scintillation properties that tend to induce cycle slips in many GPS phase tracking loop designs also tend to cause bit errors in differential detection of the 50 bps binary GPS navigation message that is phase modulated onto the L_1 carrier signal. In other words, if the noise and the scintillation-induced phase change between adjacent data bits (each 20 ms long) is so severe that one cannot decide correctly whether a bit sign change occurred, then a cycle slip is also likely. More precisely, it was shown in [1] that, over a broad range of operating conditions, the mean time between differentially-detected bit errors T_e acts as a lower bound to the mean time between cycle slips T_s for phase tracking loops with good scintillation performance in the sense that on average

$T_s/2 < T_e \leq T_s$. By accepting T_e as a rough proxy for T_s, one trades the difficult problem of cycle slip prediction for the more tractable problem of bit error prediction.

As outlined in [1], estimating T_e for a given interval of complex signal scintillation requires a model of the complex channel response function $z(t)$. One can think of $z(t)$ as the scintillation time history; its phase and magnitude are the phase and magnitude changes imposed on the GPS carrier signal by the scintillating communications channel.

The conjecture that underpins the proposed model can be summarized as follows: The close connection between T_e and T_s implies that, if a model for $z(t)$ accurately predicts T_e, then the same model can be used to synthesize scintillation because it necessarily captures the scintillation properties that cause cycle slipping, an important scintillation effect on GPS phase tracking loops. It will be shown in Section 3.4 that this conjecture is borne out by experiment.

Assume that the $z(t)$ is normalized so that $\Omega \equiv E[\alpha^2(t)] = 1$, where $\alpha(t) = |z(t)|$. Thus, when no scintillation is present, $z(t) = 1$. An estimate of T_e depends on two properties of $z(t)$, namely, its amplitude distribution $p(\alpha)$ and a measure of the rapidity with which $z(t)$ wanders about the complex plane [1]. This characterization becomes intuitive when one considers that the abrupt phase shifts in $z(t)$ that cause false sign changes between adjacent data bits tend to occur when $z(t)$ transits rapidly through a small neighborhood of the origin. Thus, if one knows the probability of being near the origin [given by $p(\alpha)$] and the speed of $z(t)$, one can predict T_e.

In deriving T_e, $z(t)$ is typically assumed to have the form

$$z(t) = \bar{z} + \xi(t) \tag{3.1}$$

where $\bar{z}$ is the direct component, modeled as a complex constant, and $\xi(t)$ is the time-varying multipath component (see, for example, [40] where the form is explicit and

[38] and [24, Sec. 8.2.5.2] where it is implicit). The multipath component $\xi(t)$, also referred to as the fading process, has an autocorrelation function defined by $R_\xi(\tau) = \frac{1}{2}E[\xi^*(t)\xi(t+\tau)]$. The channel decorrelation time $\tau_0 > 0$ is defined as the value of τ for which $R_\xi(\tau)/R_\xi(0) = e^{-1}$. A narrow $R_\xi(\tau)$ (small τ_0) implies a scintillation channel that changes rapidly with time. Hence, the shape of $R_\xi(\tau)$—most importantly, the width of its main peak—defines the measure of $z(t)$ rapidity mentioned above.

To further develop the scintillation model, the form of $p(\alpha)$ and of $R_\xi(\tau)$ must be specified. This is the subject of the next two subsections.

3.3.1 Amplitude Distribution

There does not exist at present a rigorous theory that predicts the probability distribution of $z(t)$. Only in certain limiting cases have sufficient moment calculations been carried out to completely characterize a first-order distribution [9, 18]. It can be shown, for example, that when scintillation severity enters the so-called saturation regime, the amplitude distribution $p(\alpha)$ approaches a Rayleigh distribution. In general, however, only numerical or empirical approaches have proven tractable for defining the distribution of $z(t)$.

In [18], several candidate distributions for $z(t)$ were evaluated against scintillation data from the Wideband Satellite experiment. The results of hypothesis test calculations indicated that the Nakagami-m distribution gives the best fit to the empirical intensity (and amplitude) distributions. However, the analysis is not definitive for severe equatorial scintillation at frequencies near or above UHF because its data sets are short (20 seconds) and few (20 sets at UHF and 9 sets at L-band). Furthermore, the exposition in [18] does not make clear how time correlation in the empirical $z(t)$ is handled in the

hypothesis testing analysis.

Drawing on the extensive collection of scintillation data in the empirical scintillation library (introduced in [1]), a new hypothesis testing analysis has been carried out to determine an appropriate model for the amplitude distribution $p(\alpha)$. The new analysis focuses on strong equatorial scintillation at UHF and L-band frequencies, and limits the candidate models to the popular Nakagami-m and Nakagami-n (Rice) distributions, given respectively by [24, Ch. 2]

$$p_m(\alpha) = \frac{2m^m \alpha^{2m-1}}{\Omega^m \Gamma(m)} \, e^{-m\alpha^2/\Omega} \tag{3.2}$$

$$p_n(\alpha) = \frac{2\alpha(1+K)}{\Omega} I_0\left(2\alpha\sqrt{\frac{K+K^2}{\Omega}}\right) e^{-K-\alpha^2(1+K)/\Omega} \tag{3.3}$$

where $\alpha \geq 0$, $\Gamma(\cdot)$ is the gamma function, K is the Rician parameter, and $m = 1/S_4^2$. The quantity S_4 is the standard scintillation index defined by

$$S_4^2 = \frac{\langle I^2 \rangle - \langle I \rangle^2}{\langle I \rangle^2} \tag{3.4}$$

in which $I = \alpha^2$ is signal intensity and $\langle \cdot \rangle$ denotes time average. The Rician K parameter is related to m (and thereby to S_4) by

$$K = \frac{\sqrt{m^2 - m}}{m - \sqrt{m^2 - m}} \tag{3.5}$$

At $S_4 = m = 1$, the Nakagami-m and Rice distributions both converge to the Rayleigh distribution. For $S_4 > 1$, the Nakagami-m distribution is defined whereas the Rice distribution is not. This limitation of the Rice distribution is not restrictive in practice because, aside from rare "focusing" behavior, S_4 takes on values near or below unity [9]. At values of S_4 less than unity, the Nakagami-m and Rice distributions are similar, as illustrated in Fig. 3.1, where the two distributions are shown to agree closely

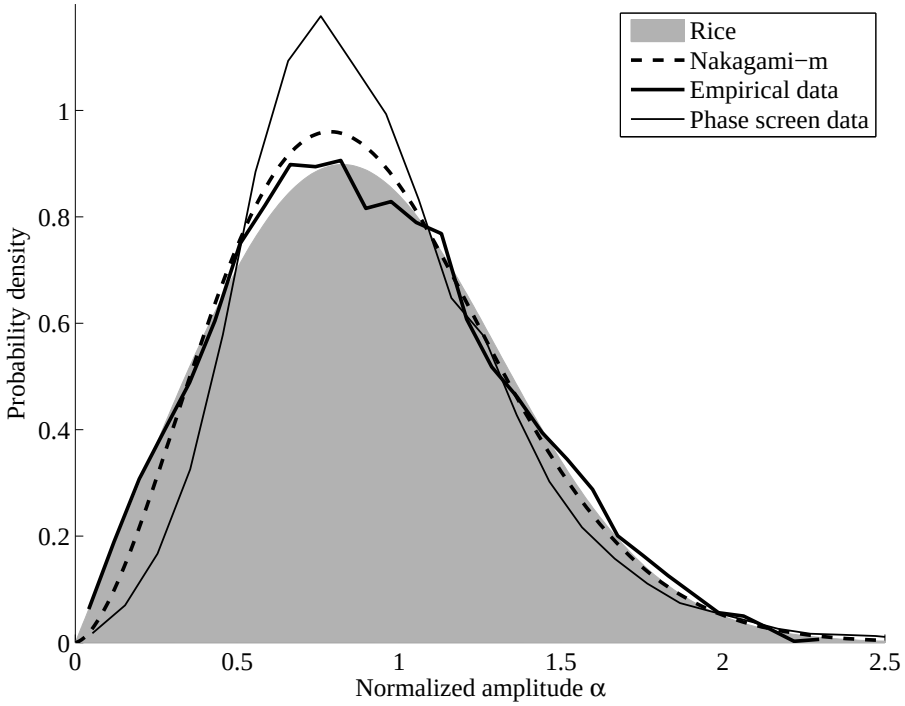

Figure 3.1: Amplitude distribution of empirical scintillation data from the scintillation library (thick solid line) compared with the Nakagami-m and Rice distributions and with the amplitude distribution of scintillation data generated by a phase screen model. For all distributions $S_4 = 0.87$.

with with a histogram (thick solid line) of representative Wideband UHF data from the scintillation library.

Also shown in Fig. 3.1 is the amplitude distribution of scintillation data that were generated by a modified version of the phase screen model presented in [43]. The modified version accommodates the development of amplitude fluctuations within the irregularity slab by replacing the single phase screen of [43] with a set of two phase screens separated by 100 km, with the uppermost screen located 350 km above the observation plane. The phase variations across each screen are Gaussian and have a power-law-type spatial power spectrum with an outer scale of 7 km and a spectral index of $\nu = -3.4$. A wavelength corresponding to the GPS L_1 frequency (1575.42 MHz) is assumed.

The phase screen scintillation model has been validated in several studies and has gained wide acceptance among theoreticians and experimentalists [25]. In this paper, it is exploited as an aid in studying the fading process spectrum (next subsection) and in validating the proposed scintillation model (Section 3.4). However, for intermediate values of the perturbation strength of the screen (defined by the parameter C_s in [43]), that is, perturbation strength values which lead to $1 > S_4 > 0.6$, the phase screen model tends to produce scintillation time histories whose amplitude distributions depart markedly from empirical amplitude distributions, as illustrated in Fig. 3.1. For perturbation strength values well into the saturation regime ($S_4 \approx 1$) or in the weak scintillation regime ($S_4 < 0.4$), the phase-screen-generated and empirical distributions agree closely. This behavior reinforces the preference for a statistical scintillation model over the phase screen model for testing carrier tracking loops.

To evaluate the goodness-of-fit of the Nakagami-m and Rice distributions, average chi-square values were computed for 79 sets of Wideband UHF data and for 33 sets of GPS L_1 data drawn from the scintillation library. The data sets, whose lengths range from 50 to 300 seconds, correspond to relatively stationary intervals of strong scintillation ($S_4 > 0.6$). Intervals were chosen by inspection from the library records. Only a subset of the data samples from each interval was used in the chi-square calculations. Each sample in the subset is separated in time from adjacent samples by twice the decorrelation time τ_0 of the full interval. This ensures that data samples are independent from each other, as assumed by the chi-square technique. The length of each data set was chosen such that each chi-square test operated on approximately 100 samples. Thus, for slowly-varying scintillation (long τ_0), longer data sets were required to produce 100 independent samples. Partitioning of the samples led to 8 chi-square degrees of freedom (DOF) for the Wideband UHF data and 7 for the GPS L_1 data (recall that the number of chi-square DOF is equal to the number of bins used to partition the data in the cal-

culation of the chi-square statistic). In the results of the chi-square tests, presented in Table 3.1, the chi-square values are near the respective chi-square DOF for both the Nakagami-m and Rice distributions. This indicates that both the Nakagami-m and the Rice distributions provide a good fit to the data, though the Rice distribution retains a slight advantage for both data sources.

Table 3.1: Chi-square Values for Fits to Nakagami-m and Rice Distributions

Data Source	**Sets, DOF**	**Nakagami-m**	**Rice**
Wideband UHF	79, 8	11.8 ± 8.8	9.0 ± 4.3
GPS L_1	33, 7	8.42 ± 5.9	7.7 ± 5.7

While the goodness-of-fit results in Table 3.1 justify either a Nakagami-m or a Rice model for the amplitude distribution, the Rice model is easier to implement in practice: one has only to assume that the fading process $\xi(t)$ in Eq. (3.1) is Gaussian, and a Rice distribution naturally results for the amplitude $\alpha(t) = |z(t)|$. Hence, in the proposed model, $\xi(t)$ is assumed to be a complex, zero-mean, stationary, Gaussian random processes with autocorrelation function $R_\xi(\tau)$. The Rician K parameter relates the magnitude of $\bar{z}$ to $\sigma_\xi^2 = R_\xi(0)$:

$$K = \frac{|\bar{z}|^2}{2\sigma_\xi^2} \tag{3.6}$$

3.3.2 Autocorrelation Function

To complete the proposed scintillation model, the form of the autocorrelation function $R_\xi(\tau)$ must be specified. Equivalently, one may specify $S_\xi(f)$, the power spectrum of the complex fading process $\xi(t)$, which is related to $R_\xi(\tau)$ by the Fourier transform. One would hope to bring the vast theory developed over many years in the scintillation literature to bear on the problem of modeling $S_\xi(f)$. But whereas the scintillation model

in Eq. (3.1) is perfectly adequate for purposes of channel and receiver effects modeling, it is not valid in general for scintillation because it fails to capture the naturally-occurring low-frequency wander in the mean $\bar{z}$. Thus, the scintillation literature generally treats the complex scintillation signal $z(t)$ as a whole. (For example, the theoretical power spectra of the scintillation amplitude $\alpha(t) = |z(t)|$ and intensity $I(t) = \alpha^2(t)$ are, for weak scintillation, well understood [9].) Of course, for strong scintillation, the direct component $\bar{z}$ is negligible and $\xi(t)$ becomes equivalent to $z(t)$. Unfortunately, in the case of strong scintillation the scintillation theory is on unsure footing [9]. Therefore, it appears most practical to adopt an experimental approach to specifying $S_\xi(f)$.

The following procedure has been used to determine the structure of $S_\xi(f)$ based on empirical and phase-screen-generated scintillation time histories. The phase of a scintillation time history $z(t)$ is high-pass filtered to remove its low-frequency components. A zero-phase filter is employed to preserve alignment of the phase and amplitude data. For convenience, let $z_f(t)$ represent the filtered version of $z(t)$. The filter cutoff frequency is adjusted so that the mean of $z_f(t)$, denoted $\bar{z}_f$, is near the value of $\bar{z}$ predicted by the Rician K parameter, itself derived from the measured S_4 [cf. Eqs. (3.4)-(3.6)]. Further small adjustments to the filter cutoff frequency are made to roughly equalize the variances of the quadrature components of $\xi_f(t) = z_f(t) - \bar{z}_f$. Typical final cutoff frequencies range from 0.05 to 0.4 Hz. It should be emphasized that only the phase of $z(t)$ is altered by such filtering; the amplitude time history—and the amplitude and intensity spectra—remain unchanged. Furthermore, the filtered and the original scintillation time histories are equivalent from the perspective of a carrier tracking loop. This is because the naturally-occurring variations in the mean $\bar{z}$ are much slower than ordinary tracking loop response times. This has been demonstrated by passing both $z(t)$ and $z_f(t)$ through the software tracking loops introduced in [1] and noting that the loops perform equivalently (in terms of cycle slips and phase error variance) when operating on either time

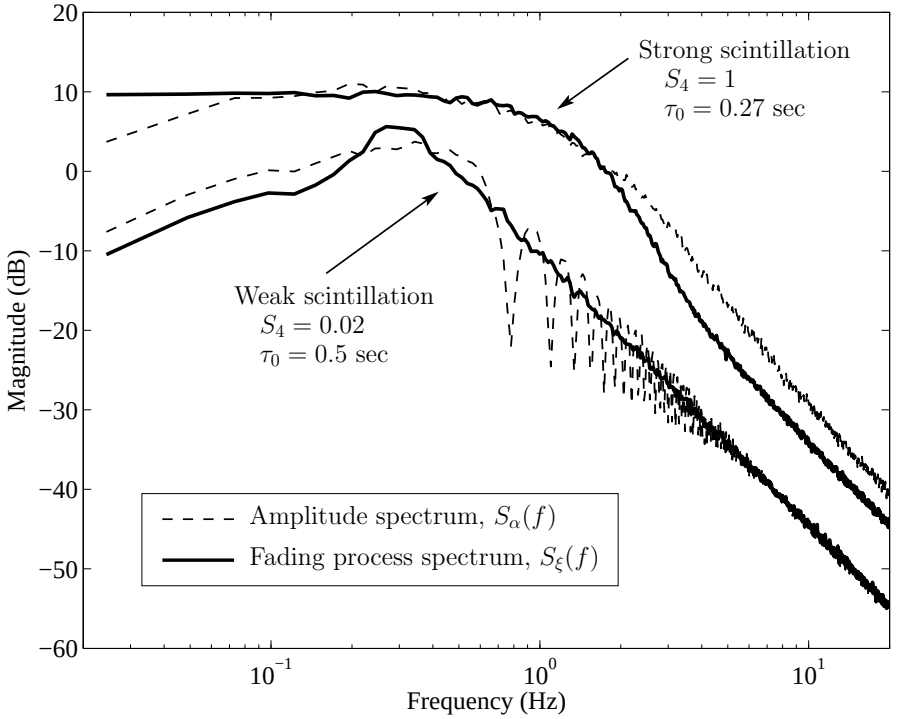

Figure 3.2: Comparison of amplitude and fading process power spectra in the weak and strong scintillation regimes. All spectra are based on phase-screen-generated scintillation data. For visual clarity, the strong and weak scintillation spectra have been offset from each other by 10 dB.

history.

Using the above filtering technique, empirical and phase-screen-generated scintillation time histories can be made to conform to the model in Eq. (3.1). The form of $S_\xi(f)$ then becomes apparent in the power spectra of the filtered time histories. Fig. 3.2 plots $S_\xi(f)$ for scintillation generated by the phase screen model described previously. Cases of weak and strong scintillation are considered. For the weak scintillation case, a single phase screen with a low perturbation strength ($C_s = 10^{19}$ in the parameterization of [43]) was used. For the strong scintillation case, two phase screens, each with a high perturbation strength ($C_s = 10^{22}$), were used. The phase screen parameters were otherwise equivalent for the two cases.

For comparison with $S_\xi(f)$, Fig. 3.2 also plots the amplitude spectrum $S_\alpha(f)$ derived from the same data for both the weak and strong cases. The weak-scintillation amplitude spectrum agrees closely with the model from weak scintillation theory (given, for example, in [46]). At low frequencies, $S_\alpha(f)$ is relatively flat up to a break point known as the Fresnel frequency, f_F. The value of f_F increases with decreasing wavelength of the propagating radio wave, with decreasing height of the ionospheric irregularities, and with increasing velocity of the radio line-of-sight ionospheric pierce point relative to the irregularities. After breaking at f_F, the weak-scintillation amplitude spectrum manifests "Fresnel oscillations" and finally rolls off toward a high frequency asymptote f^ν, where ν is the spectral index of the phase screen and is related to the spectral index p of the 3-dimensional irregularity medium by $\nu = 1 - p$. Empirical values for p are approximately 4.4 [9], which explains the choice of $\nu = -3.4$ for the phase screen spectral index. For strong scintillation (upper plots in Fig. 3.2), the amplitude spectrum also approaches f^ν at high frequencies, but the spectrum is wider and the Fresnel frequency is less distinct. This "spectral broadening" of $S_\alpha(f)$ with increasing scintillation strength is well documented in the literature [46].

One notes from Fig. 3.2 that, although $S_\xi(f)$ manifests no Fresnel oscillations (in either the weak or strong case), and, for strong scintillation, initially rolls off more steeply than $S_\alpha(f)$, it nonetheless generally conforms to the shape of $S_\alpha(f)$. This is consistent with the empirical findings presented in [47], where it was shown that during strong scintillation [for which $z(t) \approx \xi(t)$], amplitude fluctuations dominate the spectral shape of the quadrature components of $z(t)$.

The plots in Fig. 3.2 suggest that $S_\xi(f)$ can be modeled approximately as the spectrum of a low-pass filter with a 2nd-order rolloff. For simplicity, let $S_\xi(f)$ be modeled

as the spectrum of a 2nd-order Butterworth filter. In this case, $R_\xi(\tau)$ is given by [40]

$$R_\xi(\tau) = \sigma_\xi^2 e^{(-\beta|\tau|/\tau_0)}[\cos(\beta\tau/\tau_0) + \sin(\beta|\tau|/\tau_0)] \tag{3.7}$$

where $\beta = 1.2396464$. Such a model falls within the two limiting forms for scintillation spectra—the so-called Gaussian and f^{-4} spectra—given in [33].

Panel (a) of Fig. 3.3 shows a representative empirical spectrum $S_\xi(f)$ that is based on data from the scintillation library ($S_4 = 0.87$), and compares this to the proposed 2nd-order Butterworth model and to the Gaussian and f^{-4} models. The corresponding normalized autocorrelation functions $R_\xi(\tau)/R_\xi(0)$ are given in panel (b). All models have been matched to the decorrelation time τ_0 of the empirical data.

The inset in panel (b) gives an expanded view of the first 40 ms of the autocorrelation plots. This critical window, equal in length to two GPS data bits, determines the degrading effect of bit-to-bit fluctuations in $z(t)$ on differential bit detection (cf. Eqs. (16) and (17) in [1]). Together with the amplitude distribution $p(\alpha)$, the shape of $R_\xi(\tau)$ over the first 40 ms completely specifies the probability of error for GPS differential binary bit detection. Hence, it is this 40-ms window that must be accurately captured in the proposed model. In the frequency domain, this amounts to accurately modeling the shape of $S_\xi(f)$ in the neighborhood of the Fresnel frequency.

It can be shown that with a proper choice of τ_0, any one of the models in Fig. 3.3 can be made to closely match the first 40 ms of the autocorrelation function of a given Wideband data record in the scintillation library. (The GPS data, which contain some high frequency noise that slightly distorts $R_\xi(\tau)$, were excluded from these tests.) On average, however, the 2nd-order Butterworth filter provides the best fit; moreover, it is the easiest to implement. This justifies its adoption in the proposed scintillation model.

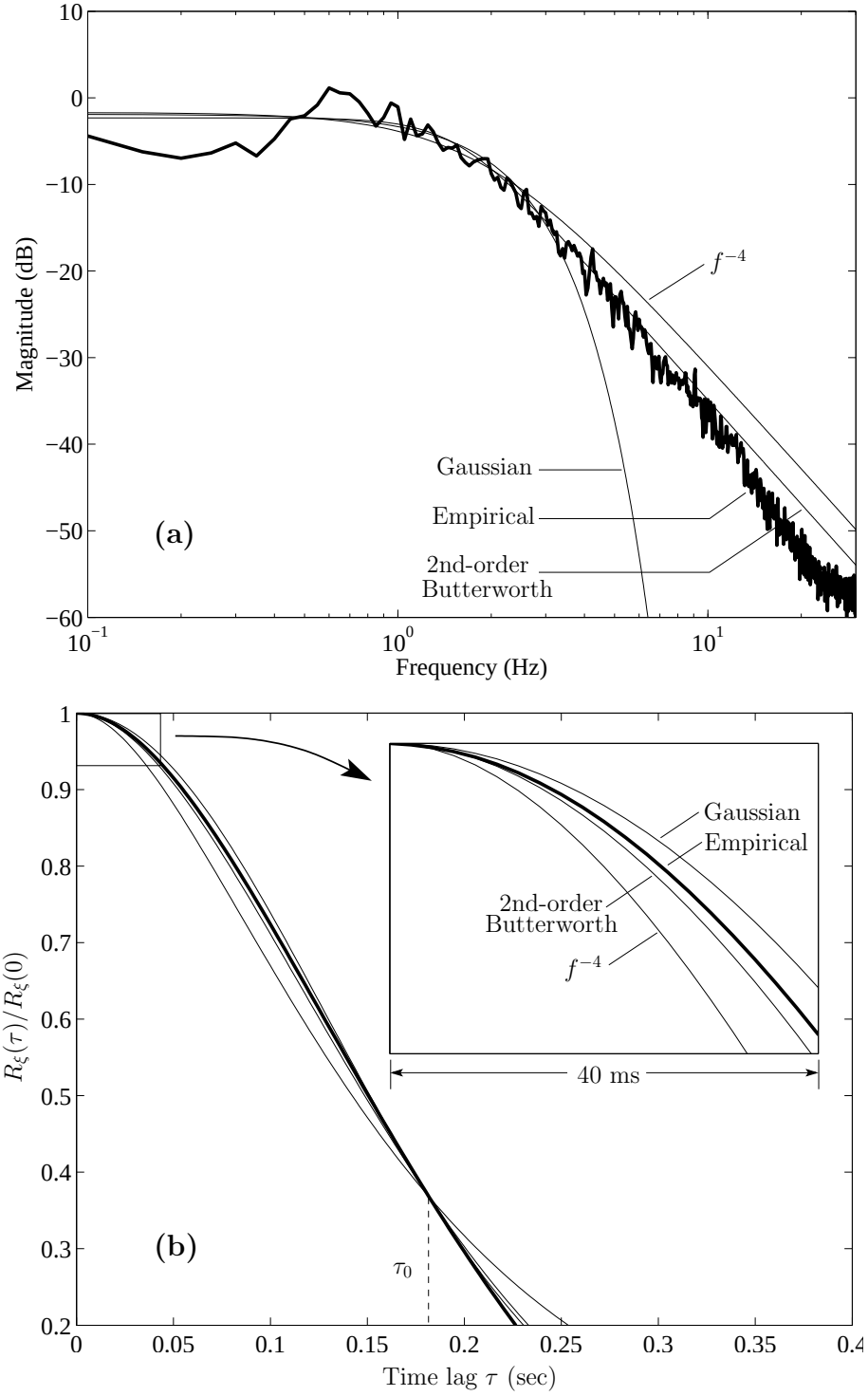

Figure 3.3: (a) Empirical fading process spectrum (thick line) compared with the f^{-4}, Gaussian, and 2nd-order Butterworth spectral models. (b) Auto-correlation functions corresponding to the spectra in panel (a).

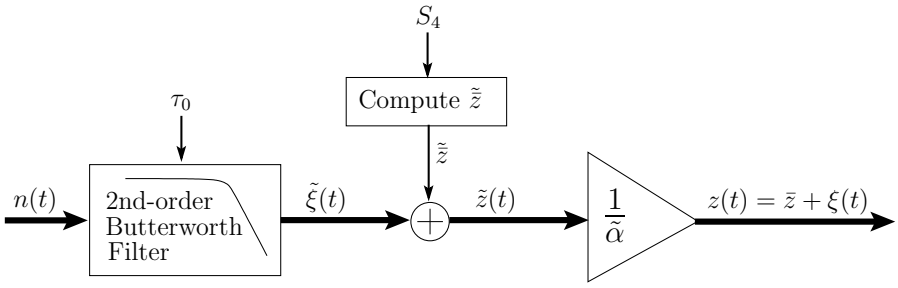

Figure 3.4: Block diagram illustrating a straightforward mechanization of the proposed scintillation model. Thick lines denote complex signal routing.

3.3.3 Scintillation Simulator Mechanization

The proposed scintillation model can be mechanized as shown in Fig. 3.4. In this form, the model becomes a scintillation simulator capable of generating realistic scintillation time histories $z(t)$. Zero-mean complex white Gaussian noise $n(t)$ is passed through a 2nd-order Butterworth filter with amplitude response function

$$|H(f)| = \frac{1}{\sqrt{1 + \left(\frac{f}{B_d}\right)^4}} \tag{3.8}$$

where $B_d = \beta/(\sqrt{2}\pi\tau_0)$ is the filter bandwidth, with β as in Eq. (3.7) and τ_0 being the desired decorrelation time. Let the resulting filtered noise process be denoted $\tilde{\xi}(t)$, with variance $\sigma^2_{\tilde{\xi}}$. The value of the direct component $\tilde{\bar{z}}$ is computed as

$$\tilde{\bar{z}} = \sqrt{2\sigma^2_{\tilde{\xi}} K} \tag{3.9}$$

where K is derived from the desired $S_4 \leq 1$ via Eq. (3.5) and the relation $m = 1/S_4^2$. The direct component $\tilde{\bar{z}}$ is summed with $\tilde{\xi}(t)$, and the resulting process $\tilde{z}(t)$ is normalized by $\tilde{\alpha} = E[|\tilde{z}(t)|]$ to produce the synthetic scintillation time history $z(t) = \bar{z} + \xi(t)$.

The 2nd-order Butterworth filter in Fig. 3.4 is most conveniently implemented as a discrete-time filter, and the noise $n(t)$ as a sequence of independent samples from a random number generator. To ensure proper steady-state statistics of the filtered noise

process $\tilde{\xi}(t)$, one must either allow the filter to settle before using its output or implement an initialization procedure based on a discrete Lyapunov computation of the steady-state covariance matrix corresponding to the filter's two states.

The severity of the scintillation time history $z(t)$ is determined by the values of τ_0 and S_4. In general, high S_4 and low τ_0 give the most severe scintillation. For reference, the GPS data in the scintillation library—recorded using a stationary L_1 receiver—manifest $0 < S_4 \lesssim 1$ and $0.5 \leq \tau_0 < 2$ seconds [1]. Receivers mounted on dynamic platforms will see a broader range of τ_0. Extreme scintillation in the library's Wideband UHF records manifests τ_0 values as low as 0.12 seconds.

A convenient lumped scintillation severity index can be had by calculating T_e as a function of S_4 and τ_0, as described in [1]. Then, when testing a typical GPS phase tracking loop using a simulated $z(t)$, a test engineer can expect the mean time between cycle slips T_s to be slightly longer than T_e.

3.4 Model Validation

The following strategy was adopted for validating the proposed scintillation model. First, time histories of "truth" scintillation were obtained. These were either generated using the previously described phase screen model (with two phase screens) or were drawn from Wideband UHF records in the scintillation library. In the latter case, relatively stationary scintillation intervals exceeding 150 seconds in length were chosen. The scintillation library's GPS data were excluded from the validation tests because of their thermal noise contamination. Nonetheless, as demonstrated in [1], there is no qualitative difference between the Wideband UHF and GPS scintillation data, apart from the noise contamination. Hence, the Wideband UHF data may be thought of as extreme

L-band scintillation and remains useful for testing receiver tracking loops.

In the next step, the truth data were detrended as described in Section 3.3.2, and the S_4 and τ_0 parameters for each truth set were estimated. The estimated value of τ_0 is the value that optimizes—in the least squares sense—the fit of the proposed autocorrelation model [Eq. (3.7)] to the first 40 ms of the empirical autocorrelation function.

Next, for each truth data set, 10 independent realizations of synthetic scintillation were generated, each equal in length to the truth set and matched to the S_4 and τ_0 parameters estimated from the truth set. The truth set and the 10 synthetic realizations were then passed as inputs to the scintillation testbed described in [1]. The dot-product four-quadrant arctangent, decision-directed four-quadrant arctangent, two-quadrant arctangent, decision-directed, and conventional Costas phase detectors were evaluated. A phase tracking loop noise bandwidth $B_n = 10$ Hz and an accumulation interval $T_a = 10$ ms were assumed. These values were found in [1] to lead to good tracking behavior. For all tests, the additive white noise that is typically used to simulate receiver thermal noise was eliminated, effectively making the tracked signals' carrier-to-noise ratios infinite. This was done so that the effects of scintillation could be studied in isolation from the effects of thermal noise.

The response of each phase tracking loop to the scintillation was noted in terms of the phase error variance σ_φ^2 and the number of cycle slips N_s over each test interval. Means and standard deviations of σ_φ^2 and N_s were computed for the synthetic data from tests using the 10 independent realizations. Results are presented in Table 3.2 for two phase-screen-generated truth sets, and in Table 3.3 for four empirical truth sets. The results presented are for the decision-directed four-quadrant arctangent phase detector, but are representative of the results for all the phase detectors tested. In the tables, T denotes the length of the test in seconds, and the spread about the means of σ_φ^2 and N_s

for the synthetic scintillation represents one standard deviation.

Table 3.2: Scintillation Effects Comparison: Phase Screen Truth Data

Parameters			**Truth Scint.**		**Synthetic Scint.**	
S_4	τ_0 (s)	T (s)	σ_φ (deg)	N_s	σ_φ (deg)	N_s
1.0	0.28	328	16.3	60	16.8 ± 0.2	70.7 ± 7.3
0.79	0.33	328	5.2	3	9.2 ± 0.3	12.1 ± 3.3

Table 3.3: Scintillation Effects Comparison: Empirical Truth Data

Parameters			**Truth Scint.**		**Synthetic Scint.**	
S_4	τ_0 (s)	T (s)	σ_φ (deg)	N_s	σ_φ (deg)	N_s
0.87	0.18	200	16.4	32	17.5 ± 0.5	35.9 ± 4.7
1.0	0.36	265	14.1	37	15.0 ± 0.5	41.6 ± 5.9
0.69	0.18	174	12.7	12	11.8 ± 0.9	5.6 ± 1.6
0.87	0.26	225	11.6	23	12.7 ± 0.5	19.2 ± 4.6
0.61	0.47	162	3.96	0	3.63 ± 0.2	0.10 ± 0.3
0.96	0.09	81	28.5	60	32.7 ± 1.0	69.4 ± 5.8
0.95	0.26	123	14.1	21	15.6 ± 0.5	19.8 ± 3.7
0.51	0.71	138	2.12	0	1.60 ± 0.1	0 ± 0

In general, the tracking loops' responses to the truth and to the synthetic scintillation are very similar. Two exceptions are the second phase-screen-generated test, whose poor correspondence can be attributed to the distortion of $p(\alpha)$ mentioned in Section 3.3.1, and the cycle slip count in the third empirical test. In all other cases (besides the $N_s = 0$ cases for which a percentage difference is not defined but the correspondence is obviously good), the σ_φ^2 and N_s values for the synthetic scintillation are within 25% of those for the true scintillation. On the whole, these results suggest that, for testing the

response of GPS phase tracking loops to scintillation, the proposed scintillation model is useful and the scintillation it produces is realistic.

3.5 Conclusions

A scintillation model has been proposed that exploits the close connection between differentially-detected data bit errors and cycle slips in GPS phase tracking loops. The connection implies that, from the perspective of a tracking loop trying to maintain lock during scintillation, the critical scintillation properties are the amplitude distribution and the autocorrelation function of the scintillation's rapidly-varying complex component. Studies presented here using phase-screen-generated and empirical scintillation data show that the amplitude distribution is well-modeled as a Rice distribution and the autocorrelation function as that corresponding to a low-pass 2nd-order Butterworth filter. Such models can be easily combined and mechanized as a scintillation simulator that takes as inputs the scintillation index S_4 and the decorrelation time τ_0, and outputs realistic scintillation. The mean time between errors in differentially-detected data bits can be calculated from the simulator inputs and serves as a convenient lumped index of scintillation severity. The proposed scintillation model has been validated in comparison tests with phase-screen-generated and empirical scintillation data.

Chapter 4

Magnetometer-based Attitude and Rate Estimation for a Spacecraft with Wire Booms

T. Humphreys, M. Psiaki, E. Klatt, S. Powell, and P. M. Kintner, Jr., "Magnetometer-based attitude and rate estimation for a spacecraft with wire booms," *Journal of Guidance, Control, and Dynamics*, vol. 28, no. 4, pp. 584–593, July 2005.

4.1 Abstract

A magnetometer-based filter and smoother are presented for estimating attitude, rate, and boom orientations for a spinning spacecraft that has wire booms. These estimates are needed to analyze science data from the subpayloads of a recent sounding rocket mission. The estimator is initialized with the measured angular rate of each subpayload at ejection and thereafter relies solely on three-axis magnetometer data. The estimation process is complicated by the flexible wire booms whose full parameterization for even the simplest pendulous modes would require 16 state elements. Several simplifying assumptions about the motion of the booms reduce the problem's complexity. A magnetometer-based attitude and rate estimator is developed which is suited to the time-varying model errors resulting from these assumptions. The estimator uses inertial angular momentum in place of angular rate in its state vector, and it explicitly includes an error model for its approximate relationship between angular rate and angular momentum. The estimator, a filter/smoother, is applied to synthetic data from a truth-model simulator and then to actual telemetry from the mission subpayloads. Accuracies are on the order of several degrees. The estimator is applicable whenever Euler-type equa-

tions must be used to propagate rate estimates in the presence of significant dynamics modeling errors.

4.2 Introduction

The present work draws its impetus from the sounding rocket experiment known as SIERRA (Sounding of the Ion Energization Region: Resolving Ambiguities), launched from Poker Flat, Alaska in January of 2002. Roughly 350 seconds before apogee, the primary SIERRA payload ejected two smaller spacecraft at an interval of 33 seconds between ejections. The three spin-stabilized payloads continued along a ballistic trajectory, finally reaching apogee at 735 km before falling earthward. Total flight time was about 950 seconds [48]. The separate payloads were essential to resolving a temporal/spatial ambiguity in electric field measurements of the ionosphere. Also critical was a broad measurement baseline for each payload. Mission specifications called for four probes extending radially from each payload's nominal axis of rotation, with opposing probes separated by 6 meters. This was a challenge particularly for the subpayloads, whose compactness barred the use of rigid booms. SIERRA designers ultimately satisfied the opposing broad baseline and compactness requirements via the Cornell Wire Boom Yo-Yo (COWBOY) system [49, 50]. Probes were connected to flexible cables wound helically around an articulating drum, and then spun out during flight in a yo-yo-type deployment that was controlled by a damper.

An estimate of spacecraft attitude and boom orientations for each payload enables researchers to correlate telemetry with spatial features of the background electric field. For the primary payload, with rigid booms and a comprehensive attitude sensor suite consisting of inertial sensors and a three-axis magnetometer (TAM), formulating an

attitude estimate is conceptually straightforward. The subpayloads present more of a challenge. Much more compact and lighter than the primary payload, their only attitude sensor is an onboard TAM. Each TAM measurement provides two axes of attitude information. This is insufficient for single-frame attitude estimation, obliging reliance on both an Euler model, for propagation of the spacecraft dynamics between measurements, and an initial estimate of the angular momentum vector. The complex dynamics of the flexible wire booms are difficult to incorporate directly into an estimation algorithm. Therefore, modeling approximations are used, but these introduce uncertainty into the Euler model. The estimation challenge for the subpayloads is tersely restated in the following terms: 3-axis attitude, rate, and boom orientation estimates are desired in the face of significant time-varying modeling uncertainty and weak observability about one axis.

Previous research efforts have produced various results that can be used to synthesize a solution to the SIERRA subpayload attitude estimation problem. A general dynamics analysis of spacecraft employing wire-boom antennas was presented in [51]. Work on another sounding rocket mission recognized the challenges posed by structural flexibility in Euler-based attitude and rate estimation [52]. In particular, it was found that rigid-body models are inadequate when significant flexible modes are present. In contrast to the present case, however, the sounding rocket of [52] was equipped with semi-rigid booms and multiple attitude sensors that provided data during most of its flight.

A substantial body of research has dealt with magnetometer-only attitude estimation applied to rigid spacecraft [53–57]. These methods rely on accurate Euler models of the spacecraft dynamics because of the lack of rate-gyro data. The Euler models are used to estimate attitude rates and to observe the attitude about the axis that is not already sensed. These models assume accurate prior knowledge of the spacecraft inertial

parameters. In [56] it is demonstrated that estimates of inertia matrix parameters may be refined by including these as part of the estimated state. This applies, however, to the inertia parameters of a rigid body. A similar approach would be unworkable in the present case due to the complexity of the wire boom system. Many of the flexible-body modes are themselves unobservable purely from magnetometer data, and a significant number of the inertial parameters, such as the tip-mass values, are equally unobservable.

Attitude observability for magnetometer-based estimation is dependent upon movement of the local magnetic field vector's direction in inertial space. This movement is primarily a consequence of the spacecraft's motion along its orbit. An additional challenge for SIERRA attitude estimation is that the sounding rocket trajectory is short. Over the course of the 700 second data capture phase, the magnetic field moves only 13.6 degrees in inertial coordinates.

A consequence of this condition is increased reliance on an initial estimate of each subpayload's angular momentum vector. These estimates are provided at separation by inertial sensors onboard the primary payload. The low level of external torques for the SIERRA mission implies that the angular momentum vector for each subpayload remains nearly fixed in inertial space. Therefore, the initial angular momentum acts almost like an independent attitude reference throughout the duration of the flight.

The filter and smoother developed in this paper are Euler-based estimators that exploit prior knowledge of the spacecraft angular momentum while gracefully accommodating errors that arise from unmodeled torques and from approximation of the effects of the flexible modes. The estimated state vector in the new filter/smoother directly includes the angular momentum components in inertial coordinates in place of the more common angular rate vector. The benefit of this approach is that, owing to conservation of angular momentum, the prediction step for this vector is essentially trivial. This is

important because modeling errors, when coupled with nonlinearities, would otherwise bleed into the rate propagation and ultimately express themselves in a wandering inertial angular momentum vector. This unforced wander is undesirable especially when one axis is weakly observable, as in the present case, since errors accumulating about the weakly observable axis are not easily corrected.

Euler-model errors are accommodated in the estimator by including a random uncertainty model for the relationship between the angular rate and the angular momentum in spacecraft coordinates. This extra source of random uncertainty is important in the present problem for the following reason: The significant effects of the spacecraft's flexible modes are included through an approximate relationship between angular velocity and angular momentum that is tailored to be relatively accurate for the dominant mode of motion. This dominant mode is the flexible-body equivalent of the nutation mode of a rigid minor-axis spinner. The random uncertainty model is included in the spacecraft kinematics exactly where the approximate angular-rate/angular-momentum relationship is invoked. This approach more accurately models the way errors are introduced into the Euler model than does, say, a simple increase of the modeled disturbance torque.

The three main contributions of this paper to attitude estimation techniques are: 1) Use of the inertially-referenced angular momentum components in the state vector in place of the body-referenced angular velocity components, 2) Inclusion of a random error model in the angular-momentum/angular-velocity relationship, and 3) An approximate angular-momentum/angular-velocity relationship that is valid for unstable nutation of a spinning spacecraft with flexible wire booms. These contributions are key to successful magnetometer-based attitude estimation for spinning spacecraft with wire booms. Their utility is demonstrated by successful application of a filter and a smoother employing these techniques to the problem of the SIERRA subpayloads. Contributions

1) and 2) should also prove useful for Euler-based attitude and rate estimation for any spacecraft if there is significant modeling uncertainty in the Euler dynamics model.

The balance of this paper is laid out as follows. A mathematical model of the flexible spacecraft motion is presented in Section 4.3, and several simplifying assumptions are motivated and used to develop a relationship between the angular momentum and the angular velocity. Section 4.4 provides a summary of the attitude parameterization used, then proceeds to develop the estimator. The estimator is evaluated in Section 4.5 using synthetic data from a truth-model simulation, and it is evaluated in Section 4.6 using data telemetered from the SIERRA subpayloads. Section 4.7 considers other situations in which the paper's techniques apply, and Section 4.8 presents the paper's conclusions.

4.3 Flexible-Body Model and Simplifying Assumptions

The essential features of the deployed SIERRA subpayloads are represented in Fig. 4.1. Four 3-m wire booms nominally spanning a plane are oriented radially about the spin axis. The articulating upper drum, which is used to control the unwinding of the wire booms during deployment, and about which the wire booms are wrapped in the stowed configuration, is held fast by a locking brake after deployment. This implies that the drum and the main spacecraft body may be modeled as a single rigid body. The center of mass of this rigid body constitutes the origin of the spacecraft body reference frame. The body z-axis, z_b, is aligned along the nominal spin axis. When the flexible booms are added, a system center of mass may be defined, which is, in general, slightly displaced from the center of mass of the main-body-plus-drum system. The translational motion of the system center of mass is independent of attitude, and this fact can be used to advantage when deriving the equations governing the attitude dynamics. Attitude

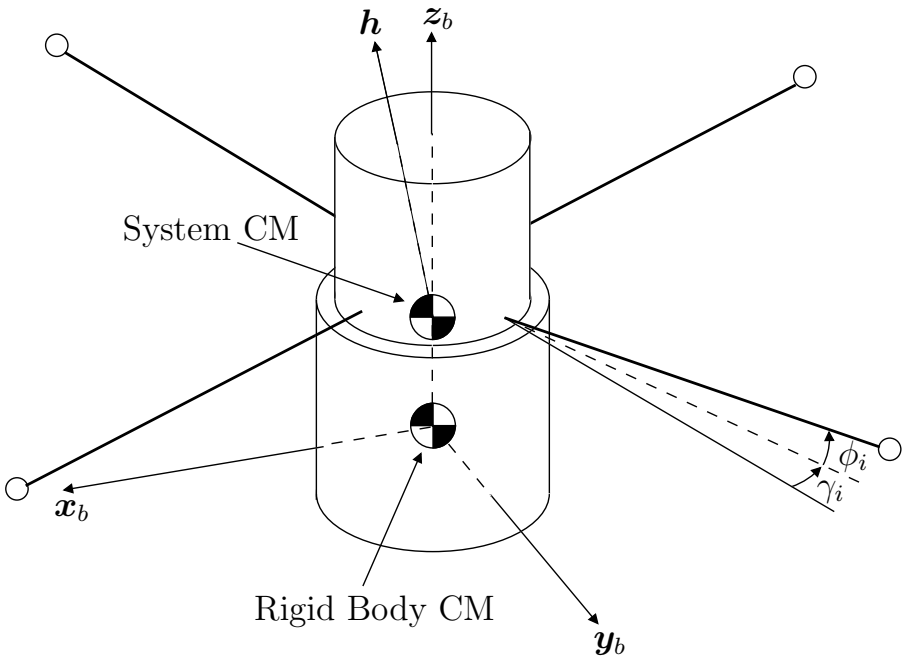

Figure 4.1: Geometry of the SIERRA subpayloads.

is measured with respect to an inertial reference frame whose axes are aligned with those of the mean J2000 Earth-centered inertial reference frame. The system angular momentum is given as the vector $\boldsymbol{h}$. Boom vibrational modes beyond the first order (pendulous) mode are assumed to be negligible. This is a good approximation for the SIERRA subpayloads [49–51]. Hence, the physical wire booms which are flexible all along their length are modeled as simple pendulums for purposes of simulation and estimation. In this work, both the physical booms and their model are described as flexible because their positions can deform with respect to spacecraft coordinates. Out-of-plane and in-plane deflections of the i^{th} boom are denoted by the angles ϕ_i and γ_i. Note that this represents a notational shift from [49, 50] wherein θ_i denotes the in-plane boom deflection.

A comprehensive dynamics model for a general case with N booms is found in [49]. This may be used to construct, for the four-boom case, a dynamics model of the form

$\dot{\boldsymbol{x}} = f(\boldsymbol{x}, \boldsymbol{n})$ governing the time evolution of a 23-element state vector $\boldsymbol{x}$. The state vector is composed of the angular rate vector of the rigid body, $\boldsymbol{\omega}$, the attitude quaternion $\boldsymbol{q}$, the angles $\phi_i,\ \gamma_i$, and their first time derivatives,

$$\boldsymbol{x} = \left[\boldsymbol{\omega}^T, \boldsymbol{q}^T, \phi_1, \dot{\phi}_1, \gamma_1, \dot{\gamma}_1, \ldots, \phi_4, \dot{\phi}_4, \gamma_4, \dot{\gamma}_4\right]^T \tag{4.1}$$

External torques act on the system through the vector $\boldsymbol{n}$.

Insight into the behavior of the spacecraft and flexible booms is had by by linearizing $f(\boldsymbol{x}, \boldsymbol{n})$ about a nominal state and examining the characteristic motion of the linearized system. The SIERRA subpayloads nominally rotate about the z_b axis at an angular rate of 1.7 Hz. The in- and out-of-plane angles γ_i and ϕ_i and their first time derivatives are nominally zero. Linearization about these nominal values (and a chosen $\boldsymbol{q}$) yields a linearized dynamics model of the form $\Delta\dot{\boldsymbol{x}} = F\Delta\boldsymbol{x}$ valid for small perturbations about the nominal values. Eigenvalue analysis of the linearized dynamics matrix F reveals a slightly unstable nutational mode–a result of design constraints that leave the subpayloads spinning about the rigid-body equivalent of their minor inertia axes. As a consequence, energy dissipation in the flexible booms drives an increase in the spacecraft nutation angle (the angle between $\boldsymbol{h}$ and z_b), and leads finally to rotation about the equivalent of the major rigid-body inertia axis. Due to the short duration of the flight, the unstable mode and consequent slow growth of the nutation angle were considered acceptable [50].

The rate of growth of the unstable mode and the decay time constants of the stable modes are functions of the energy dissipated by bending in the booms. A lumped dissipation parameter was calculated for the SIERRA subpayloads in pre- and post-launch empirical studies, predicting stable mode time constants of less than 300 seconds [49, 50]. Immediately following boom deployment, spacecraft motion may be expected to contain contributions from several different modes. Within a short interval

the nutational mode dominates as the stable modes die out.

An important feature of the nutational mode in the SIERRA design is that as long as the nutation angle is small (< 15 degrees), in-plane displacements of the wire booms are very small (< 1/2 degree). Moreover, to a very good approximation, the booms remain perpendicular to the angular momentum vector (within 1/2 degree). Using this perpendicularity approximation, the angles ϕ_i and rates $\dot{\phi}_i$ can be estimated if $\boldsymbol{h}$ is known in spacecraft body coordinates (call this latter quantity $\boldsymbol{h}_{sc}$). These features of boom motion motivate the following approximations which greatly simplify the spacecraft dynamics model:

$$\gamma_i = \dot{\gamma}_i = 0, \quad i = 1, ..., 4 \tag{4.2}$$

$$\boldsymbol{c}_i^T \boldsymbol{h}_{sc} = 0, \quad i = 1, ..., 4 \tag{4.3}$$

Here, the unit vector $\boldsymbol{c}_i = \boldsymbol{c}_i(\phi_i)$ is aligned along the i^{th} boom.

An implicit relationship between $\boldsymbol{h}_{sc}$, $\boldsymbol{\omega}$, and the boom angles ϕ_i and rates $\dot{\phi}_i$ follows from these simplifying assumptions. First, angular momentum about the system center of mass is expressed in body coordinates as

$$\boldsymbol{h}_{sc} = -m_b(\boldsymbol{r}_{cm} \times \boldsymbol{v}_b) + J_b\boldsymbol{\omega} + \sum_{i=1}^{4} m_i(\boldsymbol{r}_i - \boldsymbol{r}_{cm}) \times \boldsymbol{v}_i \tag{4.4}$$

under the following definitions, where all vectors are in body coordinates:

m_b	mass of the main spacecraft body plus drum
$\boldsymbol{r}_{cm} = \boldsymbol{r}_{cm}(\phi_1, \phi_2, \phi_3, \phi_4)$	vector from the main body/drum CM to the system CM
$\boldsymbol{v}_b = \boldsymbol{v}_b(\phi_1, ..., \phi_4, \dot{\phi}_1, ..., \dot{\phi}_4)$	inertial velocity of the main body/drum CM
J_b	moment-of-inertia matrix of the main body/drum
m_i	effective tip mass of the i^{th} boom
	(includes 1/3 of the mass of the i^{th} cable)
$\boldsymbol{r}_i = \boldsymbol{r}_i(\phi_i)$	vector from the main body/drum CM to the i^{th} tip mass
$\boldsymbol{v}_i = \boldsymbol{v}_i(\phi_1, ..., \phi_4, \dot{\phi}_1, ..., \dot{\phi}_4)$	inertial velocity of the i^{th} tip mass

The functions $\boldsymbol{r}_{cm}(\phi_1, ..., \phi_4)$, $\boldsymbol{v}_b(\phi_1, ..., \phi_4, \dot{\phi}_1, ..., \dot{\phi}_4)$, $\boldsymbol{r}_i(\phi_i)$, $\boldsymbol{v}_i(\phi_1, ..., \phi_4, \dot{\phi}_1, ..., \dot{\phi}_4)$, and $\boldsymbol{c}_i(\phi_i)$ are all defined in [49].

Second, the approximation of Eq. (4.3), repeated here for convenience, is considered together with its first time derivative:

$$\boldsymbol{c}_i^T(\phi_i)\boldsymbol{h}_{sc} = 0, \quad i = 1, ..., 4 \tag{4.5}$$

$$\dot{\phi}_i \left[\frac{d\boldsymbol{c}_i}{d\phi_i}\right]^T \boldsymbol{h}_{sc} + \boldsymbol{c}_i^T(\phi_i)[-\boldsymbol{\omega} \times \boldsymbol{h}_{sc}] = 0, \quad i = 1, ..., 4 \tag{4.6}$$

where the second term on the left-hand side of Eq. (4.6) assumes that $\dot{\boldsymbol{h}}_{sc} = -\boldsymbol{\omega} \times \boldsymbol{h}_{sc}$, which is true if external torque is zero. Equation (4.5) implicitly defines (under mild smoothness conditions) each ϕ_i in terms of $\boldsymbol{h}_{sc}$:

$$\phi_i = \phi_i(\boldsymbol{h}_{sc}), \quad i = 1, ..., 4 \tag{4.7}$$

Thus, given $\boldsymbol{h}_{sc}$, one can solve for each ϕ_i and hence each $\boldsymbol{c}_i(\phi_i)$. Substitution into Eq. (4.6), yields $\dot{\phi}_i$ as a function of $\boldsymbol{h}_{sc}$ and as a linear function of $\boldsymbol{\omega}$:

$$\dot{\phi}_i = \dot{\phi}_i(\boldsymbol{h}_{sc}, \boldsymbol{\omega}), \quad i = 1, ..., 4 \tag{4.8}$$

With these relations, the vectors on the right hand side of Eq. (4.4) may be written in terms of $\boldsymbol{h}_{sc}$ and $\boldsymbol{\omega}$, and the resulting equation takes the form

$$\boldsymbol{h}_{sc} = J(\boldsymbol{h}_{sc})\boldsymbol{\omega} \tag{4.9}$$

This form arises because of the linear dependence of $\boldsymbol{v}_b$ and $\boldsymbol{v}_i$ on $\dot{\phi}_1 ... \dot{\phi}_4$ and $\boldsymbol{\omega}$. The matrix function $J(\boldsymbol{h}_{sc})$ is effectively an angular momentum-dependent moment-of-inertia matrix. Equation (4.9) may be inverted to yield $\boldsymbol{\omega}$ as a function of $\boldsymbol{h}_{sc}$:

$$\boldsymbol{\omega}(\boldsymbol{h}_{sc}) = J^{-1}(\boldsymbol{h}_{sc})\boldsymbol{h}_{sc} \tag{4.10}$$

4.4 Estimator Development

4.4.1 Attitude Representation

The magnetic field is the sole attitude measurement for the SIERRA subpayloads after separation from the primary payload. Hence, the greatest attitude uncertainty is in rotation and rate about the magnetic field vector. In [56], a 3-parameter attitude representation is developed which isolates rotation about the measured magnetic field vector in a single parameter, θ. Two other attitude parameters, α_1 and α_2, are used to account for magnetometer measurement noise. The full attitude parameterization is $\{\alpha_1, \alpha_2, \theta\}$, and may be introduced in the following manner:

If $\hat{\boldsymbol{b}}_{sc}$ is the unit vector in the direction of the measured magnetic field in the spacecraft reference frame and $\hat{\boldsymbol{b}}_{in}$ is the unit vector in the direction of the magnetic field in the inertial reference frame, then the quaternion relating the two reference frames is

parameterized as

$$\boldsymbol{q}(\alpha_1, \alpha_2, \theta) = \frac{1}{\sqrt{1 + \alpha_1^2 + \alpha_2^2}} \begin{bmatrix} \alpha_1 \hat{\boldsymbol{v}}_1 + \alpha_2 \hat{\boldsymbol{v}}_2 \\ 1 \end{bmatrix} \otimes \begin{bmatrix} \hat{\boldsymbol{b}}_{sc} \sin(\theta/2) \\ \cos(\theta/2) \end{bmatrix} \otimes \boldsymbol{q}_{min}(\hat{\boldsymbol{b}}_{sc}, \hat{\boldsymbol{b}}_{in}) \quad (4.11)$$

where $\hat{\boldsymbol{v}}_{1,2}$ are unit vectors that, together with $\hat{\boldsymbol{b}}_{sc}$, form a right-hand orthonormal triad, and the symbol $\otimes$ denotes quaternion composition. The minimum quaternion $\boldsymbol{q}_{min}(\hat{\boldsymbol{b}}_{sc}, \hat{\boldsymbol{b}}_{in})$ is the quaternion of minimum rotation that maps $\hat{\boldsymbol{b}}_{in}$ into $\hat{\boldsymbol{b}}_{sc}$.

Figure 4.2 illustrates the rotations associated with each attitude parameter. The parameter θ corresponds to a rotation about the measured magnetic field vector in spacecraft coordinates. The parameters α_1 and α_2 correspond to respective rotations about axes $\hat{\boldsymbol{v}}_1$ and $\hat{\boldsymbol{v}}_2$. Note by Eq. (4.11) that α_1 and α_2 approximately equal $1/2$ of the total rotation about $\hat{\boldsymbol{v}}_1$ and $\hat{\boldsymbol{v}}_2$, respectively. This can be seen by comparing the first quaternion on the right-hand side of Eq. (4.11) with the general form of the quaternion in which the axis of rotation is scaled by the factor $\sin(\theta/2)$, which, in the small-angle approximation, is $1/2$ of the rotation angle θ. When combined in Eq. (4.11) under the small-angle approximation, α_1 and α_2 produce a total rotation angle of $2\sqrt{\alpha_1^2 + \alpha_2^2}$ about the rotation vector $\alpha_1 \hat{\boldsymbol{v}}_1 + \alpha_2 \hat{\boldsymbol{v}}_2$ to correct for errors in $\hat{\boldsymbol{b}}_{sc}$, as depicted in Fig. 4.2.

The attitude singularity associated with this 3-parameter attitude representation occurs at 180 degrees rotation about any vector perpendicular to the measured magnetic field. It is avoided because α_1 and α_2, which represent rotation about vectors perpendicular to $\boldsymbol{b}_{sc}$, also parameterize the magnetometer measurement errors. Small magnetometer measurement errors lead to small values for α_1 and α_2, and the singularity is avoided.

One advantage of this parameterization is that, as will be seen in a later section, it provides for a simple model relating magnetic field measurements to spacecraft attitude.

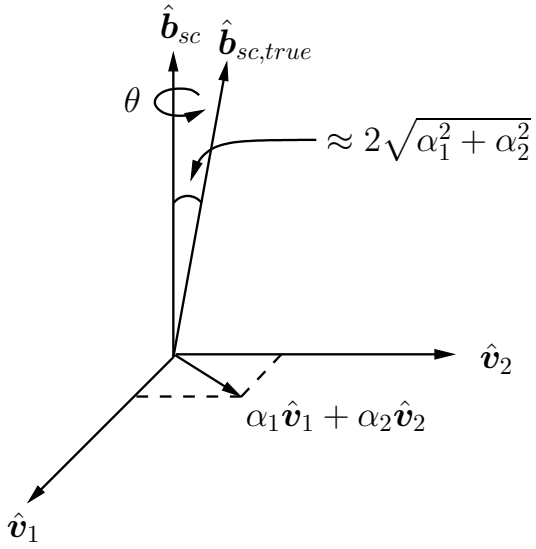

Figure 4.2: Attitude parameters θ, α_1, and α_2 and their corresponding rotation angles.

4.4.2 Estimator State Vector

The state vector of the new filter/smoother is

$$\boldsymbol{x} = \left[\boldsymbol{h}_{in}^T, \alpha_1, \alpha_2, \theta\right]^T \tag{4.12}$$

where angular momentum expressed in inertial coordinates has been included with the attitude parameterization of the previous section. The inclusion of $\boldsymbol{h}_{in}$ represents a departure from typical state vectors used to estimate spacecraft attitude and rate. These commonly employ angular rate $\boldsymbol{\omega}$ instead of $\boldsymbol{h}_{in}$. The rationale behind this replacement will become clear in later sections as the estimator is formulated and tested.

It should be pointed out that the state vector presented here is sufficient to describe the angular rate of the rigid body and the boom orientations, provided the simplifying assumptions of Eqs. (4.2) and (4.3) are valid. This can be seen by using the attitude parameterization to map $\boldsymbol{h}_{in}$ into spacecraft body coordinates,

$$\boldsymbol{h}_{sc} = A[\boldsymbol{q}(\alpha_1, \alpha_2, \theta)]\boldsymbol{h}_{in}$$

where $A[\boldsymbol{q}]$ is the direction-cosine matrix equivalent of the quaternion $\boldsymbol{q}$. The function $\boldsymbol{\omega}(\boldsymbol{h}_{sc})$ is then used to compute $\boldsymbol{\omega}$ in body coordinates. Finally, out-of-plane boom angles ϕ_i are calculated using Eq. (4.7), and in-plane boom angles γ_i are assumed to be zero, following the assumption in Eq. (4.2).

4.4.3 State Observability

A brief discussion of state observability will aid understanding of the filter and smoother behavior. Any single magnetometer measurement provides only two axes of attitude information, but a series of measurements is, under modest conditions, sufficient for full attitude and rate observability. The reasoning for this is as follows. Except under very restrictive circumstances (when the spacecraft angular momentum vector and the magnetic field are aligned), the angular rate $\boldsymbol{\omega}$ is observable from a series of vector magnetometer measurements [57]. The spacecraft-referenced angular momentum $\boldsymbol{h}_{sc}$ can then be calculated using Eq. (4.9). Presuming the spacecraft location is known (e.g. from an onboard GPS receiver), the vector $\hat{\boldsymbol{b}}_{in}$ may be calculated using a geomagnetic field model. The vector $\hat{\boldsymbol{b}}_{sc}$ is given by magnetometer measurements. If the vector $\boldsymbol{h}_{in}$ were also known, the set $\{\boldsymbol{h}_{sc}, \boldsymbol{h}_{in}, \hat{\boldsymbol{b}}_{sc}, \hat{\boldsymbol{b}}_{in}\}$ would completely determine the spacecraft attitude $\{\alpha_1, \alpha_2, \theta\}$, provided $\boldsymbol{h}_{in}$ and $\hat{\boldsymbol{b}}_{in}$ were not aligned. This well-known result is embodied in the algebraic (TRIAD) method of attitude determination [58]. State observability is thus reduced to observation of $\boldsymbol{h}_{in}$.

The magnitude of $\boldsymbol{h}$ and the relationship between $\boldsymbol{h}$ and $\hat{\boldsymbol{b}}$ are invariant from one reference frame to another. Hence, from corresponding quantities in the body reference frame, the magnitude $\|\boldsymbol{h}_{in}\|$ and the component of $\boldsymbol{h}_{in}$ along $\hat{\boldsymbol{b}}_{in}$ are known, which leaves only one unknown component of $\boldsymbol{h}_{in}$. Because external torques are assumed to be neg-

ligible, $\boldsymbol{h}_{in}$ remains fixed in inertial coordinates. If $\hat{\boldsymbol{b}}_{in}$ moves between measurements, then the projection of $\boldsymbol{h}_{in}$ onto the span of two measurements may be calculated from the component along each measurement. This situation is illustrated in Fig. 4.3. The component of $\boldsymbol{h}_{in}$ orthogonal to the plane spanned by $\hat{\boldsymbol{b}}_{in}(t_1)$ and $\hat{\boldsymbol{b}}_{in}(t_2)$ may be calculated from knowledge of $\|\boldsymbol{h}_{in}\| = \|\boldsymbol{h}_{sc}\|$, to within a sign uncertainty. Any $\hat{\boldsymbol{b}}_{in}$ at a 3^{rd} time that moves out of the plane resolves the sign uncertainty.

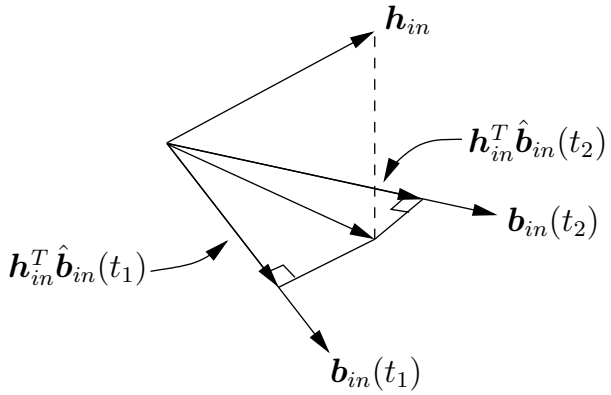

Figure 4.3: Relationship between $\boldsymbol{h}_{in}$ and the magnetic field vector at times t_1 and t_2.

The key point here is that movement of $\hat{\boldsymbol{b}}_{in}$ in inertial space is crucial to observation of $\boldsymbol{x} = \left[\boldsymbol{h}_{in}^T, \alpha_1, \alpha_2, \theta\right]^T$. Of course, very small movements of $\hat{\boldsymbol{b}}_{in}$ result in weak state observability, whereas larger transits approaching 90 degrees strengthen the observation.

Owing to a short flight duration, the SIERRA subpayloads do not enjoy large excursions of $\hat{\boldsymbol{b}}_{in}$. The total change in the magnetic field direction over 700 seconds of data capture is less than 14 degrees. Weak observability in this case demands accuracy in the *a priori* momentum estimate, $\hat{\boldsymbol{h}}_{in(0)}$ (the circumflex here denotes an estimate, not a unit vector as for $\hat{\boldsymbol{b}}_{sc}$). Errors in the magnitude of $\hat{\boldsymbol{h}}_{in(0)}$ and in its component along $\hat{\boldsymbol{b}}_{in}$ are readily corrected by magnetometer measurements, whereas errors orthogonal to the plane spanned by $\{\hat{\boldsymbol{h}}_{in(0)}, \hat{\boldsymbol{b}}_{in}\}$ are not immediately visible because they constitute rotation of $\hat{\boldsymbol{h}}_{in(0)}$ about $\hat{\boldsymbol{b}}_{in}$. They can be corrected only through movement of $\hat{\boldsymbol{b}}_{in}$.

4.4.4 Dynamics and Kinematics Models

In the case of the SIERRA subpayloads, no control torques or significant environmental forces act on the spacecraft, so angular momentum is nearly conserved from one time step to the next. This fact, coupled with inclusion of $\boldsymbol{h}_{in}$ directly in the estimator state vector, leads to a very simple spacecraft dynamics model:

$$\boldsymbol{h}_{in(k+1)} = \boldsymbol{h}_{in(k)} + \boldsymbol{w}_k \tag{4.13}$$

The impulse $\boldsymbol{w}_k$ is a process noise term that accounts for disturbance torques. For the kinematics model, implicit trapezoidal integration is used to equate the angular rate with the eigenvector of rotation $\boldsymbol{e}$ and the average angular rate over the interval $(t_k,\ t_{k+1})$,

$$\frac{\boldsymbol{\omega}_{k+1}(\boldsymbol{h}_{sc(k+1)}) + \boldsymbol{p}_{k+1} + \boldsymbol{\omega}_k(\boldsymbol{h}_{sc(k)}) + \boldsymbol{p}_k}{2} = \left[\frac{\psi(\boldsymbol{s}_{k+1}, \boldsymbol{s}_k)}{t_{k+1} - t_k}\right] \boldsymbol{e}(\boldsymbol{s}_{k+1}, \boldsymbol{s}_k) \tag{4.14}$$

Here, the attitude portion of the estimator state vector has been abbreviated into the vector $\boldsymbol{s}_k$,

$$\boldsymbol{s}_k = \left[\alpha_{1(k)}, \alpha_{2(k)}, \theta_k\right]^T$$

The vector $\boldsymbol{e}(\boldsymbol{s}_{k+1}, \boldsymbol{s}_k)$ is the unit vector in the direction of the Euler rotation that takes the system from attitude $\boldsymbol{s}_k$ to attitude $\boldsymbol{s}_{k+1}$, and the angle $\psi(\boldsymbol{s}_{k+1}, \boldsymbol{s}_k)$ is the magnitude of this rotation. Reference [56] gives expressions for both of these quantities. It should also be noted that since $\boldsymbol{h}_{sc(k)} = A[\boldsymbol{q}(\boldsymbol{s}_k)]\boldsymbol{h}_{in(k)}$, the angular rate terms $\boldsymbol{\omega}_{k+1}$ and $\boldsymbol{\omega}_k$ on the left-hand side of Eq. (4.14) are dependent on $\boldsymbol{s}_{k+1}$ and $\boldsymbol{s}_k$.

The vectors $\boldsymbol{p}_{k+1}$ and $\boldsymbol{p}_k$ play a key role in accommodating the errors in the approximate function $\boldsymbol{\omega}(\boldsymbol{h}_{sc})$ that result from the simplified model of boom motion, where in-plane boom angles are assumed to be zero and out-of-plane boom angles are such that the booms are orthogonal to $\boldsymbol{h}_{sc}$. To the degree that spacecraft motion departs from uniform nutation, these approximations of boom motion are less valid, introducing more error into the $\boldsymbol{h}_{sc}$ to $\boldsymbol{\omega}$ conversion. Since $\boldsymbol{\omega}$ is not included as an element

of the state, application of the kinematic model in Eq. (4.14) requires calculation of $\boldsymbol{h}_{sc} = A[\boldsymbol{q}(\alpha_1, \alpha_2, \theta)]\boldsymbol{h}_{in}$ and conversion from $\boldsymbol{h}_{sc}$ to $\boldsymbol{\omega}$ via $\boldsymbol{\omega}(\boldsymbol{h}_{sc})$. The noise parameters $\boldsymbol{p}_{k+1}$ and $\boldsymbol{p}_k$ account for the errors introduced by this conversion.

It is important to note that, because the noise sequence $\boldsymbol{p}_k$ corresponds to macroscopic motion of the booms, it will be time-correlated. The estimator does not model any correlation of the $\boldsymbol{p}_k$ sequence, but its use of both $\boldsymbol{p}_{k+1}$ and $\boldsymbol{p}_k$ on the left-hand side of Eq. (4.14) constitutes a correlated model of the effect on the kinematics of this error sequence. This is further explained in the subsequent filter development.

4.4.5 Measurement Model

When the spacecraft attitude is parameterized based on the magnetometer measurement $\hat{\boldsymbol{b}}_{sc}$, as in [56], an uncomplicated measurement model results:

$$\begin{aligned} \begin{bmatrix} 0 \\ 0 \end{bmatrix} &= \begin{bmatrix} \mathbf{0} & 1 & 0 & 0 \\ \mathbf{0} & 0 & 1 & 0 \end{bmatrix} \begin{bmatrix} \boldsymbol{h}_{in(k)} \\ \alpha_{1(k)} \\ \alpha_{2(k)} \\ \theta_k \end{bmatrix} + \tilde{\boldsymbol{\nu}} \\ &= \tilde{C}\boldsymbol{x}_k + \tilde{\boldsymbol{\nu}} \end{aligned} \tag{4.15}$$

The 2×1 vector $\tilde{\boldsymbol{\nu}}$ represents measurement noise. The measurement model implies that, in the absence of noise, the parameters α_1 and α_2 are identically zero, and the true and measured magnetic field vectors in Fig. 4.2 are exactly aligned. Subsumed into $\tilde{\boldsymbol{\nu}}$ are contributions from several error sources including sensor noise, quantization noise, spacecraft position error, and geomagnetic field model error. The discrete sequence $\tilde{\boldsymbol{\nu}}$ is modeled as zero-mean uncorrelated Gaussian noise with covariance

$$E[\tilde{\boldsymbol{\nu}}_k \tilde{\boldsymbol{\nu}}_j^T] = \left[\sigma_{\tilde{\nu}}^2 I_{2\times 2}\right] \delta_{k,j} = P_{\tilde{\nu}\tilde{\nu}} \delta_{k,j} \tag{4.16}$$

4.4.6 Filtering

The discrete-time square-root information filter described here is based on material drawn from [56] and [59]. Departures from the filter presented in [56] are those required to incorporate the new state vector in which $\boldsymbol{h}_{in}$ replaces $\boldsymbol{\omega}$, and to incorporate the new model error sequence $\boldsymbol{p}_k$. The results of this paper are not dependent on a square-root implementation of the filter and smoother: an extended Kalman filter implementation would be equally effective. This is because round-off errors are much less significant than modeling errors in the SIERRA attitude estimation problem.

In the following, the overbar indicates an *a priori* estimate: an estimate of the state $\boldsymbol{x}_k$ based on measurements up to time t_{k-1}. The circumflex ($\hat{}$) denotes an *a posteriori* estimate: an estimate of the state $\boldsymbol{x}_k$ based on measurements up to time t_k. The filtering algorithm proceeds as follows:

1. Given an *a posteriori* state estimate

$$\hat{\boldsymbol{x}}_k = \left[\hat{\boldsymbol{h}}_{in(k)}^T, \hat{\alpha}_{1(k)}, \hat{\alpha}_{2(k)}, \hat{\theta}_k\right]^T = \left[\hat{\boldsymbol{h}}_{in(k)}^T, \hat{\boldsymbol{s}}_k^T\right]^T$$

   the attitude portion of the state, $\hat{\boldsymbol{s}}_k$, is used to convert $\hat{\boldsymbol{h}}_{in(k)}$ to spacecraft coordinates: $\hat{\boldsymbol{h}}_{sc(k)} = A[\boldsymbol{q}(\hat{\boldsymbol{s}}_k)]\hat{\boldsymbol{h}}_{in(k)}$. The relation $\boldsymbol{\omega}(\boldsymbol{h}_{sc})$ is then applied to obtain $\hat{\boldsymbol{\omega}}_k$ in spacecraft coordinates. A quaternion of rotation $\boldsymbol{q}_{rot}(\hat{\boldsymbol{\omega}}_k, \Delta t_k)$ is formed from $\hat{\boldsymbol{\omega}}_k$ and $\Delta t_k = t_{k+1} - t_k$. It describes the rotation during the sampling interval, assuming $\boldsymbol{\omega}$ is constant. This is used to construct the quaternion

$$\boldsymbol{q}(\bar{\boldsymbol{s}}_{k+1}) = \boldsymbol{q}_{rot}(\hat{\boldsymbol{\omega}}_k, \Delta t_k) \otimes \boldsymbol{q}(\hat{\boldsymbol{s}}_k) \tag{4.17}$$

   from which $\bar{\theta}_{k+1}$ may be extracted assuming *a priori* values $\bar{\alpha}_{1(k+1)} = \bar{\alpha}_{2(k+1)} = 0$, as described in Eqs. (28)-(30) of [56]. The *a priori* angular momentum $\bar{\boldsymbol{h}}_{in(k+1)}$ is calculated from Eq. (4.13) assuming $\boldsymbol{w}_k = 0$. The full *a priori* state estimate is

then

$$\bar{\boldsymbol{x}}_{k+1} = \left[\bar{\boldsymbol{h}}_{in(k+1)}^T, 0, 0, \bar{\theta}_{k+1}\right]^T$$

2. Equations (4.13) and (4.14) are each linearized about both $\hat{\boldsymbol{x}}_k$ and $\bar{\boldsymbol{x}}_{k+1}$ to produce the mapping equation

$$\boldsymbol{x}_k = \Phi_k \boldsymbol{x}_{k+1} + \Gamma_k \boldsymbol{w}_k + \Lambda_{k,k} \boldsymbol{p}_k + \Lambda_{k,k+1} \boldsymbol{p}_{k+1} + \xi_k \tag{4.18}$$

where ξ_k is a known non-homogeneous term.

3. Information equations are constructed from the measurement model in Eq. (4.15) and from noise models for $\boldsymbol{w}_k$ and $\boldsymbol{p}_{k+1}$. For convenience in working with the square-root information filter, information equations are square-root normalized such that the noise terms are distributed as $\sim N(0, I)$. For example, Eq. (4.15) is premultiplied by $R_{\tilde{\nu}\tilde{\nu}}$ where $(R_{\tilde{\nu}\tilde{\nu}}^T R_{\tilde{\nu}\tilde{\nu}})^{-1} = P_{\tilde{\nu}\tilde{\nu}}$, yielding

$$0 = C\boldsymbol{x}_k + \boldsymbol{\nu}_k \tag{4.19}$$

with $\boldsymbol{\nu}_k \sim N(0, I)$. Similarly, the information equations for $\boldsymbol{p}_{k+1}$ and $\boldsymbol{w}_k$ are

$$0 = \bar{R}_{pp(k+1)} \boldsymbol{p}_{k+1} + \boldsymbol{\nu}_{p(k+1)} \tag{4.20}$$

$$0 = \bar{R}_{ww} \boldsymbol{w}_k + \boldsymbol{\nu}_{w(k)} \tag{4.21}$$

with $\boldsymbol{\nu}_{(.)} \sim N(0, I)$.

4. The state $\boldsymbol{x}_k$ and noise term $\boldsymbol{p}_k$ are combined into an augmented state. The *a posteriori* information equation for this augmented state from the previous iteration is

$$\begin{bmatrix} \boldsymbol{z}_{p(k)} \\ \boldsymbol{z}_{x(k)} \end{bmatrix} = \begin{bmatrix} R_{pp(k)} & R_{px(k)} \\ 0 & R_{xx(k)} \end{bmatrix} \begin{bmatrix} \boldsymbol{p}_k \\ \boldsymbol{x}_k \end{bmatrix} + \begin{bmatrix} \boldsymbol{\nu}_{p(k)} \\ \boldsymbol{\nu}_{x(k)} \end{bmatrix} \tag{4.22}$$

again with $\boldsymbol{\nu}_{(.)} \sim N(0, I)$. The *a posteriori* state estimate $\hat{\boldsymbol{x}}_k$ and error covariance $P_{xx(k)}$ are related to this information equation by

$$\hat{\boldsymbol{x}}_k = R_{xx(k)}^{-1} \boldsymbol{z}_{x(k)}, \quad P_{xx(k)} = \left(R_{xx(k)}^T R_{xx(k)}\right)^{-1}$$

To perform time and measurement updates from time t_k to t_{k+1}, the square-root information filter minimizes the following least-squares cost function subject to the linearized dynamics mapping equation (4.18):

$$J = \left\| \begin{bmatrix} \boldsymbol{z}_{p(k)} \\ \boldsymbol{z}_{x(k)} \end{bmatrix} - \begin{bmatrix} R_{pp(k)} & R_{px(k)} \\ 0 & R_{xx(k)} \end{bmatrix} \begin{bmatrix} \boldsymbol{p}_k \\ \boldsymbol{x}_k \end{bmatrix} \right\|^2 + \|\bar{R}_{pp(k+1)}\boldsymbol{p}_{k+1}\|^2 \\ + \|\bar{R}_{ww}\boldsymbol{w}_k\|^2 + \|C\boldsymbol{x}_{k+1}\|^2 \tag{4.23}$$

Minimization of J is equivalent to maximization of the state vector's *a posteriori* conditional probability density function, making the current least-squares formulation a *maximum a posteriori* estimator. Combining the cost functional terms and eliminating $\boldsymbol{x}_k$ via Eq. (4.18) leads to

$$J = \left\| \begin{bmatrix} R_{pp(k)} + R_{px(k)}\Lambda_{k,k} & R_{px(k)}\Gamma_k & R_{px(k)}\Lambda_{k,k+1} & R_{px(k)}\Phi_k \\ 0 & \bar{R}_{ww} & 0 & 0 \\ 0 & 0 & \bar{R}_{pp(k+1)} & 0 \\ R_{xx(k)}\Lambda_{k,k} & R_{xx(k)}\Gamma_k & R_{xx(k)}\Lambda_{k,k+1} & R_{xx(k)}\Phi_k \\ 0 & 0 & 0 & C \end{bmatrix} \begin{bmatrix} \boldsymbol{p}_k \\ \boldsymbol{w}_k \\ \boldsymbol{p}_{k+1} \\ \boldsymbol{x}_{k+1} \end{bmatrix} \right. \\ \left. - \begin{bmatrix} \boldsymbol{z}_{p(k)} - R_{px(k)}\xi_k \\ 0 \\ 0 \\ \boldsymbol{z}_{x(k)} - R_{xx(k)}\xi_k \\ 0 \end{bmatrix} \right\|^2 \tag{4.24}$$

5. An orthogonal transformation found by QR factorizing the large block matrix in Eq. (4.24) is applied to both terms within the vector norm, triangularizing the

block matrix without affecting the magnitude of the overall vector norm,

$$J = \left\| \begin{bmatrix} R^*_{pp(k)} & R^*_{pw(k)} & R^*_{p(k)p(k+1)} & R^*_{p(k)x(k+1)} \\ 0 & R^*_{ww(k)} & R^*_{w(k)p(k+1)} & R^*_{w(k)x(k+1)} \\ 0 & 0 & R_{pp(k+1)} & R_{px(k+1)} \\ 0 & 0 & 0 & R_{xx(k+1)} \\ 0 & 0 & 0 & 0 \end{bmatrix} \begin{bmatrix} \boldsymbol{p}_k \\ \boldsymbol{w}_k \\ \boldsymbol{p}_{k+1} \\ \boldsymbol{x}_{k+1} \end{bmatrix} - \begin{bmatrix} z^*_{p(k)} \\ z^*_{w(k)} \\ z_{p(k+1)} \\ z_{x(k+1)} \\ \boldsymbol{\epsilon}_{k+1} \end{bmatrix} \right\|^2 \tag{4.25}$$

The matrices on the diagonal of the large block matrix in Eq. (4.25) are all square, non-singular, and upper-triangular. The asterisk ($*$) refers to quantities that will be used to do smoothing.

6. The *a posteriori* state estimate $\hat{\boldsymbol{x}}_{k+1}$ is solved for using $\hat{\boldsymbol{x}}_{k+1} = R^{-1}_{xx(k+1)} z_{x(k+1)}$. The quantity $\|\boldsymbol{\epsilon}_{k+1}\|^2$ represents the sum of the squared errors in the least-squares fit. The third and fourth lines of Eq. (4.25), which are like Eq. (4.22), are extracted for use in the next filter iteration, with k replaced by $k + 1$.

An important feature of the filtering algorithm is the evolution of the noise vector $\boldsymbol{p}_k$. At time step k, information equation (4.20) effectively resets $\boldsymbol{p}_{k+1}$, modeling it as being uncorrelated with previous values of $\boldsymbol{p}_k$. However, as can be seen in the structure of Eqs. (4.22) and (4.25), an *a posteriori* estimate of $\boldsymbol{p}_{k+1}$ forms part of the augmented state in the information equation for the next iteration. Note that an extended Kalman filter formulation of the filtering algorithm must likewise include the three elements of $\boldsymbol{p}_k$ in an augmented state vector. This one-step-memory process implements a time correlation model of the error in Eq. (4.14).

4.4.7 Fixed Interval Smoothing

The smoother problem formulation and solution algorithm use the same discrete-time square-root information structure as the filtering problem. The smoother performs a backwards pass on the data, taking as initial estimates the terminal estimates $\hat{\boldsymbol{x}}_N$ and $\hat{\boldsymbol{p}}_N$ provided by the filter. Equation (4.18), inverted to express $\boldsymbol{x}_{k+1}$ in terms of $\boldsymbol{x}_k$, is used as the mapping equation for the backwards pass. At each time step, information equations for smoothed estimates $\hat{\boldsymbol{x}}_{k+1|0:N}$ and $\hat{\boldsymbol{p}}_{k+1|0:N}$ are available in the form of Eq. (4.22) from the previous iteration (subscript notation employed here refers to the smoothed estimate at $k+1 \in [0, N]$ based on all data from 0 to N). These are combined with *a posteriori* data from iteration $k+1$ of the filtering pass by replacing the third and fourth lines of Eq. (4.25) with the R matrices and $\boldsymbol{z}$ vectors that are associated with $\hat{\boldsymbol{x}}_{k+1|0:N}$ and $\hat{\boldsymbol{p}}_{k+1|0:N}$. The quantity $\boldsymbol{x}_{k+1}$ is eliminated from the resulting cost by using Eq. (4.18) to solve for $\boldsymbol{x}_k$ in terms of $\boldsymbol{x}_{k+1}$, $\boldsymbol{w}_k$, $\boldsymbol{p}_k$ and $\boldsymbol{p}_{k+1}$. Finally, an appropriate orthogonal transformation is applied as in Step 5 of the filter to yield smoothed information equations for $\hat{\boldsymbol{x}}_{k|0:N}$ and $\hat{\boldsymbol{p}}_{k|0:N}$ that are independent of $\boldsymbol{w}_k$ and $\boldsymbol{p}_{k+1}$. The process is then repeated.

4.4.8 Filter Tuning

The process of filter tuning consists in choosing values for the *a priori* statistical models represented by matrices $R_{\tilde{\nu}\tilde{\nu}}$, $\bar{R}_{pp(k)}$, $\bar{R}_{ww}$, $R_{pp(0)}$, $R_{px(0)}$, and $R_{xx(0)}$, along with an initial state estimate $\hat{\boldsymbol{x}}_0$. (Because the smoother relies on *a posteriori* filter statistics, no additional smoother-specific tuning is required.) The tuning process typically proceeds by first relating parameter values to physical phenomena and then adjusting these values to achieve satisfactory filter performance as measured by truth-model simulation and innovations analysis.

The matrix $R_{\tilde{\nu}\tilde{\nu}}$, used to develop Eq. (4.19), is the square root of the inverse covariance of the zero-mean measurement noise $\tilde{\boldsymbol{\nu}}_k$. The statistics of $\tilde{\boldsymbol{\nu}}_k$ must account for geomagnetic field model errors as well as sensor and quantization noise. Model errors may be approximated by comparing a 7th-order 1995 geomagnetic model against a 10th-order, year 2000 model. Sensor and quantization noise are modeled for the SIERRA subpayload magnetometers as a random measurement error with a standard deviation of 0.4 degrees in each of the two axes orthogonal to the measured magnetic field. These are combined with the field model errors for a standard deviation of $\sigma_{\tilde{\nu}} = 0.0077$ rad. Recall by Eq. (4.11) that the parameters α_1 and α_2 correspond to $1/2$ of the total rotation about $\hat{\boldsymbol{\nu}}_1$ and $\hat{\boldsymbol{\nu}}_2$, respectively. The matrix $R_{\tilde{\nu}\tilde{\nu}}$ is formed as

$$R_{\tilde{\nu}\tilde{\nu}} = \sigma_{\tilde{\nu}}^{-1} I_{2\times 2}$$

For simplicity, the time correlation in the slowly varying geomagnetic field model error is not included in the filter, but it is included in the truth model that has been used to test the filter.

The process noise $\boldsymbol{w}_k$ represents a torque impulse impingent on the spacecraft over the sample period. It is related to physical phenomena. Solar radiation pressure, gravity-gradient torques, and atmospheric drag torques are the primary disturbance factors over the altitude range of the SIERRA subpayloads. The square-root information matrix $\bar{R}_{ww}$ is related to $\boldsymbol{w}_k$ by

$$E[\boldsymbol{w}_j \boldsymbol{w}_k] = \left(\bar{R}_{ww}^T \bar{R}_{ww}\right)^{-1} \delta_{j,k}$$

The matrix $\bar{R}_{ww}$ is assumed diagonal with identical elements, i.e.,

$$\bar{R}_{ww} = \sigma_w^{-1} I_{3\times 3}$$

The tuned value of σ_w is 10^{-4} N-m-s. This value has been selected based on the expected levels of the disturbance sources listed above.

The vector $\boldsymbol{p}_k$ models the error in the conversion from $\boldsymbol{h}_{sc}$ to $\boldsymbol{\omega}$ through the function $\boldsymbol{\omega}(\boldsymbol{h}_{sc})$. The statistics of the sequence $\boldsymbol{p}_k$ depend on the richness of the spacecraft's modal excitation. The approximations in $\boldsymbol{\omega}(\boldsymbol{h}_{sc})$ are more exact as the spacecraft motion more closely approximates pure nutation. For example, multi-modal excitation in a typical test case led to sinusoidal $\boldsymbol{\omega}(\boldsymbol{h}_{sc})$ errors with an amplitude of 0.1 rad/s, or 1% of the nominal 10 rad/s spin rate, whereas errors when the nutational mode acted alone were about 10 times smaller. A good model for the $\boldsymbol{p}_k$ sequence must take into account both the decay in non-nutational spacecraft modes (and the consequent decrease in the error $\boldsymbol{p}_k$) and the nominal intensity of $\boldsymbol{p}_k$ when in pure nutation. The equation governing the time dependence of $\bar{R}_{pp(k)}$ has been formulated as

$$\bar{R}_{pp(k)} = \sigma_{p(k)}^{-1} I_{3\times 3}, \quad \sigma_{p(k)} = \sigma_f + (\sigma_0 - \sigma_f) \exp\left(\frac{-t_k}{\tau}\right) \tag{4.26}$$

The parameter σ_0 reflects the magnitude of errors in $\boldsymbol{\omega}(\boldsymbol{h}_{sc})$ immediately following boom deployment, whereas σ_f represents errors after the stable boom articulation modes have decayed to zero. Selection of values for these parameters is guided by a comparison of truth-model data for $\boldsymbol{\omega}_k$ against the approximation $\boldsymbol{\omega}(\boldsymbol{h}_{sc(k)})$ under the type of post-deployment multi-modal excitation that might be expected. The time constant τ is chosen close to the decay time constants of significant non-nutational modes. The selected parameter values for the SIERRA subpayloads are

$$\sigma_0 = 0.4 \text{ rad/s}, \quad \sigma_f = 0.03 \text{ rad/s}, \quad \tau = 100 \text{ s}$$

The time correlation in the error in Eq. (4.14) is modeled using the one-step memory process whereby $\boldsymbol{p}_k$ and $\boldsymbol{p}_{k+1}$ both appear in the equation. A more exotic exponentially correlated process has also been tested, with unremarkable improvement. The one-step memory process was selected because it requires a minimal number of tuning parameters while capturing the bulk of the time correlation. The square-root information matrix $\bar{R}_{pp(k)}$ is related to $\boldsymbol{p}_k$ by

$$E[\boldsymbol{p}_k \boldsymbol{p}_k^T] = \left(\bar{R}_{pp(k)}^T \bar{R}_{pp(k)}\right)^{-1}$$

The diagonal elements of $R_{xx(0)}$ are chosen to be commensurate with expected errors in the initial state estimate $\hat{\boldsymbol{x}}_0$, and the off-diagonal elements are set to 0. The matrix $R_{pp(0)}$ is set equal to $\bar{R}_{pp(0)}$, whereas $R_{px(0)}$ is set to 0, reflecting the assumption that $\boldsymbol{p}_0$ and the errors in $\hat{\boldsymbol{x}}_0$ are uncorrelated.

Adjustments to the tuning values have been made to match the modeled covariances with filter performance. The sequence of residuals $\boldsymbol{\epsilon}_k$ in Eq. (4.25) is used as the performance metric in this process. In the absence of modeling errors, the sequence $\boldsymbol{\epsilon}_k$ is distributed as

$$E[\boldsymbol{\epsilon}_k] = 0, \quad E[\boldsymbol{\epsilon}_k \boldsymbol{\epsilon}_j^T] = I_{2\times 2}\delta_{k,j} \tag{4.27}$$

An average of $\|\boldsymbol{\epsilon}_k\|^2$ over K time steps may be written

$$\bar{\epsilon}_K = \frac{1}{K}\sum_{i=1}^{K} \|\boldsymbol{\epsilon}_i\|^2 \tag{4.28}$$

From this it may be noted that $K\bar{\epsilon}_K \sim \chi^2_{(2K)}$. The matrices $R_{xx(0)}$, $\bar{R}_{pp(k)}$, and $\bar{R}_{ww}$ have been tuned so that the weighted average $K\bar{\epsilon}_K$ is near the 95% confidence bounds of the $\chi^2_{(2K)}$ distribution. This process worked well when using simulated data but was less effective with empirical data where high frequency errors in the measurement were insignificant compared with the slowly varying magnetic field model errors. This resulted in smaller innovations than expected because the filter was able to fit the low-frequency noise better than the high-frequency noise model predicted. The final strategy adopted was to tune the filter using simulated data and then to vary only $R_{xx(0)}$ when tuning the filter to empirical data, choosing the $R_{xx(0)}$ that gave a good overall fit to the measurements while maintaining $\boldsymbol{h}_{in}$ fairly constant. The tuned values of $\bar{R}_{pp(k)}$ and $\bar{R}_{ww}$ are as noted above, while the tuned value of $R^{-1}_{xx(0)} = \text{diag}([1, 1, 1, 0.01, 0.01, 0.01])$. The magnitude of the angular momentum vector for each subpayload is more than 20 N-m-s. The three 1 values for the initial angular momentum component error standard deviations are less than 5% of this magnitude.

4.5 Results when the Filter and Smoother Operate on Simulated Data

4.5.1 Truth-Model Simulation

The truth-model simulator employs the dynamics model of [49], which governs the time evolution of the 23-element state vector $\boldsymbol{x}$ presented in Section 4.3. It models the spacecraft attitude and rate and the relative boom positions and rates. Runge-Kutta integration is used to solve for $\boldsymbol{x}(t_k)$. To validate the simulator output, the total system angular momentum was reconstructed for the zero-torque case. This was shown to be constant over 700 seconds of simulated data.

A realistic simulation of the sensor noise is important to truth-model testing of an estimation algorithm. Errors in magnetometer measurements are of two categories: sensor errors and magnetic field model errors. Sensor errors relating to non-orthogonality, scale factor errors, and biases are not included in the simulator output. It is assumed that these errors are removed by calibration during the data preparation process. It is further assumed that magnetometer mounting misalignment is calibrated prior to launch. The remaining sensor errors are non-deterministic thermal noise and quantization noise. These can be lumped together and modeled as a discrete-time zero-mean white Gaussian process. It is important to consider the sampling interval when selecting the value of the process variance, since more closely spaced samples are less likely to be uncorrelated. This effect can be modeled loosely by increasing the variance of the uncorrelated noise added to simulate the measurement. The sampling rate of the magnetometer measurements produced by the simulator was set at 120 Hz to match the sampling rate of the SIERRA magnetometers. The magnetometer sampling rate must be at least twice the

angular frequency of the rotating spacecraft to avoid aliasing. Higher sampling rates generally improve the performance of the estimator as long as the increased correlation in the noise from one measurement to the next is accounted for in the measurement model.

For the current simulator, a zero-mean uncorrelated error angle with a standard deviation of 0.57 degrees is added to each magnetometer measurement to simulate thermal and quantization noise within the magnetometer. Comparison with SIERRA flight data has shown this to be a pessimistic estimate of high-frequency noise, but it has been adopted so that the simulation cases will be demanding. Time-tagging errors in the magnetometer measurements for the SIERRA subpayloads were not modeled as these are a negligible fraction of the sampling interval.

To simulate magnetic field model errors, which include errors in spacecraft position knowledge within the geomagnetic field, a 10th-order, year 2000 International Geomagnetic Reference Field (IGRF) is used as the truth model, whereas a 7th-order 1995 IGRF model is used in the filter/smoother. This strategy captures the time correlation inherent in the magnetic field model errors. The field is calculated at the Earth-relative positions of the SIERRA flight trajectory. Hence, the simulated magnetic field movement reflects the actual 13.6 degree rotation of the true magnetic field during the data collection period of the SIERRA mission.

4.5.2 Representative Results

A 700 second data segment was created using the SIERRA simulator under the following conditions:

- Initial spacecraft angular rate $\boldsymbol{\omega_0}$ = 10.14 rad/s.
- Initial nutation angle = 1.8 deg., final nutation angle = 10.4 deg.
- Initial angle between $\boldsymbol{h}_{in}$ and $\boldsymbol{b}_{in}$ = 34 deg. This angle is related to the sensitivity of the attitude estimate to errors in the estimate of $\boldsymbol{h}_{in}$. Maximal (minimal) sensitivity occurs for $\boldsymbol{h}_{in}$ and $\boldsymbol{b}_{in}$ aligned (orthogonal). Although the actual SIERRA subpayloads enjoy a robust 87 and 97 degrees separation, a narrower angle was chosen in simulation to represent a less ideal situation.
- Total angular rotation of $\boldsymbol{b}_{in}$ = 13.6 deg.
- Error in initial estimate of attitude parameter θ = 5.7 deg.
- The error in the initial $\boldsymbol{h}_{in}$ estimate consists of 3 equal components: one in the $\{\boldsymbol{h}_{in}, \boldsymbol{b}_{in}\}$ plane and perpendicular to $\boldsymbol{h}_{in}$, one orthogonal to the plane, and one along $\boldsymbol{h}_{in}$. The magnitude of each error component is 5% of the magnitude of $\boldsymbol{h}_{in(0)}$. These lead to an initial $\boldsymbol{h}_{in(0)}$ estimate 4 degrees from the true angular momentum.

Estimation results for the filter and smoother using simulated data are presented in Figs. 4.4-4.6. Figure 4.4 displays the total error angle in the attitude estimates produced by the filter and the smoother over a 700-second run. The effect of the non-nutational modes is evident in the first 300 seconds where the attitude estimation errors undergo larger excursions than during the remaining 400 seconds. The smoothed total attitude error angle remains below 4 degrees throughout the run. It drops below 2 degrees as multi-modal motion gives way to pure nutation, causing approximations within the estimator to become more accurate.

Figure 4.5 presents the errors in the smoothed estimates of the boom articulation angles ϕ_1 and γ_1. These are representative of the errors in all 4 booms. Errors in the out-of-plane angle ϕ_1 fall below 0.5 degrees after non-nutational modes die out, validating the assumption that the booms lie approximately perpendicular to the angular

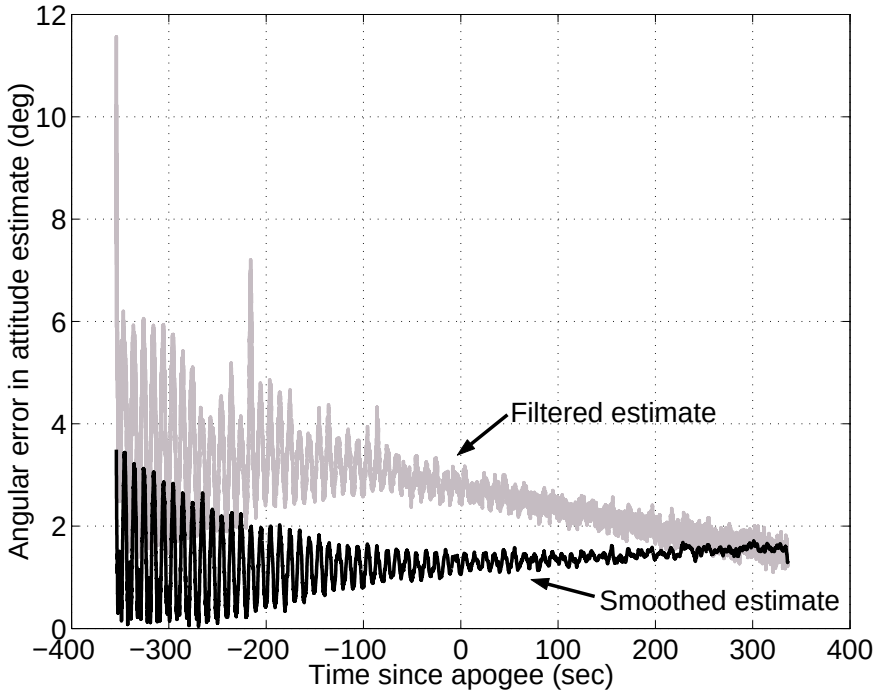

Figure 4.4: Filtered and smoothed total attitude error angle for a 700 second run using simulated data.

momentum vector during pure nutation. Errors in the in-plane boom angle γ_1 reflect the deviation from the assumed value of zero. These errors increase as the spacecraft nutation angle grows. Analysis shows that this instability of the in-plane boom angles is due to the boom attachment points being slightly displaced along the z-direction from the system center of mass. As the spacecraft nutates, the in-plane motion of the booms' base attachment points produces a periodic in-plane forcing which acts to increase the in-plane boom articulation angles γ_i. For nutation angles below 15 degrees, the in-plane boom deflection remains below 1 degree.

The filtered and smoothed estimates of the inertial angular momentum components are compared with the true component values in Fig. 4.6. The z-component of $\hat{\boldsymbol{h}}_{in}$ contains less error than the x and y components. This is because $\boldsymbol{h}_{in}$ is nearly aligned along the reference z-axis, so that corrections to the magnitude of $\hat{\boldsymbol{h}}_{in}$ are reflected in

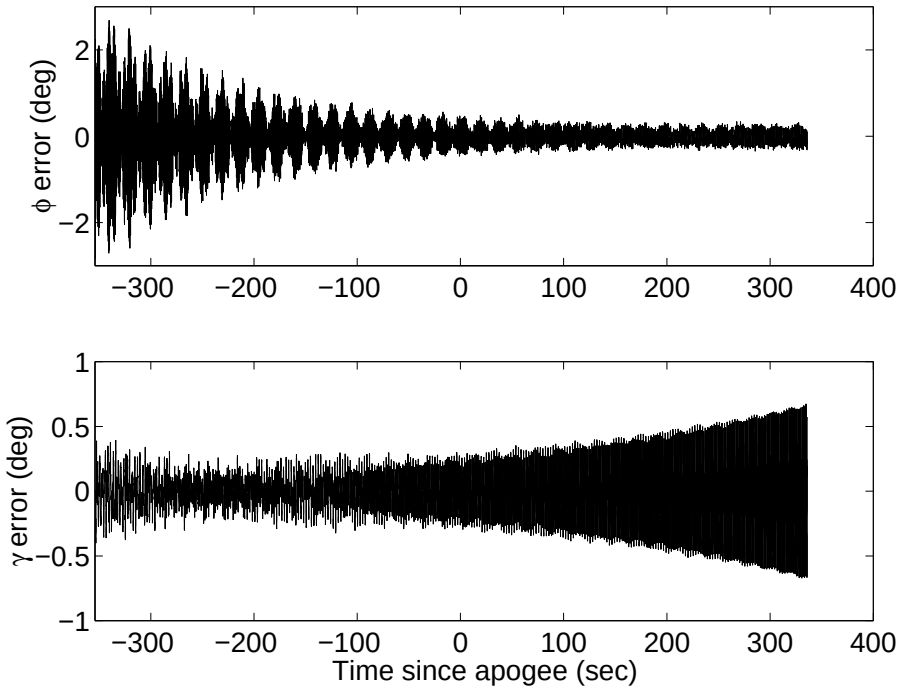

Figure 4.5: Errors in the smoothed estimates of the angles ϕ_1 and γ_1 for a 700 second run using simulated data (representative of errors in all 4 booms).

the z-component of $\hat{\boldsymbol{h}}_{in}$. As has been mentioned, the magnitude of $\boldsymbol{h}_{in}$ is a strongly observable quantity, which is why the filter is able to correct the z-component of $\hat{\boldsymbol{h}}_{in}$ almost immediately. The large initial x- and y-component corrections in Fig. 4.6 are along the other most observable direction, which is in the $\{\boldsymbol{h}_{in}, \boldsymbol{b}_{in}\}$ plane. The key to the remaining gradual improvement in the filtered angular momentum estimate is the movement of $\boldsymbol{b}_{in}$ in inertial space. Additional information about $\boldsymbol{h}_{in}$ is revealed as $\boldsymbol{b}_{in}$ changes its direction. Since knowledge of $\boldsymbol{h}_{in}$ is linked to attitude knowledge, the attitude estimate is also refined.

Herein lies the significance of including $\boldsymbol{h}_{in}$ directly as an element of the state. Under the conditions of weak observability brought on by using only a magnetometer and by the small 13.6 degree rotation of $\boldsymbol{b}_{in}$, incremental information gathered about $\boldsymbol{h}_{in}$ must be closely guarded. It was found that a more traditional estimator state, where $\boldsymbol{\omega}$ describes

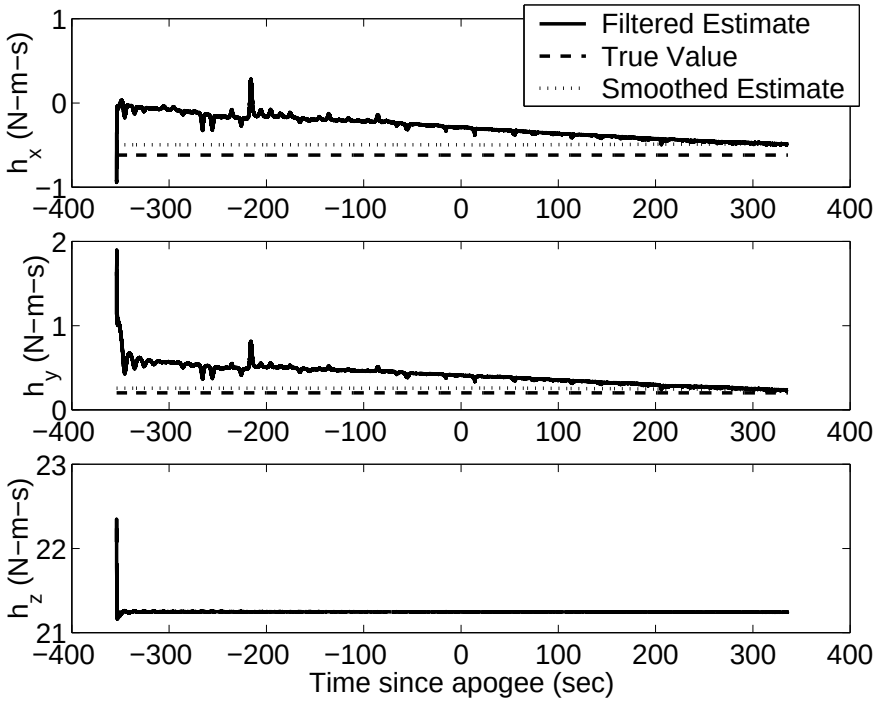

Figure 4.6: Filtered and smoothed estimates of $\boldsymbol{h}_{in}$ components compared with values from the truth-model simulation for a 700 second run using simulated data.

rate, allows errors in the $\boldsymbol{\omega}(\boldsymbol{h}_{sc})$ conversion to creep into the angular momentum, making a reconstruction of $\boldsymbol{h}_{in}$ wander in inertial space, contrary to conservation of angular momentum. This drives the spacecraft attitude estimate into divergence.

One may easily contrast a filter dynamics model based on a state vector that includes $\boldsymbol{\omega}$ and one based on a state vector that instead includes $\boldsymbol{h}_{in}$ for the SIERRA estimation problem. One way to do this is to provide each dynamics model with an error-free initial state and propagate this state forward without measurement updates. These open-loop estimates are then compared to the output of the SIERRA truth-model simulator primed with the same initial state.

The significant deficiencies in both the $\boldsymbol{\omega}$- and $\boldsymbol{h}_{in}$-based dynamics models are due to errors in the relation $\boldsymbol{\omega}(\boldsymbol{h}_{sc})$. These errors arise because the underpinning assump-

tions of Eqs. (4.2) and (4.3) are inexact–especially for subpayload motion that includes modes other than pure nutation. A comparison of the propagation accuracy of these two models has been carried out using the initial conditions described at the beginning of this subsection. These initial conditions lead to subpayload motion that is not purely nutational. It was found that the open-loop state estimate produced by the $\boldsymbol{\omega}$-based model diverged within 10 seconds. In contrast, the $\boldsymbol{h}_{in}$-based model produced open-loop attitude estimates which strayed only 16 degrees from the truth-model attitude after 100 seconds of propagation. Thus, the use of the inertial angular momentum components as states of the SIERRA filter improves the filter's accuracy by decreasing its dynamics propagation errors.

In any Euler-based estimation scheme, there will exist small errors in the relationship between $\boldsymbol{\omega}$ and $\boldsymbol{h}_{sc}$ owing to factors such as uncertainty in the inertia matrix or in the motion of flexible appendages. Under conditions of strong attitude observability, these errors are corrected soon after they arise, meaning that an unforced $\boldsymbol{h}_{in}$ remains fixed in inertial space. In these cases, a traditional state vector employing $\boldsymbol{\omega}$ is adequate. Under weak observability, however, use of $\boldsymbol{h}_{in}$ is preferred. The trivial propagation of Eq. (4.13) isolates the estimate of $\boldsymbol{h}_{in}$ from errors in $\boldsymbol{\omega}(\boldsymbol{h}_{sc})$.

4.6 Filter and Smoother Results for SIERRA Flight Data

4.6.1 Data Preparation

Several data pre-processing tasks were carried out before applying the new estimation algorithm to the SIERRA flight data. The raw 1 kHz magnetometer measurements from the TAMs onboard the SIERRA subpayloads were interpolated and undersampled

at 120 Hz. The data was further processed to remove the effects of magnetometer non-orthogonality, scale factor errors, and biases. Obvious measurement outliers were also removed. Biases in the inertial sensors onboard the primary SIERRA payload were calibrated post-launch using magnetic field data. Rate measurements from these inertial sensors were used to calculate an initial estimate of $\boldsymbol{h}_{in}$ for each subpayload at separation. This estimate is denoted by $\hat{\boldsymbol{h}}_{in(0)}$.

The remaining estimator state elements, $\alpha_{1,2}$ and θ, were initialized as follows: Elements $\alpha_{1,2}$ assumed their *a priori* value of 0. Rotation θ was chosen such that initial transients in the estimate of $\boldsymbol{h}_{in}$ were as smooth as possible. This is equivalent to the hypothesis testing approach used in [56], where selection of the initial θ is driven by the size of the resulting innovations process.

The size of the error in $\hat{\boldsymbol{h}}_{in(0)}$ may be inferred from the corrections applied to $\hat{\boldsymbol{h}}_{in(0)}$ by the filter and the smoother. For the fore subpayload, the direction of the smoothed estimate of $\boldsymbol{h}_{in}$ differs from that of the initial estimate by 3.35 degrees. The discrepancy for the aft subpayload is more severe: 10.5 degrees. This implies that aft results may be less accurate.

4.6.2 Results

Filter and smoother results using telemetered data from the fore subpayload are presented in Figs. 4.7- 4.9. Figure 4.7 shows that the angular momentum estimate remains relatively constant over the data capture interval. Thus, the initial angular momentum estimate agrees well with the 700 seconds of magnetometer data. In Fig. 4.8, the root-sum-square sequence of the half angles α_1 and α_2 is plotted for the smoother. These are similar to filter innovations, giving a measure of how well the smoother fits the magne-

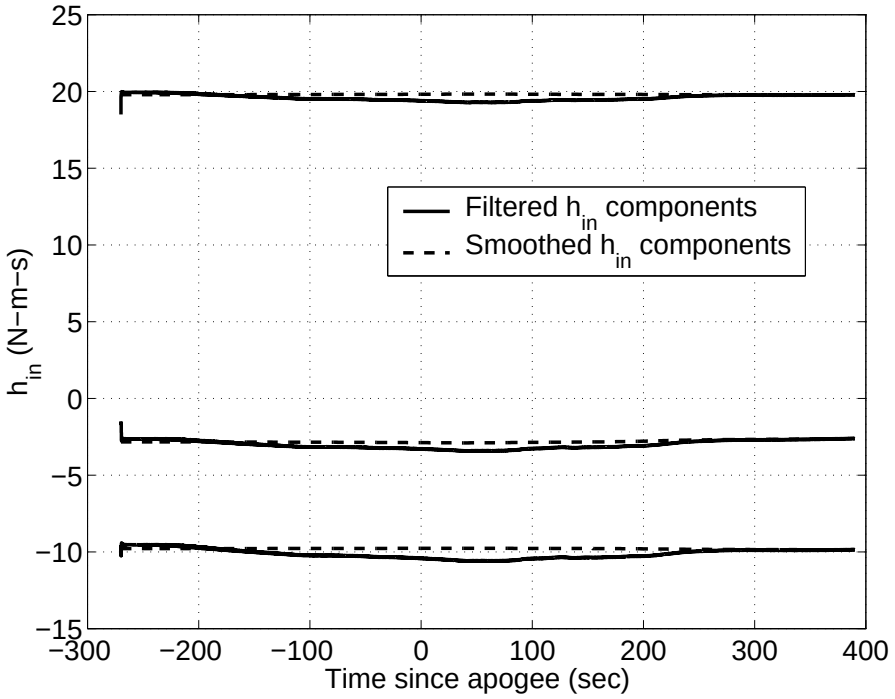

Figure 4.7: Components of the filtered and smoothed estimates of $\boldsymbol{h}_{in}$ using data from the SIERRA fore subpayload.

tometer data. Their small size, corresponding to a root-sum-square magnetometer error angle less than 1.2 degrees, indicates a close fit to the data. Closer inspection reveals strong time correlation among the innovations. This correlation is probably an artifact of the time-correlated errors in the spacecraft dynamics model and in the magnetic field model errors. Further error modeling might reduce correlation in the innovations sequence, but this was not considered necessary given the satisfactory estimator performance.

In Fig. 4.9 the smoothed estimate of the out-of-plane boom angle ϕ_1 is presented as representative of estimates for all four booms. Its profile shows the effect of the increasing nutation angle on out-of-plane boom displacement.

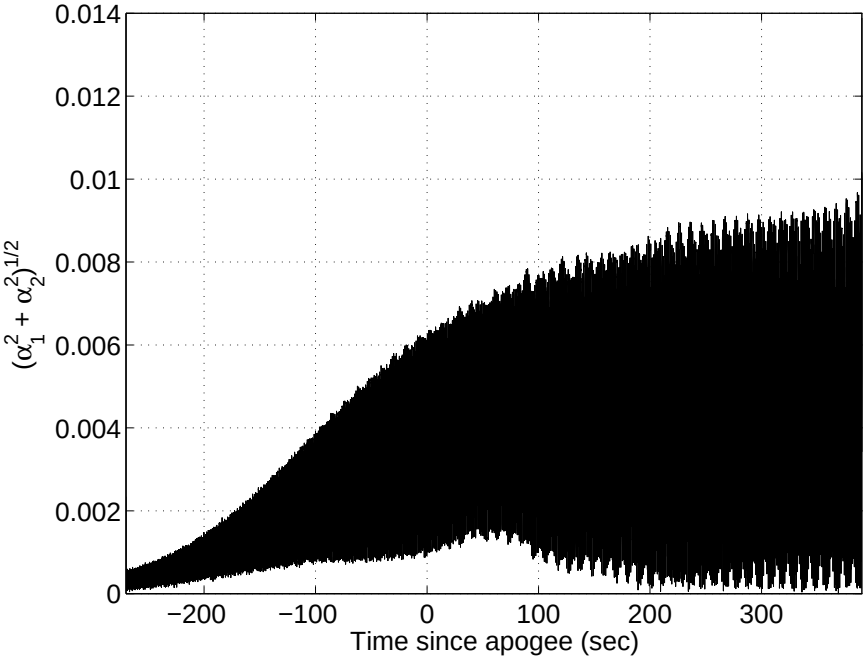

Figure 4.8: Root-sum-square of the residual measurement error sequence for the smoother applied to flight data.

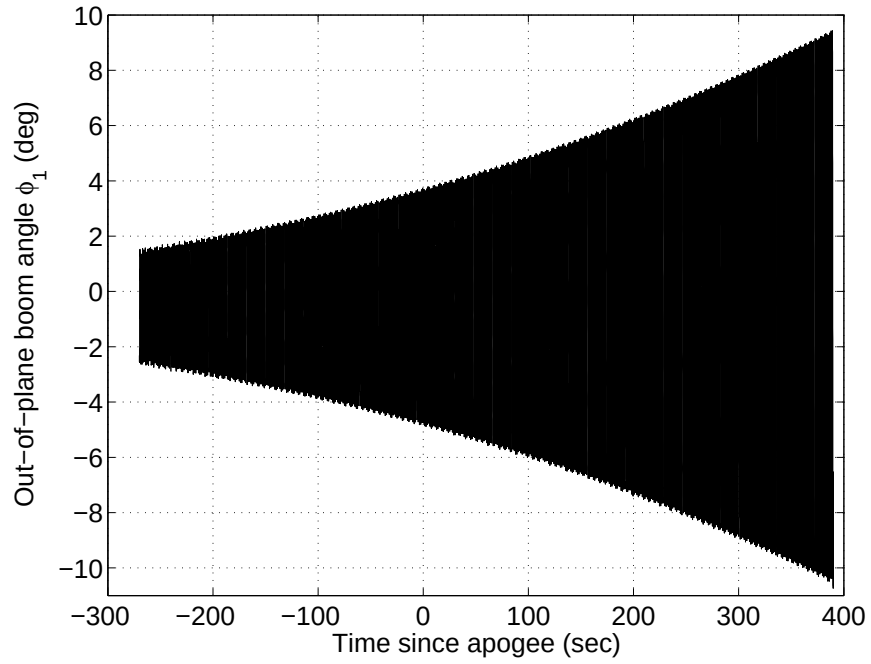

Figure 4.9: Smoothed estimate of the out-of-plane boom angle ϕ_1 for the SIERRA fore subpayload (representative of all ϕ_i).

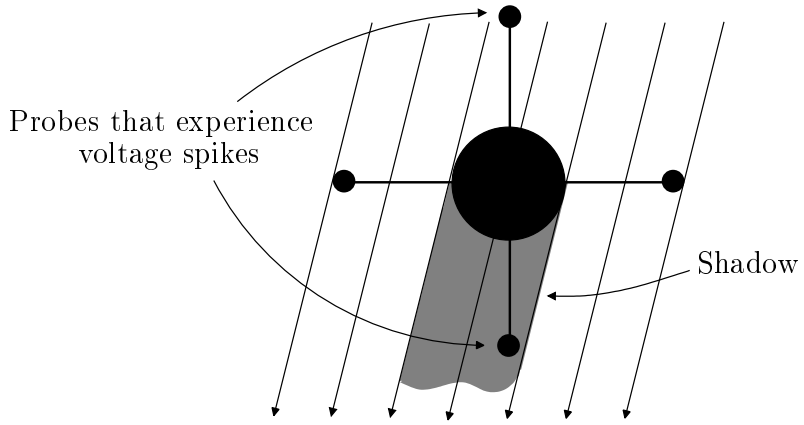

Figure 4.10: The plasma shadowing effect.

4.6.3 An Independent Check

An independent measure of estimator performance may be formulated from natural ionospheric phenomena. The booms of the SIERRA subpayloads were set up to make electric field measurements between opposite probes. The electric field sensed by the wire probes is the sum of two components. One is an induced electric field $\boldsymbol{E}_{v\times b} = \boldsymbol{v} \times \boldsymbol{b}$ generated by the spacecraft moving in the magnetic field. The other is the ambient electric field present in the ionosphere. For both sources, the electric field is null in the direction of the magnetic field. This is evident for the first source from the cross product operation. For the ambient field, it is a consequence of the high plasma conductivity along magnetic field lines. In practice, however, when opposite booms are aligned along the magnetic field, the body of the spacecraft blocks plasma movement from the region of one probe to the other. This gives rise to a difference in plasma population, and hence a voltage potential, between the probes. This plasma "shadowing" effect manifests itself in voltage spikes in the electric potential measurements. The situation is illustrated in Fig. 4.10.

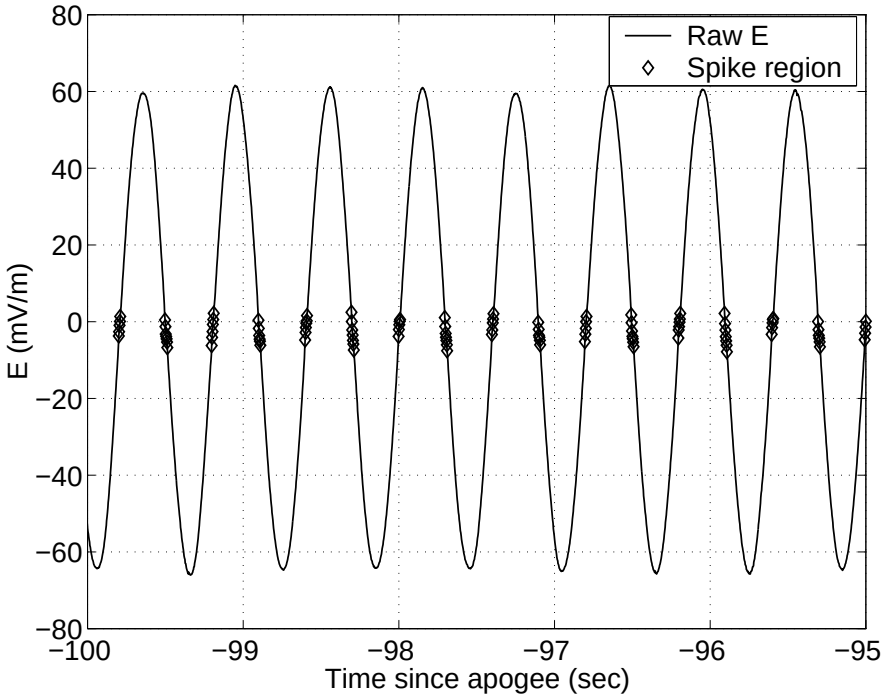

Figure 4.11: Electric field measurements between opposite probes of the aft SIERRA subpayload.

If performing properly, the present estimator should be able to predict boom alignments with the magnetic field, and thereby predict the occurrence of the voltage spikes. This test was carried out, and the estimator was able to accurately predict the voltage spikes. Results for the aft payload are presented in Fig. 4.11. The marked regions of Fig. 4.11 are those where predictions of boom and magnetic field alignment to within 5 degrees coincide with the small voltage spikes resulting from the plasma shadowing effect. This coincidence provides an independent verification of the boom angle estimates.

It should be noted that the voltage spikes can also be predicted, though less successfully, using only magnetometer data while assuming boom angles $\phi_i = \gamma_i = 0$. The added predictive accuracy of the estimator suggests that estimates of boom angles are fairly accurate.

4.7 Broadened Scope of Application of the Estimation Algorithms

Modeling errors, time varying and otherwise, are common to the general problem of Euler-based spacecraft attitude estimation. When they are significant, errors can quickly accumulate to the point of destabilizing an estimator that has weak state observability. The present estimator is designed to accommodate time-varying model uncertainty and weak state observability. It does this by directly including $\boldsymbol{h}_{in}$ in the estimator state and by allowing random error in the relationship between $\boldsymbol{\omega}$ and $\boldsymbol{h}_{sc}$. This technique is useful for spacecraft with modest attitude knowledge requirements where flexible appendages, uncertain inertia parameters, or both, could foul a traditional Euler-based Kalman filter. It is also useful as a backup estimator should sensors (e.g. gyros) fail, and Euler-based estimation become a last resort.

4.8 Conclusions

A magnetometer-based attitude estimation filter and smoother have been developed for a spinning spacecraft with wire booms. The new estimator overcomes two principal challenges: significant time-varying modeling errors and weak state observability. This is done by including the inertially-referenced angular momentum vector directly as a state element and by expressly accounting for modeling errors within the spacecraft kinematics. These random modeling errors enter the algebraic relationship whereby the spacecraft-referenced angular velocity is determined as a function of the spacecraft-referenced angular momentum. An additional feature of the estimator is that an approximation has been used for this relationship, one that is useful when the spacecraft is undergoing its principal mode of motion–an unstable flexible-body nutation.

The estimator is initialized with an estimate of the system angular momentum and thereafter uses magnetic field measurements to accurately estimate the spacecraft attitude, the angular momentum, and the relative positions of the wire booms. Testing has been carried out using a full-order nonlinear truth model. Under realistic error and noise conditions, the estimator converged to within 2 degrees of the true spacecraft attitude. Relative boom orientation estimates remained within 1 degree of the true orientations.

The estimator has also been tested using flight data telemetered from the subpayloads of a recent sounding rocket mission. In this case, the estimator for each subpayload is initialized with an angular momentum estimate based on measurements from inertial sensors onboard the primary payload taken immediately before the deployment of each subpayload. Measurement residuals from the estimator indicate that it is able to fit the subpayloads' magnetometer measurements to within 1.2 degrees. An independent test of the estimator performance using electric field measurements has demonstrated the estimator's ability to accurately predict relative boom positions. The estimator is recommended for use on spacecraft whose Euler dynamics models contain significant uncertainties due to parameter errors or due to the approximate treatment of flexible-body dynamics effects.

Chapter 5

The Semidiurnal Variation in GPS-derived Zenith Neutral Delay

T. E. Humphreys, M. C. Kelley, N. Huber, and P. M. Kintner, "The semidiurnal variation in GPS-derived zenith neutral delay," *Geophysical Research Letters*, vol. 32, pp. 24 801–+, Dec. 2005.

5.1 Abstract

Zenith neutral delay (ZND) estimates derived from ground-based GPS receivers exhibit variations at harmonics of the solar day. The aim of this work is to characterize the semidiurnal (S_2) variation and determine its probable origin. Data from 100 GPS sites are compared with surface pressure measurements to reveal close agreement between the estimated ZND S_2 variation and the S_2 surface pressure tide. Error analysis suggests that the S_2 variation in ZND estimates is not due primarily to orbit, solid earth, or Earth orientation modeling errors. Atmospheric loading and mapping function errors are each expected to contribute less than 11% to the estimated ZND S_2 amplitude. Local incongruities reflect the influence of water vapor or site-dependent errors.

5.2 Introduction

Since 1998 the International GPS Service (IGS) has included an estimated zenith neutral delay (ZND) (sometimes called tropospheric delay) among its official products. The

ZND measures the amount by which the neutral atmosphere delays a GPS signal in excess of the free-space delay. ZND is conventionally measured in meters, with a nominal value of 2.4 m at sea level. Current ZND accuracy is about 4 mm [60].

Spectral analysis of IGS ZND data reveals mm-level variations at harmonics of the solar day and at the lunar tidal frequency. An obvious explanation is that these variations reflect the regular tides induced on the atmosphere by solar and lunar thermal and gravitational excitation. Indeed, Dai et al. [61] showed that a solar diurnal (S_1) variation in the wet component of GPS-derived ZND agrees roughly with that in microwave radiometer (MWR) and radiosonde measurements. However, Humphreys et al. [62] showed that the amplitude of the lunar tide in IGS ZND data prior to 2000 is drastically reduced in post-2000 data, and that high-frequency solar harmonics extend well beyond S_6, contrary to the behavior of the surface pressure tides. Such results encourage careful scrutiny of the periodic variations in IGS ZND data if these are to be accepted as manifestations of actual atmospheric tides. Moreover, a close examination of the variations in GPS-derived ZND will be useful for detecting persistent periodic errors in the ZND record.

The S_2 variation in IGS ZND data will be the focus of this study. The approach taken will be to compare its global phase and amplitude distribution with that of the semidiurnal surface pressure tide, $S_2(p)$. With long wavelengths excited by ozone and water vapor absorption of solar radiation, the 12-hour $S_2(p)$ tide is characterized by a strong, zonally homogeneous surface pressure variation with tidal maximum occurring about 2 hours before local noon and midnight [63–65]. A strong correlation between the global distribution of the two signals will provide evidence for the authenticity of the S_2 variation in IGS ZND estimates. Precision and likely errors will also be considered.

5.3 Models, Data, and Analysis Technique

ZND is the integrated refractivity along a vertical path through the neutral atmosphere:

$$\tau^z = ct^z = 10^{-6} \int_0^\infty N(z)dz \tag{5.1}$$

where τ^z is ZND measured in units of distance, c is the speed of light in a vacuum, and t^z is the delay measured in units of time. Neutral atmosphere refractivity N is approximately related to the total mass density of moist air ρ (kg m^{-3}), temperature T (K), and partial pressure of water vapor e (mb) by the relation [66]

$$N = 222.76\rho + (17 \pm 10)\frac{e}{T}Z_w^{-1} + 377600\frac{e}{T^2}Z_w^{-1} \tag{5.2}$$

Here, Z_w is a factor near unity that accounts for the small departure of moist air from an ideal gas. The integral of the first term in Eq. (5.2) is designated the hydrostatic component, τ_h^z; the integral of the remaining two terms is the wet component, τ_w^z. Thus $\tau^z = \tau_h^z + \tau_w^z$.

The hydrostatic component dominates τ^z, accounting for roughly 90% of the total delay. It follows that τ^z is strongly correlated with surface pressure p_0. Disregarding the change in the acceleration of gravity g with height, the hydrostatic approximation $dp = -g\rho\, dz$ relates τ_h^z to p_0 by $\tau_h^z = (2.28\ \text{mm/mb})p_0$. Davis et al. [66] note that this scale factor varies less than 1% under extreme weather conditions. Assuming a typical 1-mb semidiurnal surface pressure tide $S_2(p)$, this scale factor predicts a semidiurnal ZND variation $S_2(\tau^z)$ with an amplitude of 2.28 mm. Thus, it is unsurprising to note variations in IGS ZND data at frequencies corresponding to the atmospheric tides (Fig. 5.1, left panel). Peaks at S_1 to S_6 are visible as well as a peak at the lunar tidal frequency, L_2 (nearly coincident with S_2). This paper will focus only on S_2, which, as observed in the IGS ZND data, will be denoted $S_2(\tilde{\tau}^z)$ to distinguish it from the error-free $S_2(\tau^z)$

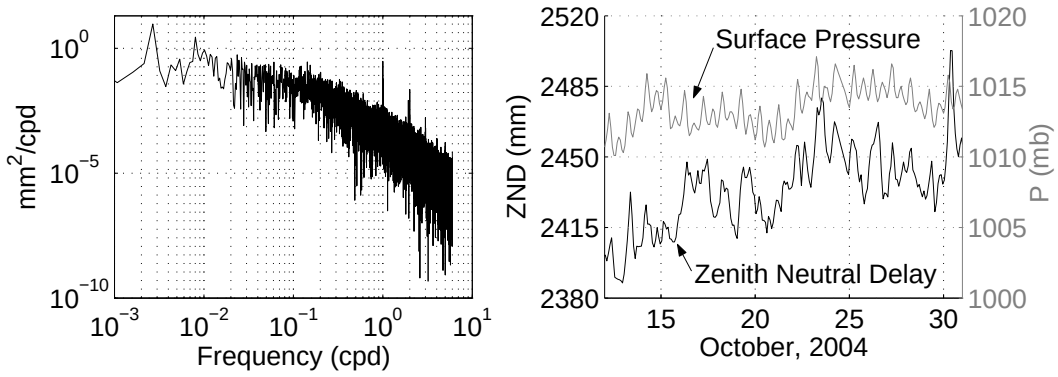

Figure 5.1: Left panel: Power spectrum of ZND data taken from IGS station BAHR (50.6°E, 26.2°N) for 2000-2005. Abscissa units are cycles per day (cpd). Spectral peaks are visible at harmonics of the solar day and at the lunar tidal frequency. Right panel: Time history of ZND and surface pressure measurements from BAHR. Diurnal and semidiurnal variations are evident in both plots.

variation. This is done to concede the possibility that the observed variations in IGS ZND data are due to causes other than actual tides in τ^z.

Though small on average, the wet component is highly variable, contributing to τ^z significant dynamics that are not present in surface pressure. This explains some of the irregularity of the IGS ZND data relative to surface pressure (Fig. 5.1, right panel). The effect of water vapor dynamics on $S_2(\tau^z)$ has not been well established. Dai et al. [61] detected a ~0.1-mm semidiurnal variation in GPS-derived precipitable water vapor (PWV) estimates over North America, amounting to a ~0.7-mm semidiurnal variation in τ^z_w—comparable in amplitude to the semidiurnal variation in τ^z_h. On the basis of this estimate, one would expect τ^z_w to significantly influence the response of τ^z to S_2 forcing. But whereas Dai et al. [61] conclusively demonstrated a large diurnal variation in PWV, the reported semidiurnal variation is much smaller than the rms errors for GPS-derived PWV and was not visible in independent radiosonde and MWR measurements. As will be shown subsequently, the irregularities in $S_2(\tilde{\tau}^z)$ at some IGS sites are consistent with the hypothesis that there exist significant local semidiurnal signals in τ^z_w. However, in

general, the $S_2(\tilde{\tau}^z)$ variation is well predicted by its hydrostatic component alone.

This study analyzes the new IGS ZND product, available at

ftp : //cddis.gsfc.nasa.gov/gps/products/trop_new

for the interval October 2000 to June 2005 and for 100 sites distributed globally as indicated by the dots in Figs. 5.2 and 5.3. The new IGS ZND product is based on the precise point positioning technique. It has a higher sampling rate and lower formal errors than the legacy IGS ZND product [60]. Most (79) of the sites are Reference Frame sites, which are subject to strict standards of data quality and continuity. Gaps are common in the data, but at least 2 years of ZND estimates are available for each site. The IGS data are downsampled from 5- to 15-min intervals and the harmonic coefficients a_2 and b_2 of the oscillation at the S_2 frequency are estimated by least squares from the ZND time series for each site. These are used to calculate the mean amplitude A_2 and phase σ_2 of $S_2(\tilde{\tau}^z)$ over the data interval:

$$S_2(\tilde{\tau}^z) = A_2 \sin(2t' + \sigma_2) = a_2 \cos 2t' + b_2 \sin 2t' \tag{5.3}$$

Here, t' is local mean solar time (LST) in degrees. Zonal harmonic analysis of the harmonic coefficients follows the procedure outlined in [67]. First, a_2 and b_2 are interpolated onto a regularly-spaced 5° lat by 10° long grid. Next, the gridded coefficients around each line of latitude θ_i are expanded using a trigonometric series of the longitude λ. This yields a decomposition of S_2 into wave components $S_2(t, \theta_i) = \sum_{s=-\infty}^{\infty} S_2^s(t, \theta_i)$, where s is wave number and t is Universal Time. Predominant among the wave components is the migrating tide S_2^2, which moves westward at the speed of the mean Sun. All zonal wave components with wave numbers $s \neq 2$ are termed nonmigrating wave components; $s = 0$ is a standing wave; wave numbers $s < 0$ move eastward.

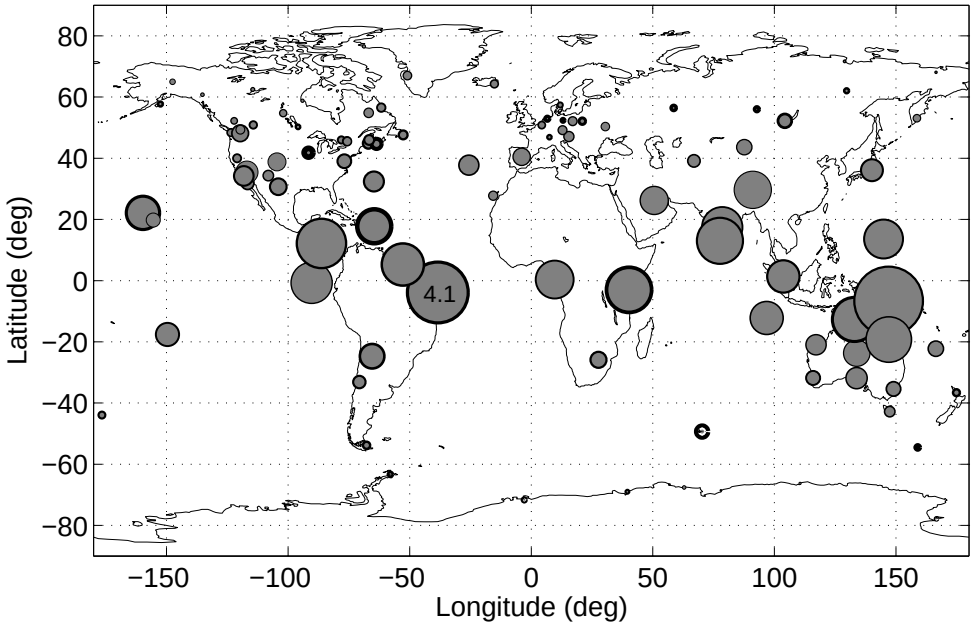

Figure 5.2: Global distribution of annual mean $S_2(\tilde{\tau}^z)$ amplitude. The amplitude at IGS site FORT (4.1 mm) is labeled for scale. The dark annulus about each dot gives a measure of the $S_2(\tilde{\tau}^z)$ signal-to-noise (SNR) ratio at that site (see AM for details). At SNR = 1, the dark annulus completely covers the gray dot.

5.4 Observations

Results of the global analysis of $S_2(\tilde{\tau}^z)$ are presented in Figs. 5.2 and 5.3. These may be compared with similar plots for $S_2(p)$ reported in [67], [64], and [65]. The data underlying Figs. 5.2 and 5.3 are available in tabular format in the auxiliary material (AM). Auxiliary material is available from ftp://ftp.agu.org/apend/gl/2005GL024207.

The large-scale features of the $S_2(\tilde{\tau}^z)$ amplitude distribution, which forgive deficiencies in the spatial resolution of the 100 sites used, correlate well with large-scale features of $S_2(p)$; namely, $S_2(p)$'s characteristic zonal homogeneity and its amplitude increase toward the equator. A comparison of the latitudinal distribution of $S_2(\tilde{\tau}^z)$'s and $S_2(p)$'s migrating components is presented in the AM, leading to an estimated $S_2^2(\tilde{\tau}^z)/S_2^2(p)$

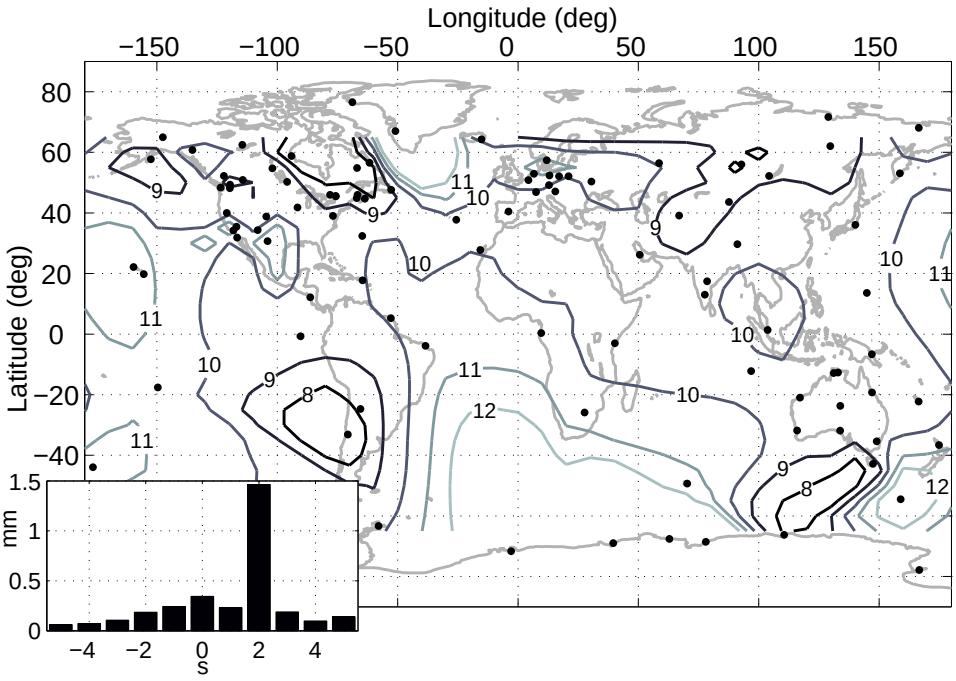

Figure 5.3: Annual mean $S_2(\tilde{\tau}^z)$ phase isolines. Phase is expressed as local mean solar time at first tidal maximum. Accuracy of the isolines is limited by the sparse spatial resolution of the sites used (black dots). Inset: Global average $S_2(\tilde{\tau}^z)$ wave components.

scale factor of 1.9 mm mb^{-1}—near the scale factor predicted by the hydrostatic approximation. This suggests that, on average, $S_2(\tilde{\tau}^z)$ is dominated by its hydrostatic component.

The $S_2(\tilde{\tau}^z)$ phase distribution exhibits a predominant phase near 150°, corresponding to tidal maximum at 1000 LST. This is consistent with the global average phase for $S_2(p)$, which is 158° (0940 LST). The phase of $S_2(\tilde{\tau}^z)$ is more irregular at middle and low latitudes than that of $S_2(p)$ (irregularity at high latitudes is expected—a result of the increasing dominance of the S_2^0 standing wave toward the poles). This is due in part to systematic errors in ZND and to the short ZND data record, but may also indicate wet component influences on $S_2(\tilde{\tau}^z)$.

The global mean wave components of $S_2(\tilde{\tau}^z)$ (inset of Fig. 5.3) agree closely with surface pressure data. The migrating wave component, S_2^2, predominates as expected for the S_2 tide. The next largest contribution for both data sources is the standing wave, S_2^0. As a consequence of amplitude and phase irregularities, the non-migrating wave components are more pronounced in the ZND data than in the surface pressure field [e.g., $S_2^2(\tilde{\tau}^z)/S_2^0(\tilde{\tau}^z) \simeq 4$ vs. $S_2^2(p)/S_2^0(p) \simeq 10$].

5.5 Error Analysis and Discussion

The results of the previous section are encouraging insofar as they suggest that $S_2(\tilde{\tau}^z)$ behaves generally as expected: it is dominated by its hydrostatic component. The 'fingerprint' of the hydrostatic tide in the amplitude and phase data (most striking in the wave component analysis) makes it unlikely that $S_2(\tilde{\tau}^z)$ is caused primarily by variations in EOP, ocean tide loading, or solid earth tides. Each of these has its own unique global phase and amplitude fingerprint, different from that of the $S_2(\tilde{\tau}^z)$ and $S_2(p)$ tides. (For example, the anelastic response of the solid Earth to the solar tide potential causes the maximum solid-earth deformation to occur after local noon, in contrast to the phase shown in Fig. 5.3.) Similarly, it is unlikely that errors in the final IGS orbit estimates couple into the ZND estimates in such a way as to closely replicate the hydrostatic tide (except in the case of atmospheric pressure loading, which will be discussed subsequently). Nonetheless, incongruities between the global distributions of $S_2(\tilde{\tau}^z)$ and $S_2(p)$ warrant closer examination. It is the purpose of this section to further assess the validity of $S_2(\tilde{\tau}^z)$ by examining its precision and considering likely sources of error.

A tidal determination's precision is calculated by dividing the data record into smaller subrecords that are assumed to be stochastically independent. The mean ampli-

tude and phase of these samples are considered significant if the mean tidal amplitude is at least 3 times greater than the semi-major axis of its 1σ error ellipse [63]. To assess $S_2(\tilde{\tau}^z)$ precision, 13 sites with nearly continuous data records from 2000 to 2005 were chosen for statistical analysis. Of these sites, 9 were equipped with a meteorological (MET) package providing surface pressure measurements, enabling a site-by-site comparison of $S_2(\tilde{\tau}^z)$ and $S_2(p)$ (MET data for site MKEA were taken from the MET package of a nearby telescope). The ZND and surface pressure records are divided into 4 one-year subrecords, each beginning on the same day of the year. From these, a four-sample amplitude and phase standard deviation is computed. The entire 5-year interval is used to evaluate the mean amplitude and phase. Results are reported in Table 5.1. All the determinations of $S_2(\tilde{\tau}^z)$ are significant except for those corresponding to sites YELL and ALGO, whose high latitudes explain the difficulty in the determination. All the determinations of $S_2(p)$ from MET data are significant. In all comparable cases, the precision of the MET determination is superior to that of ZND. Possible sources of random errors in $S_2(\tilde{\tau}^z)$ are phase range measurement errors and random fluctuations in τ_w^z.

Two features of Table 5.1 invite further attention. First, phase estimates for sites JPLM, MDO1, KOKB, and MKEA are low compared with MET data. Their phases correspond to tidal maxima at about local solar noon. In each case the good phase precision makes it unlikely that random instrument or meteorological noise is to blame. A glance at Fig. 5.3 shows that, at mid to low latitudes, such departures from $S_2(p)$'s global mean phase (158° or 0940 LST) are exceptional, indicating site-dependent systematic errors or a significant semidiurnal variation in τ_w^z at these sites. A second anomaly in Table 5.1 is the sharp decrease in $S_2(\tilde{\tau}^z)$ amplitude from KOKB to MKEA, i.e., from the northwest to the southeast extremes of the Hawaiian archipelago—a short span on the scale of the S_2 tide. No other pair of similarly proximate sites with statistically significant

Station Data				ZND		MET	
Site	lon	lat	ht	A_2	σ_2	A_2	σ_2
YELL	246	63	181	27±5	157±29	–	–
POTS	13	52	174	27±6	148±8	32±1	142±2
WTZR	13	49	666	60±9	134±16	36±1	143±1
ALGO	282	46	202	48±14	200±20	–	–
GOLD	243	35	987	149±12	148±3	–	–
JPLM	242	34	424	131±14	84±9	69±1	150±1
MDO1	256	31	2005	111±18	91±8	70±1	154±1
LHAS	91	30	3622	249±19	156±5	106±2	157±1
BAHR	51	26	-17	190±12	162±1	87±1	160±1
KOKB	200	22	1167	224±6	92±2	86±1	164±1
MKEA	205	20	3755	96±10	118±3	83±1	161±1
TOW2	147	-19	87	303±18	154±1	125±2	163±1
HRAO	28	-26	1414	107±16	135±7	–	–

Table 5.1: ZND and surface pressure (MET) determinations of S_2. Longitude in deg. E, latitude in deg. N, height in m, ZND amplitude in 10^{-2}mm, pressure amplitude in 10^{-2}mb, phase in deg. Error bounds are 1σ values.

determinations of $S_2(\tilde{\tau}^z)$ manifests such a disparity in amplitude. The disparity is unlikely to be caused by errors in the IGS orbits, the solid earth tide models, the transmitter clock biases, or the EOP models since these errors would be approximately common to both KOKB and MKEA. Furthermore, the MET data indicate that the hydrostatic component of the semidiurnal variation is nearly equivalent at the two sites, despite a large difference in height.

The $S_2(\tilde{\tau}^z)$ amplitude at KOKB is within 14% of the value predicted by the hydrostatic scale factor, but the $S_2(\tilde{\tau}^z)$ amplitude at MKEA is 50% lower than predicted. A close examination of MKEA's ZND frequency spectrum in the neighborhood of S_2 reveals that a considerable fraction of $S_2(\tilde{\tau}^z)$ energy is contained in sidebands resulting from a seasonal modulation. The same sidebands are a smaller fraction of $S_2(\tilde{\tau}^z)$ amplitude at KOKB and a much smaller fraction at LHAS, an inland site on the Tibetan Plateau whose height is nearly that of MKEA. One explanation might be that at MKEA's

height the marine-influenced atmosphere produces a seasonally-varying semidiurnal oscillation in τ_w^z.

Atmospheric pressure loading (APL), the slight (mm-scale) deformation of the flexible Earth caused by redistribution of atmospheric mass [68], is a possible error source for $S_2(\tilde{\tau}^z)$. Because APL is site-dependent it contributes to irregularities in $S_2(\tilde{\tau}^z)$; and because APL is caused by variations in surface pressure it is capable of masquerading as an atmospheric tide. None of the analysis centers that contribute to the IGS final orbits currently includes APL in its measurement model, nor is it included in the models used to generate the new IGS ZND product.

ZND is sensitive to APL through direct and indirect effects. The direct effect occurs simply because more atmosphere separates a depressed station from a GPS satellite at zenith. This effect is small: a 1-cm (worst-case) depression corresponds to a 0.003-mm increase in τ^z. The indirect effect arises because the site position errors caused by APL couple into satellite orbit and ZND estimates. This effect is larger and more difficult to evaluate because it depends on many factors, including: (1) the spatial extent and amplitude of the pressure anomaly, (2) the spatial distribution of the ground sites, (3) the APL response at each site, (4) the elevation cutoff angle, and (5) the estimation strategy used to determine ZND.

A study of the effects of APL on ZND was carried out by simulation. Realistic GPS satellite orbits and phase range measurements were generated for a globally-distributed set of ground stations. The effects of atmospheric loading were simulated by varying station heights in response to a global model of $S_2(p)$. APL sensitivity at each site was specified by regression coefficients from the International Earth Rotation Service Special Bureau for Loading (available at http://www.sbl.statkart.no). The coefficients were doubled to account for local departures from the inverted barometer assumption

used in their calculation. Simulation revealed that APL contamination of ZND estimates amounts to less than 11% of the amplitude of the hydrostatic oscillation in ZND. Simulation details and plots are found in the AM.

A final error source considered here is the ZND mapping function (MF). The IGS currently uses the Niell MF to convert neutral slant delays to zenith delays. Niell [69] showed that radiosonde-derived ("truth") MFs exhibit a diurnal variation at low elevation angles—a consequence of temperature-driven changes in the atmospheric scale height. This variation gives rise to a $\sim 0.1\%$ diurnal error at 5° in the hydrostatic Niell MF because the latter does not account for MF variations on time scales less than one year. If only 5° elevation slant delays were used to estimate ZND, a spurious 1.7-mm diurnal variation in estimated ZND would result. Accounting for the average distribution of elevation angles at each site and the 7° IGS elevation cutoff angle, the effect is reduced to 0.5 mm. A semidiurnal error in ZND caused by the same process can be estimated to be ≤ 0.17 mm (or $\leq 11\%$ of the global average $S_2^2(\tilde{\tau}^z)$ amplitude) by recognizing that the semidiurnal atmospheric temperature variation is at least factor of 3 smaller than the diurnal variation. Improved MFs based on numerical weather models (see [60]) can be expected to reduce these periodic errors in ZND estimates.

5.6 Conclusion

A strong global correlation with $S_2(p)$ suggests that the semidiurnal variation in IGS ZND data, $S_2(\tilde{\tau}^z)$, is due primarily to the actual semidiurnal variation in ZND, $S_2(\tau^z)$, and not to other geophysical signals or to orbit errors. Atmospheric loading and mapping function errors each contribute less than an estimated 11% of $S_2(\tilde{\tau}^z)$ amplitude. Local incongruities between $S_2(\tilde{\tau}^z)$ and $S_2(p)$ may indicate lingering site-dependent errors or

result from a semidiurnal variation in water vapor. These incongruities invite further study.

5.7 Acknowledgments

The authors are grateful to Jim Ray and Paul Tregoning for their careful comments.

Chapter 6

Conclusion

A scintillation model has been introduced that predicts the rate of cycle slipping in a GPS phase tracking loop, or, in another role, is used to synthesize time histories of realistic complex signal scintillation for evaluating GPS carrier tracking loops. Subsequent work will exploit this model to design scintillation-robust tracking loops. Two other applications of modeling and estimation have been presented. The first is a novel attitude and rate estimation strategy and the second is a study of the influence of atmospheric tides on GPS signal delay.

A unifying theme that connects the separate papers presented in this dissertation is the theory of model based estimation. In particular, issues of stochastic signals, random measurement errors, and general probability and statistics theory have been important in developing this work. These concepts have been applied in various ways to develop batch or sequential estimation algorithms or truth-model simulations for the physical systems under investigation.

BIBLIOGRAPHY

[1] T. E. Humphreys, M. L. Psiaki, B. M. Ledvina, , A. P. Cerruti, and P. M. Kintner, Jr., "Characterization of severe ionospheric scintillation and its effect on GPS carrier phase tracking," *IEEE Transactions on Aerospace and Electronic Systems*, 2007, submitted for review.

[2] J. A. Klobuchar, *Global Positioning System: Theory and Applications*. Washington, DC: American Institute of Aeronautics and Astronautics, 1996, ch. 12: Ionospheric Effects on GPS, pp. 485–515.

[3] T. E. Humphreys, M. L. Psiaki, B. M. Ledvina, and P. M. Kintner, Jr., "GPS carrier tracking loop performance in the presence of ionospheric scintillations," in *Proceedings of ION GNSS 2005*. Long Beach, CA: Institute of Navigation, Sept. 2005.

[4] K. M. Groves, S. Basu, J. M. Quinn, T. R. Pedersen, K. Falinski, A. Brown, R. Silva, and P. Ning, "A comparison of GPS performance in a scintillating environment at Ascension Island," in *Proceedings of ION GPS 2000*. Institute of Navigation, 2000.

[5] M. Knight and A. Finn, "The effects of ionospheric scintillation on GPS," in *Proceedings of ION GPS 1998*. Nashville, TN: Institute of Navigation, 1998.

[6] R. S. Conker, M. B. El-Arini, C. J. Hegarty, and T. Hsiao, "Modeling the effects of ionospheric scintillation on GPS/Satellite-Based Augmentation System availability," *Radio Science*, vol. 38, Jan. 2003.

[7] C. Hegarty, M. B. El-Arini, T. Kim, and S. Ericson, "Scintillation modeling for GPS-wide area augmentation system receivers," *Radio Science*, vol. 36, no. 5, pp. 1221–1231, Sept. 2001.

[8] G. Bishop, D. Howell, C. Coker, A. Mazzella, D. Jacobs, E. Fremouw, J. Secan, B. Rahn, C. Curtis, J. Quinn, K. Groves, S. Basu, and M. Smitham, "Test bed for evaluation of GPS receivers' performance in ionospheric scintillation–a progress report," in *Proceedings of ION GPS 1998*. Long Beach, CA: Institute of Navigation, 1998.

[9] K. C. Yeh and C. H. Liu, "Radio wave scintillations in the ionosphere," *Proceedings of the IEEE*, vol. 70, no. 4, pp. 324–360, 1982.

[10] J. Aarons, "Global morphology of ionospheric scintillations," *Proceedings of the IEEE*, vol. 70, no. 4, pp. 360–378, 1982.

[11] ——, "Global positioning system phase fluctuations at auroral latitudes," *Journal of Geophysical Research*, vol. 102, pp. 17,219–17,231, 1997.

[12] B. M. Ledvina, J. J. Makela, and P. M. Kintner, "First observations of intense GPS L1 amplitude scintillations at midlatitude," *Geophysical Research Letters*, vol. 29, no. 14, pp. 4–1—4–4, 2002.

[13] N. Luo and G. Lachapelle, "Relative positioning of multiple moving platforms using GPS," *IEEE Transactions on Aerospace and Electronic Systems*, vol. 39, no. 3, pp. 936–947, July 2003.

[14] P. Misra and P. Enge, *Global Positioning System, Signals, Measurements, and Performance*. Lincoln, Massachusetts: Ganga-Jumana Press, 2006.

[15] A. Cameron, "Next-generation air traffic controlled by GPS," GPS World, July 2006.

[16] M. A. Cervera and M. F. Knight, "Time series modelling of intensity and phase scintillation at GPS frequencies," *Acta Geodaetica et Geophsysica Hungarica*, vol. 33, no. 1, pp. 25–40, 1998.

[17] M. Nakagami, "The m-distribution: A general formula of intensity distribution of rapid fading," in *Statistical Methods in Radio Wave Propagation*, W. C. Hoffman, Ed. New York: Pergamon, 1960, pp. 3–36.

[18] E. J. Fremouw, R. C. Livingston, and D. A. Miller, "On the statistics of scintillating signals," *Journal of Atmospheric and Terrestrial Physics*, vol. 42, pp. 717–731, Aug. 1980.

[19] C. L. Rino, "A power law phase screen model for ionospheric scintillation (1. Weak scatter)," *Radio Science*, vol. 14, no. 6, pp. 1135–1145, 1979.

[20] T. E. Humphreys, B. M. Ledvina, M. L. Psiaki, and P. M. Kintner, "Analysis of ionospheric scintillations using wideband GPS L1 C/A signal data," in *Proc. ION GNSS 2004*. Long Beach, California: Institute of Navigation, 2004, pp. 399–407.

[21] T. N. Morrissey, K. W. Shallberg, A. J. Van Dierendonck, and M. J. Nicholson, "GPS receiver performance characterization under realistic ionospheric phase scintillation environments," *Radio Sci.*, vol. 39, pp. 1–18, 2004.

[22] E. J. Fremouw, R. L. Leadabrand, R. C. Livingston, M. D. Cousins, C. L. Rino, B. C. Fair, and R. A. Long, "Early results from the DNA Wideband Satellite experiment - Complex-signal scintillation," *Radio Science*, vol. 13, pp. 167–187, Feb. 1978.

[23] P. M. Kintner, B. M. Ledvina, E. R. de Paula, and I. J. Kantor, "Size, shape, orientation, speed, and duration of GPS equatorial anomaly scintillations," *Radio Science*, vol. 39, pp. 2012–+, April 2004.

[24] M. K. Simon and M. Alouini, *Digital Communications over Fading Channels*. New York: Wiley, 2000.

[25] C. L. Rino, "On the application of phase screen models to the interpretation of ionospheric scintillation data," *Radio Science*, vol. 17, no. 4, pp. 855–867, July 1982.

[26] V. E. Gherm, N. N. Zernov, and H. J. Strangeways, "Rate of phase change and fade depth on GPS paths due to ionospheric scintillation," in *Proc. of Twelfth International Conference on Antennas and Propagation (ICAP 2003)*, vol. 1. IEE, 2003, pp. 413–416.

[27] A. J. Viterbi, *Principles of Coherent Communication*. New York: McGraw-Hill, 1966.

[28] W. C. Lindsey and M. K. Simon, *Telecommunication Systems Engineering*. New Jersey: Prentice-Hall, 1973.

[29] F. M. Gardner, *Phaselock Techniques*, 3rd ed. Hoboken, NJ: Wiley, 2005.

[30] S. Gupta, "Phase-locked loops," *Proc. IEEE*, vol. 63, no. 2, pp. 291–306, 1975.

[31] G. Ascheid and H. Meyr, "Cycle slips in phase-locked loops: A tutorial survey," *IEEE Transactions on Communications*, vol. COM-30, no. 10, pp. 2228–2241, Oct. 1982.

[32] W. C. Lindsey and C. M. Chie, "A survey of digital phase-locked loops," *Proc. IEEE*, vol. 69, no. 4, pp. 410–431, 1981.

[33] R. A. Dana, "Effects of ionospheric scintillation on differential demodulation of GPS data," *IEEE Transactions on Aerospace and Electronic Systems*, vol. 33, no. 3, pp. 893–902, July 1997.

[34] S. A. Stephens and J. B. Thomas, "Controlled-root formulation for digital phase-locked loops," *IEEE Transactions on Aerospace and Electronic Systems*, vol. 31, no. 1, pp. 78–95, Jan. 1995.

[35] J. G. Proakis and M. Salehi, *Communication Systems Engineering*. Upper Saddle River, NJ: Prentice Hall, 1994.

[36] P. Ward, *Understanding GPS: Principles and Applications*. Boston: Artech House, 1996, ch. 5: Satellite Signal Acquisition and Tracking, pp. 119–208.

[37] A. J. Van Dierendonck, *Global Positioning System: Theory and Applications*. Washington, D.C.: American Institute of Aeronautics and Astronautics, 1996, ch. 8: GPS Receivers, pp. 329–407.

[38] P. A. Bello and B. D. Nelin, "The influence of fading spectrum on the binary error probabilities of incoherent and differentially coherent matched filter receivers," *IRE Transactions on Communication Systems*, vol. CS-10, pp. 160–168, June 1962.

[39] M. L. Psiaki and H. Jung, "Extended Kalman filter methods for tracking weak GPS signals," in *Proceedings of ION GPS 2002*. Portland, Oregon: Institute of Navigation, 2002, pp. 2539–2553.

[40] L. J. Mason, "Error probability evaluation for systems employing differential detection in a Rician fast fading environment and Gaussian noise," *IEEE Transactions on Communications*, vol. COM-35, no. 1, pp. 39–46, Jan. 1987.

[41] A. J. Van Dierendonck, "How GPS receivers measure (or should measure) ionospheric scintillation and TEC and how GPS receivers are affected by the ionosphere," in *Proc. 11th International Ionospheric Effects Symposium*, Alexandria, VA, 2005.

[42] M. J. Keskinen, "GPS scintillation channel model for the disturbed low-latitude ionosphere," *Radio Science*, vol. 41, pp. 4003–+, July 2006.

[43] C. L. Rino and J. Owen, "Numerical simulations of intensity scintillation using the power law phase screen model," *Radio Science*, vol. 19, pp. 891–908, June 1984.

[44] A. Pidwerbetsky, "Simulation and analysis of wave propagation through random media," Ph.D. dissertation, Cornell University, 1988.

[45] T. L. Beach, "Global positioning system studies of equatorial scintillations," Ph.D. dissertation, Cornell University, Ithaca, N.Y., 1998.

[46] R. Umeki, C. H. Liu, and K. C. Yeh, "Multifrequency spectra of ionospheric amplitude scintillations," *Journal of Geophysical Research*, vol. 82, pp. 2752–2760, July 1977.

[47] W. J. Myers, R. J. Gjeldum, C. H. Liu, and K. C. Yeh, "A study of ionospheric scintillations of phase and quadrature components," *Journal of Geophysical Research*, vol. 84, pp. 2039–2048, May 1979.

[48] S. P. Powell, E. M. Klatt, and P. M. Kintner, "Plasma wave interferometry using GPS positioning and timing on a formation of three sub-orbital payloads," in *Proceedings of the Institute Of Navigation Global Positioning System Conf.*, Portland, Oregon, Sept. 24–27, 2002, pp. 145–154.

[49] M. L. Psiaki, P. M. Kintner, Jr., and S. P. Powell, "Rapid energy dissipation in a yo-yo-type wire boom deployment system," *Journal of Guidance, Control, and Dynamics*, vol. 23, no. 3, pp. 483–490, 2000.

[50] M. L. Psiaki, S. P. Powell, E. M. Klatt, and P. M. Kintner, Jr., "Practical design and flight test of a yo-yo wire boom deployment system," in *Proceedings of the AIAA Guidance, Navigation, and Control Conf.*, Austin, Texas, Aug. 11–14, 2003.

[51] R. W. Longman and J. V. Fedor, "Dynamics of flexible spinning satellites with radial wire antennas," *Acta Astronautica*, vol. 3, no. 1 and 2, pp. 17–37, 1976.

[52] M. L. Psiaki, E. M. Klatt, P. M. Kintner, Jr., and S. P. Powell, "Attitude estimation for a flexible spacecraft in an unstable spin," *Journal of Guidance, Control, and Dynamics*, vol. 25, no. 1, pp. 88–95, 2002.

[53] T. E. Humphreys, "Attitude determination for small satellites with modest pointing constraints," Master's thesis, Utah State University, Logan, Utah, 2003.

[54] M. L. Psiaki, F. Martel, and P. K. Pal, "Three-axis attitude determination via Kalman filtering of magnetometer data," *Journal of Guidance Control and Dynamics*, vol. 13, no. 3, pp. 506–514, 1990.

[55] M. Challa, G. Natanson, and N. Ottenstein, "Magnetometer-only attitude and rates for spinning spacecraft," in *Proceedings of the AIAA/AAS Astrodynamics Specialists Conf.*, American Institute of Aeronautics and Astronautics, Reston, VA, 2000, pp. 311–321.

[56] M. L. Psiaki, "Global magnetometer-based spacecraft attitude and rate estimation," *Journal of Guidance, Control, and Dynamics*, vol. 27, no. 2, pp. 240–250, 2004.

[57] M. L. Psiaki and Y. Oshman, "Spacecraft attitude rate estimation from geomagnetic field measurements," *Journal of Guidance, Control, and Dynamics*, vol. 26, no. 2, pp. 244–252, 2003.

[58] G. M. Lerner, "Three-axis attitude determination," in *Spacecraft Attitude Determination and Control*, J. R. Wertz, Ed. Boston: D. Reidel, 1978, pp. 424–426.

[59] G. J. Bierman, in *Factorization Methods for Discrete Sequential Estimation*. New York: Academic Press, 1977, pp. 69–76, 115–122, 214–217.

[60] S. H. Byun, Y. Bar-Sever, and G. Gendt, "The new tropospheric product of the international GNSS service," in *Proceedings of ION GNSS 2005*. Long Beach, CA: Institute of Navigation, 2005.

[61] A. Dai, J. Wang, R. H. Ware, and T. Van Hove, "Diurnal variation in water vapor over North America and its implications for sampling errors in radiosonde humidity," *Journal of Geophysical Research*, vol. 107, no. D10, 2002.

[62] T. Humphreys, M. Kelley, and P. Kintner, "GPS-based measurement of atmospheric tides," in *Proc. ION GNSS 2004*. Long Beach, California: Institute of Navigation, 2004, pp. 864–880.

[63] S. Chapman and R. S. Lindzen, *Atmospheric Tides*. New York: Gordon and Breach, 1970.

[64] A. Dai and J. Wang, "Diurnal and semidiurnal tides in global surface pressure fields," *J. Atmos. Sci.*, vol. 56, pp. 3874–3891, 1999.

[65] R. D. Ray, "Comparisons of global analyses and station observations of the S_2 barometric tide," *Journal of Atmospheric and Solar-Terrestrial Physics*, vol. 63, pp. 1085–1097, 2001.

[66] J. L. Davis, T. A. Herring, I. I. Shapiro, A. E. E. Rogers, and G. Elgered, "Geodesy by radio interferometry: Effects of atmospheric modeling errors on estimates of baseline length," *Radio Sci.*, vol. 20, no. 6, pp. 1593–1607, 1985.

[67] B. Haurwitz and A. D. Cowley, "The diurnal and semidiurnal barometric oscillations, global distribution and annual variation," *Pure Appl. Geophys.*, vol. 102, pp. 193–222, 1973.

[68] L. Petrov and J. Boy, "Study of the atmospheric pressure loading signal in very long baseline interferometry observations," *Journal of Geophysical Research*, vol. 109, p. B03405, 2004.

[69] A. E. Niell, "Global mapping functions for the atmosphere delay at radio wavelengths," *Journal of Geophysical Research*, vol. 101, pp. 3227–3246, 1996.